GRAPH ANALYTICS FOR SMART MANUFACTURING

A Dissertation

by

ASHIF SIKANDAR IQUEBAL

Submitted to the Office of Graduate and Professional Studies of
Texas A&M University
in partial fulfillment of the requirements for the degree of

DOCTOR OF PHILOSOPHY

Chair of Committee,	Satish T.S. Bukkapatnam
Committee Members,	Daren Cline
	Yu Ding
	Dinakar Sagapuram
	Arun Srinivasa
Head of Department,	Lewis Ntaimo

August 2020

Major Subject: Industrial Engineering

ABSTRACT

Emergence in the high-resolution sensing and imaging technologies have allowed us to track the variability in manufacturing processes occurring at every conceivable resolution of interest. However, representation of the underlying manufacturing processes using streaming sensor data remains a challenge. Efficient representations are critical for enabling real-time monitoring and quality assurance in smart manufacturing. Towards this, we present graph-based methods for efficient representation and quantification of the image data gathered from advanced manufacturing processes.

In this dissertation, we first focus on experimental studies involving the finishing of complex additively manufactured components and discuss the important phenomenological details of the polishing process. Our experimental studies point to a material redistribution theory of polishing where material flows in the form of thin fluid like layers, eventually bridging up the neighboring asperities. Subsequently, we use the physics of the process gathered from this study to develop a random planar graph approach to represent the evolution of the surface morphology as gathered from electron microscopic images during mechanical polishing. In the sequel, we focus on unsupervised image segmentation using graph cuts by iteratively estimating the image labels by solving the max-flow problem while optimally estimating the tuning parameters using maximum a posteriori estimation. We also establish the consistency of the posterior estimates. Applications of the method in benchmark and manufacturing case studies show more than 90% improvement in the segmentation performance as compared to state-of-the-art unsupervised methods. While the characterization of the advanced manufacturing processes using image and sensor data is increasingly sought after, it is equally important to perform characterization rapidly. Towards this, we employ machine learning methods for the rapid characterization of the salient microstructural phases present on a metallic workpiece surface via a nanoindentation-based lithography process. In closing, a summary of the contributions and directions of future work are also presented.

DEDICATION

To my parents

Md. M. A. Ansary and Razia Umrani

ACKNOWLEDGMENTS

As another chapter of my life concludes, I have come to appreciate the importance of failures—they are what defines who we are, and success is merely an outcome. My Ph.D. journey was no short of a roller coaster ride, and of course, I hate riding one. But I have always been blessed to have people around me that helped me navigate the ebb and flow, and I wouldn't have wanted this journey to be any different.

Meeting research expectations while juggling through courses and multiple projects was not an easy endeavor. But these experiences were instrumental in instilling the importance of perseverance and hard work in me from the beginning, for which I am grateful to my advisor, Dr. Satish Bukkapatnam. I am thankful for his support, endless motivation, and hours of discussion, whether it was day or night, weekday or weekend. This dissertation would not have been possible without his guidance and constant encouragement, and I remain deeply indebted to him.

I want to extend my gratitude to Dr. Arun Srinivasa, who guided me on my research problems and taught me personal skills that always came in handy. His endless discussion and mentoring sessions were also a boost to my motivation. I want to sincerely acknowledge the kind and sincere support of Dr. Daren Cline. Being a professor of Statistics, my research problems in manufacturing were out of his court. His willingness to understand those problems from a manufacturing context and provide insightful comments from a statistical perspective greatly helped me complete this dissertation while simultaneously pursuing a master's degree in Statistics.

I would also like to acknowledge Dr. Dinakar Sagapuram and Dr. Yu Ding, whose advice and insightful comments invaluably helped me with my writing and presentation skills. Apart from my committee members, I want to acknowledge Dr. Natarajan Gautam, who selflessly spent hours on counseling and resolving my problems. Whether it was an academic hurdle or an emotional breakdown, Dr. Gautam was always there to offer suggestions and guidance. I also want to thank Dr. Alaa Elwany, Dr. Shahin Shahrampour, and Dr. Amarnath Banerjee for their advice and feedback throughout my Ph.D.

The road to my Ph.D. program began with Dr. Manoj Tiwari—my undergraduate mentor and advisor (now the director of the National Institute of Industrial Engineering, India). He taught me everything from reading journals to writing papers and prepared me for grad school, and I will always be indebted to him for leading me on this path. I am obligated to share my deepest gratitude to the many people I met during my Ph.D. journey. I want to sincerely acknowledge Dr. Trung Le, Dr. Hoang Tran, Dr. Zimo Wang, Bhaskar Botcha, Iskandar El-Amri, and Shirish Pandagare. I want to thank many masters and undergraduate students who painstakingly conducted hours of tiring experiments reported in this dissertation. The list of people whom I owe my gratitude would be incomplete without Kahkashan Afrin. While she was also steering the same boat, she never backed down from providing all the emotional support and motivation and was always there to cheer me up.

Finally, I would like to share my deepest gratitude to my parents, who always sacrificed their comfort for my success and building my career. I thank them for their unconditional love and support during my Ph.D.

CONTRIBUTORS AND FUNDING SOURCES

Contributors

This work was supported by a dissertation committee consisting of Professor Satish Bukkapatnam and Professor(s) Yu Ding and Dinakar Sagapuram of the Department of Industrial and Systems Engineering and Professor Daren Cline of the Department of Statistics and Professor Arun Srinivasa of the Department of Mechanical Engineering.

The additively manufactured Ti-6Al-4V samples employed in this study were provided by Professor Guha Manogharan of the Pennsylvania State University. The polishing machine–Buehler Metaserv Grinder-Polisher (model 95-C2348-160) was provided by Professor Alex Fang of Texas A&M University. A part of the experimentation and data collection was performed by Iskander El-Amri of Texas A&M University.

All other work conducted for the dissertation was completed by the student independently.

Funding Sources

Graduate study was supported by the National Science Foundation's Grants – CMMI 1432914, CMMI 1538501, ECCS 1547075, IIS 1849085, and Texas A&M University's X-Grants program.

TABLE OF CONTENTS

LIST OF FIGURES

FIGURE Page

LIST OF TABLES

1. INTRODUCTION

1.1 Analytics for smart manufacturing

The advent of the Internet of Things (IoT) is propelling the generation of a deluge of data (more than 1.8 petabytes per year) across and about various aspects of manufacturing processes. These advances have opened an unprecedented opportunity to harness information from these vast data streams to *characterize* as-you-make synergistically. It holds a huge potential for the emerging paradigm of materials-on-demand manufacturing, where "intelligent machines" operate autonomously to discover the optimal process conditions and characterize the morphology and microstructures [75]. At the systems level, the data streams also allow enhanced connectivity and coordination among all components across the value chain—right from the material, machines, and shop floor to the supply chain and the enterprise—and thus bring substantial improvements in the productivity of the whole system.

Smart manufacturing aims at harnessing the streaming data generated from advanced manufacturing processes to enable efficient decision making under uncertain environments, autonomous experimentation for materials-on-demand manufacturing, and closed-loop monitoring and control of complex manufacturing processes such as additive and hybrid manufacturing (AM/HM) technologies. In this work, we primarily focus on additive manufacturing owing to its potential to fabricate complex, free-form geometries with a near-net shape, and radically new and innovative part designs while minimizing the production time and costs. More pertinently, the AM market has grown five folds during 2014-2018 and is expected to become a $25 billion industry by 2025 with expanding industrial applications. However, despite strong growth projections, AM technologies only represent 0.04% of the total global manufacturing market, with prototyping occupying the majority share. This is primarily due to the poor surface finish and frequent occurrence of defects particularly pores emerging from various sources that significantly deteriorate the mechanical performance and the overall functional integrity of AM components.

Along the similar lines, significant research has been carried out towards optimizing the process parameters to improve the surface morphology and reduce the defect concentration while maintaining the desired level of mechanical performance as well as geometric dimensionality and tolerances. However, optimization of process parameters turns out to be an extremely challenging problem especially due to the combinatorial nature of the search space, variations, and confounding effects among the process state variables. As an offshoot of global thrusts in material genomics, new alloy systems are increasingly being considered for industrial practice, especially to fabricate structural components of critical importance via AM technologies [84]. Due to the fast-paced introduction of material systems for AM as well as the inherent process complexities, any effort to optimize the process to mitigate defects for a particular scenario would likely be ineffective for subsequent AM operations.

Towards this, advancements in *in situ* imaging and sensing technologies have enabled monitoring of manufacturing processes over sub-micrometer resolutions at high speeds, fidelity, and field-of-view [56]. These open exciting opportunities for real-time tracking of spatiotemporal evolutions, especially of surface morphologies that take place over nano- through micro- and mesoscale, that are critical for quality assurance as well as physical characterization of manufacturing processes. In this context, representation approaches, which are essential in harnessing information from these emerging imaging and multi-modal sensing technologies for quality assurance, and process characterization remain at a nascent stage. The need for such representation schemes is becoming essential in AM and other advanced manufacturing technologies.

While advances have been made towards identification and tracking of image-based morphological features, quantification of their spatiotemporal evolution, and connecting these with the underlying process physics remain open issues. Quantification of spatiotemporal variation from *in situ* images poses significant challenges mainly, because (a) images capture only small snapshots in time and space, (b) significant uncertainties exist in the trajectories of the location and shape of morphological features (in addition to their compositions and structures) as captured from the images, and (c) complex, seemingly irregular, evolution patterns do not lend themselves to conventional statistical descriptions. These evolution patterns are also influenced by the phase and chemical transformation phenomena during finishing, which are inherently stochastic.

1.2 Organization and contributions of this dissertation

This dissertation aims at innovations in advanced manufacturing processes as well as methodological foundations in data analytics to enable rapid, *in situ* characterization of smart manufacturing processes. More specifically, the dissertation focuses on developing advanced manufacturing processes for finishing of additively manufactured components and experimental strategies to study the phenomenologies underlying surface modification during these finishing processes. These key phenomenological observations not only provide the exact physics of the surface smoothening process but also forms the basis for developing physics-based models for the representation and quantification of the surface morphology, necessary for autonomous detection of polishing endpoints, i.e., deciding when to stop polishing. Along the direction of representing surface morphology, we are also concerned with the unsupervised learning methods when labeled data is costly to obtain, e.g., high-resolution microscopic images of the surface morphology during additive manufacturing. Towards this, we delve into developing statistical models for unsupervised learning methods.

In the following, we outline the key contributions that emerged from this dissertation towards addressing the challenges pertaining to the representation of the streaming sensor and image data gathered from advanced manufacturing processes.

The second chapter of this dissertation is devoted to studying the challenges pertaining to poor surface morphology and integrity of additively manufactured components [140, 74, 59, 77]. A detailed description of the sample preparation and review of the existing post-processing methods are presented. We then present a multi-stage surface finishing process and compare the surface morphology characteristics such as average surface roughness (S_a), surface peak to valley (S_{pv}), hardness, and the resulting microstructures as obtained from that of multi-stage surface finishing process and traditional milling process. *The underlying research hypothesis in this study is to test if a multi-stage finishing process results in superior surface integrity as compared to traditional subtractive methods.*

Following up on the second chapter, we note that surface finish requirements vary depending upon the applications, from biomedical implants that call for differential surface roughness (sub-micron finish at bearing locations while rough and textured surface at the bone-implant interaction site [140]) to mechanical applications that require a uniform specular finish (average surface roughness, $S_a < 25$ nm). Therefore, it is important to understand the exact phenomenology governing surface modification during the post-processing stages and develop accurate modeling approaches to achieve the desired specifications.

The surface morphologies obtained during various stages of the polishing process are observed under a scanning electron microscope to understand the exact phenomenology of the finishing process. *The hypothesis in this research (Chapter 3) is to test if surface smoothening occurs due to material removal, which is the traditional theory.* To further validate the hypothesis, we use analytical models to determine the asperity-abrasive contact temperatures, microstructural evolution at the surface, as well as potential microscopic mechanisms during asperity-abrasive contacts in polishing [78].

The next chapter (Chapter 4) is based on harnessing the physics of the polishing process to develop a robust approach for representation and quantification of the surface morphology evolution during finishing. We first review the existing methods towards modeling the surface morphology using image data. From the previous study (Chapter 3), we note that the evolution in the surface morphology during the polishing process is reminiscent of an evolving planar graph where the undulations on the surface, also known as asperities (or nodes in the graph) bridge with neighboring nodes to form a flat, smooth surface. In light of this, we develop a random planar graph representation of the surface morphology during the finishing process and quantify the resulting graphs using the second smallest eigenvalue

(λ_2) of the graph Laplacian [39, 3].

We subsequently use these quantifiers for endpoint detection, i.e., determining when to stop the polishing process. Finally, we establish the sensitivity of the Fiedler value to capture the evolution in the surface morphology as well as the effect of node density lying near the boundary of the image.

Along the similar lines of representation of the surface morphology, as described in Chapter 4, characterization of surface porosity and defects is critical to facilitate wider adoption of additive manufacturing. The problem of identifying the defects using *in situ* images is particularly challenging because labeled data is difficult to obtain. This excludes the possibility of employing supervised segmentation methods. Therefore, the fourth objective (Chapter 5) in this dissertation focuses on developing an unsupervised algorithm based on a max-flow formulation for the segmentation of defects [76, 2]. Towards accomplishing this objective, we present an approach to consistently estimating the flow capacities of a continuous max-flow/min-cut problem leading to fully unsupervised, fast image segmentation. We also present the performance of the proposed approach in benchmark datasets.

While the previous chapters focused on harnessing image data for characterization of manufacturing processes, Chapter 6 of this dissertation will focus on developing strategies for the rapid characterization of manufacturing processes using streaming time series data [75, 4]. More specifically, we develop a sensor-based platform for rapid characterization of materials microstructure in a hybrid manufacturing platform. We employ a machine learning approach to connect the time-frequency patterns of the corresponding acoustic emission (AE) signals with the underlying microstructural phases and demonstrate the efficacy of underlying AE signals to identify novel patterns and possible microstructural anomalies. The final chapter of this dissertation will summarize the research undertaken in this dissertation, the contributions, and the impact on advanced manufacturing. A brief discussion on future research directions is also presented.

2. FINISHING SURFACE MORPHOLOGY OF ADDITIVE MANUFACTURED COMPONENTS *

Post-processing strategies are becoming imperative for a range of additively manufactured alloys, especially those with applications in aerospace and biomedical industry, to achieve the desired surface quality and integrity. This chapter focuses on the impact of post-processing recipes on the surface morphology and mechanical properties of AM components. More specifically, we compare the effect of traditional machining and a multi-step fine-abrasive finishing process on the surface morphology and integrity of Ti-6Al-4V workpieces manufactured via an Electron Beam Melting (EBM) process. Extensive experimental investigations demonstrate that the multi-step finishing process results in an ultra-smooth surface finish of $S_a < 50$ nm, increases the surface density (and hence the bearing characteristics) by minimizing the surface void volumes to less than 0.2% and achieves a 20% improvement in surface hardness.

2.1 Introduction

Additive Manufacturing is defined as "the process of joining materials to make objects from 3D model data, layer upon layer, as opposed to selectively removing materials in subtractive manufacturing methodologies" [1]. AM is increasingly becoming attractive to the industry as well as the research community for its ability to manufacture complex components, achieve the near-net shape, and customize geometric designs without the need for custom fixtures and jigs [115]. In 2018, the AM industry experienced a 41.9% growth rate, consistent with the growth over the past five years, with expected net revenue of $15.8 billion in 2020. However, among several disadvantages of AM (specifically metal AM), poor surface finish and porosity significantly hinder its broader adoption. For example, load-bearing ap-

---

[*] Reprinted with permission form A. S. Iquebal, S. El Amri, S. Shrestha, Z. Wang, G. P. Manogharan, and S. Bukkapatnam, "Longitudinal milling and fine abrasive finishing operations to improve surface integrity of metal AM components," Procedia Manufacturing, vol. 10, pp. 990–996, Copyright 2017 Elsevier

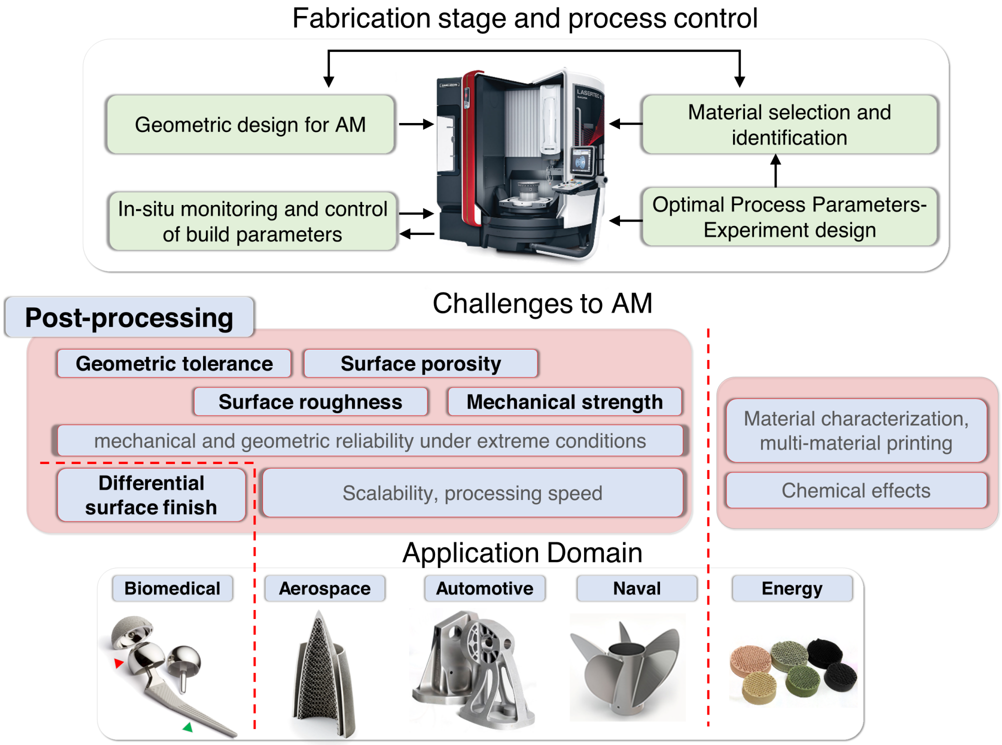

Figure 2.1: Overview of the key challenges pertaining to the surface morphology and integrity of AM components that need to be addressed before the application phase. Challenges highlighted in bold are the focus of the current study and are analyzed via a longitudinal post-processing strategy.

plications in the mechanical and aerospace industry require a specular surface finish with tighter part feature tolerances [36]. Successful adoption of metal AM components in such applications need appropriate post-processing treatments. Traditional subtractive methods such as machining offer advantages that would mitigate these challenges. However, they suffer from poor material utilization, machinability issues, limited part complexity, and custom tooling requirements. Therefore, integrating subtractive methods such as machining and grinding with rather advanced polishing processes through a hybrid approach is desirable. Figure 2.1 summarizes some of the key challenges that may be addressed by adopting appropriate post-processing technologies.

This chapter summarizes the influence of post-processing methods on the resulting surface morphology, microhardness, and mechanical load-bearing characteristics. Specifically, Ti-

6Al-4V components fabricated through EBM are subjected to two post-processing methods: (1) traditional dry milling and (2) multi-stage fine-abrasive finishing. Section 2.2 presents a brief background and literature review on the post-processing of EBM fabricated parts, followed by experimental studies in Section 2.3. Section 2.4 summarizes the finding from the experiments.

2.2 Background

Much of the work in hybrid processes with AM has focused on directed energy metal deposition processes such as wire welding using a metal inert gas, metal active gas [9], and laser melting due to the relative ease of integration [11]. These hybrid systems are formulated by retrofitting 3-axis platforms (e.g., ball screw/ lead screw, etc.) in a CNC machining centered by adding the deposition head within the machining volume. Another study presented a powder plasma-based system that utilizes 3-axis contour milling to finish machined near-net shape parts [156]. In such processes, hybrid manufacturing is achieved by alternating between additive and subtractive methods after every few layers. Machining is performed after deposition or formation of relatively thick layers followed by sequential addition and subtraction until the final part is created. Other hybrid processes employ additional rotary axes based laser-aided deposition process in which the deposition table is rotated to accommodate overhanging surfaces by depositing material from multiple directions followed by machining [95].

Post-processing is considered as a crucial and challenging step for AM practice, and it is emerging as one of the critical elements of hybrid manufacturing systems [98]. While metal AM (e.g. EBM) is a desirable option for fabricating custom components in the biomedical and aerospace industry, tighter tolerance and performance specifications of these components necessitate finishing as an essential post-processing step. For example, in the context of biomedical implants, authors in [130] suggest that a roughness R_a of $0.5 - 8.5$ μm was most conducive for osseointegration. However, ultra-smooth finish $R_a < 0.1$ μm is necessary on the bearing surfaces (e.g. at hip and knee joints) to ensure performance as well as durability

Table 2.1: Summary of the post processing methods applied to additive manufactured parts.

No.	Post processing Method	Description	Remarks
1.	Sintering	Solid-state densification mechanism at high temperature (∼1300°C) in phase, but well below its melting point. It involves surface, grain boundary as well as lattice diffusion [157]	Although surface voids were reduced, no significant improvement in Young's Modulus and Microhardness has been reported [104]
2.	Hot Isostatic Pressing (HIP)	Sintering under pressure, achievable at a relatively lower temperature (∼900°C) and high isostatic pressure [157]	
3.	Using additives	(a) Additives such as TiH_2 can be added as a starting powder [60] or (b) in-situ addition of elements such as Boron [154]	The purity of Ti64 is lost and might not be acceptable in many applications
4.	Sandblasting (SB)	Stream of sand is shot against the workpiece surface to minimize the irregularities or remove undesirable particles [41]	Frequently adopted, might help in controlling the initial surface properties
5.	Shot Peening (SP)	Theoretically, a relatively efficient methodology for producing a compressive residual stress layer and enhance the mechanical properties [153]	Contrary to the theory, SP deteriorates the fatigue strength due to initiation of crack from internal pores
6.	Shot pulsed laser*	Create a rough surface texture via short-pulse laser radiations [61]	Applied on selective laser melting parts
7.	Surface Coating & Alloying*	A thin layer of composite is deposited on the surface, thereby improving the tribological properties [21]	
8.	Machining	Traditional machining methods, e.g., end mill to mitigate surface irregularities.	Heat generation remains an important issue

under dynamic loading [80]. In this context, it is important that post-processing technologies are economical to realize the desired surface characteristics, so that the overall production cost can be minimized while meeting the part requirements. Currently, only a handful of efforts have been reported in the literature on the finishing of EBM printed components and a brief summary of some of these methods is presented in Table 2.2. Note that some of the methods mentioned here have only been applied to AM processes other than EBM (marked asterisk).

2.3 Materials and methods

2.3.1 Surface preparation

Ti-6Al-4V samples of ⌀50 mm and 7 mm thickness with controlled surface morphology consisting of spherical asperity structure were prepared using an Arcam EBM machine operating at a vacuum of 2 Pa and accelerating voltage of 60 kV. The process involved raking a 50 μm layer of Ti-6Al-4V powder of average ⌀72 μm (see Figure 2.2(c) for the distribution of diameter of Ti-6Al-4V particles) using a focused electron beam of 3 mA, scanning at a speed of 10 m/s. The resulting surface consists of granular Ti-6Al-4V particles with a unique spherical asperity structure. SEM image of the representative surface morphology is shown in Figure 2.2(a). The distributions of asperity height and diameter are shown in Figures 2.2(b) and (c), respectively. The asperity height as well as the diameter exhibit a Weibull distribution with an average value of 72 μm and 64.5 μm, respectively, and a standard deviation of ~ 15 μm. Incidentally, the idealization of surfaces as a collection of spherical asperities (with Gaussian and Weibull distribution of heights) has been the basis for many prior theoretical analyses of elastic-plastic contacts between rough surfaces [73].

2.3.2 Experimental approach

The Ti-6Al-4V samples were polished on a Buehler Metaserv Grinder-Polisher (model 95-C2348-160) using silicon carbide (SiC) polishing pads (⌀203 mm), in stages, with progressively smaller abrasives ranging from 30 μm to 5 μm under dry conditions. A steady nominal down pressure of 0.5 kPa was maintained and the polisher speed was fixed at 500 rpm. The surface was manually subjected to a quasi-random orbital motion. The final polishing step involved the use of alumina abrasives (< 1 μm), suspended in an aqueous solution (20% by wt., pH ≈ 7.5) for 20 minutes to impart a specular finish to the surface. The slurry was routinely flushed to avoid possible agglomeration of finer abrasives into large clusters that may result in scratching.

2.3.3 Surface and microstructure characterization

The polishing was interrupted at every 90 s intervals to observe the surface morphology changes and the evolution of asperity structure using a Zeiss EVO scanning electron microscope. Quantitative details pertaining to the surface finish including surface roughness (S_a) and volume of inter-asperity "valleys" (S_v) were measured using a white light interferometer from Zegage. Inter-asperity valleys were characterized by the surface heights lying below the 10^{th} percentile on the bearing area curve (i.e., the cumulative distribution of surface profile) [73]. To ensure that observations and measurements were made at the same surface location during different polishing steps, the sample surface was initially indented with a 2×2 mm square grid. The vertices of this grid enabled us to image the same surface location after each interrupted test. To facilitate better observations of the plastic flow patterns at asperity surfaces, the sample was tilted by 70° in the scanning electron microscope.

The outcome of machining and fine abrasive finishing of as-fabricated EBM sample prior to surface characterization and microhardness testing is presented in Figure 2.3. Evidently, the fine abrasive finishing process has resulted in a significant improvement in the surface morphology. The average roughness of the workpiece improved from $S_a \approx 25$ μm before finishing to $S_a \approx 0.045$ μm after finishing. Simultaneously, the peak-to-valley height reduced from $S_{pv} \approx 250$ μm before finishing to $S_{pv} \approx 5$ μm after finishing.

Representative surface profiles are shown in Figures 2.3(a), (b), and (c). Note that the granular structure on as-fabricated sample shown in Figure 2.3(a) exhibit voids in the work piece resulting in a much lower surface density. On the other hand, polished work piece is mostly free from any granular structure and the inter-granular voids although it shows signs of scratch marks and pits on the surface as shown in Figure 2.3(c). The scratch marks may be attributed to the limitations of hand-held mechanical polishing as well as agglomeration of abrasives forming larger abrasive particles when an aqueous solution is employed.

The hardness of the polished sample was measured on a Leco LM300 AT microhardness machine with a load and dwell time of 500 g and 5 s, respectively. To observe the microstructures, the mechanically polished samples were first treated with Kroll's reagent ($5-7\%$ nitric acid (HNO_3) and $2-4\%$ hydrofluoric acid (HF) and rest distilled water) for 10 s and then rinsed with distilled water. The microstructures were observed using SEM under high vacuum ($\leq 1 \times 10^{-4}$ mbar) with accelerating voltage of 15 kV and a working distance of 15 mm. Figure 2.2(d) shows the representative microstructure observed in an as-EBM fabricated Ti-6Al-4V, comprising of lamellar α and β phases with both colony and basket-weave (also called Widmanstätten pattern) morphology. The α lamellar phase is etched out by Kroll's reagent and therefore, exhibits a darker contrast as compared to the β phase under SEM. Here, the β phase resembles rod-like morphology with an average thickness of 200 nm. Details of the effect of polishing on the hardness and surface microstructure is presented in Chapter 3 in detail.

2.4 Summary and conclusions

This chapter presented the effects of post-processing of metal AM parts (Ti-6Al-4V) through machining and fine-abrasive finishing. Results suggest that machining improved the average surface roughness 98.1% and increased surface hardness by 37%. In contrast, the average surface roughness improved by 99.82% and the microhardness increased by 11% when the workpiece was subjected to fine-abrasive finishing (with significantly more efficacy on z-build-direction surfaces). We also noted that fine-abrasive finishing reduced the fraction of voids by almost 99.81%, thus providing an effective means to enhance the bearing capacity of AM components. The study showed the importance of post-processing, specifically the first reported study on the influence of multi-step fine abrasive finishing on additively manufactured surfaces. Implications of the findings include applications in efficiently combining traditional post-processing, machining, and non-traditional approaches such as fine abrasive finishing, electrochemical polishing, and magnetic polishing of AM parts.

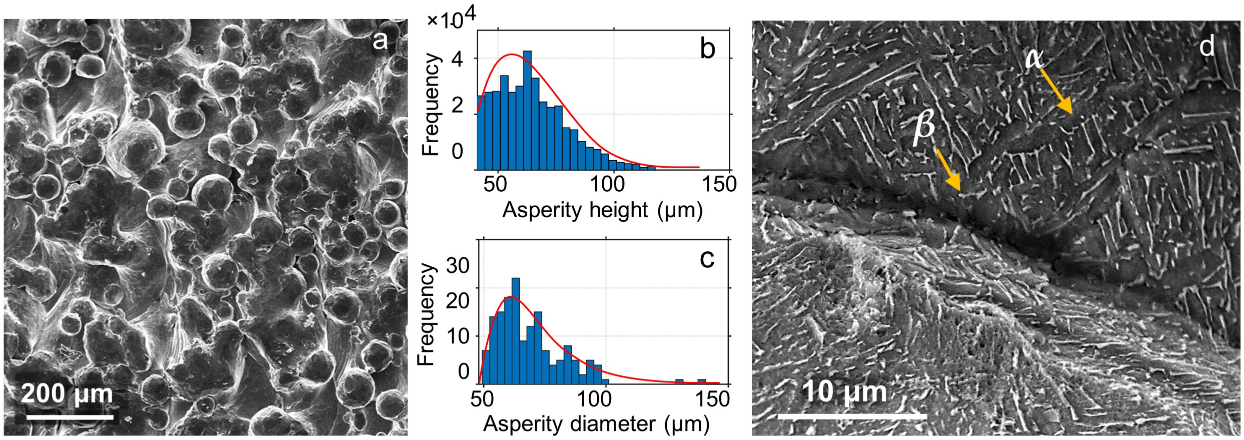

Figure 2.2: (a) SEM image showing the spherical asperity structure of the sample surface; (b) and (c) are respectively the distribution plots for the asperity height and diameter as measured using white light interferometry. Empirical estimate suggests a Weibull distribution with an average value of 72 μm and 64.5 μm, respectively and a standard deviation of $\sim$ 15 μm. (d) SEM image showing the representative $\alpha + \beta$ colony with α lamellae (in dark) interspersed with β phase (rod-shaped, in white) of average thickness 200 nm.

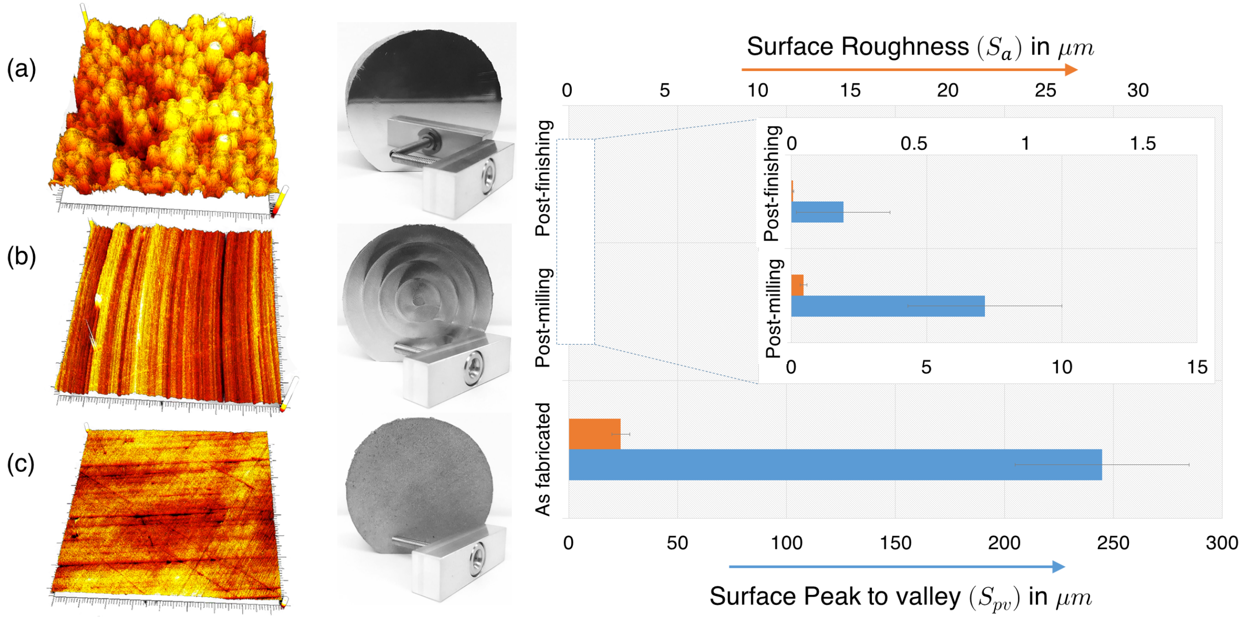

Figure 2.3: Summary of the as fabricated EBM, machining & abrasive finishing results comparing surface morphology. (a) as fabricated EBM, (b) machining & (c) abrasive finishing results comparing surface morphology.

3. SURFACE PLASTIC FLOW IN POLISHING OF ROUGH SURFACES*

In this chapter, we are concerned with understanding the exact phenomenology of surface smoothening during mechanical polishing. Experimental studies presented in this chapter point to material redistribution as the dominant mechanism of polishing, as opposed to material removal. Electron microscopy observations of Ti-6Al-4V surface with a spherical asperity structure—realized via AM—during successive polishing stages suggest that asperity-abrasive contacts exhibit viscous behavior, where the asperity material flows in the form of thin ($1-10$ μm) fluid-like layers. Subsequent bridging of these layers among neighboring asperities results in progressive surface smoothening. Using analytical asperity-abrasive contact temperature modeling and microstructural characterization, we show that the sliding contacts encounter flash temperatures of the order of 700-900 K which is in the range of the dynamic recrystallization temperature of the material considered, thus supporting the experimental observations. The research findings and observations are of broad relevance to the understanding of plastic flow behavior of sliding contacts ubiquitous in materials processing, tribology, and natural geological processes as well as present unique opportunities to tailor the microstructures by controlling the thermomechanics of the asperity-abrasive contacts.

3.1 Introduction

The practice of polishing to impart solid surfaces with smooth, lustrous finish has been known for centuries. The use of hard abrasives such as corundum and diamond for polishing in fact dates back to the Neolithic period [96] and Leonardo da Vinci is credited with the earliest systematic design of a polishing machine [114]. It might be surprising then to know that the mechanism of polishing—how surface irregularities are smoothened out by abrasive particles—is still unsettled. Excellent account of the history and theories of polishing can be

---

*Reprinted with permission from A. S. Iquebal, D. Sagapuram, and S. T. S. Bukkapatnam, "Surface plastic flow in polishing of rough surfaces," Scientific reports, vol. 9, no. 1, p. 10617, Copyright 2019 Springer Nature found in [15]. However, it may suffice to note that mainly two lines of thought for the polishing mechanism have prevailed: that of abrasion and surface flow. Early theories by Hooke and Newton [108], followed by those of Herschel [15] and Rayleigh [40] viewed polishing essentially as an abrasion or a grinding process at a very fine scale where surface irregularities are removed by cutting action of the abrasives. The work by Samuels [127] presented irrefutable evidence for this mechanism and showed how abrasives act as planing tools and result in the generation of well-defined chips as they slide past a surface. However, the fine scale abrasion theory falls short in explaining the high (almost an order of magnitude) compressive residual stresses obtained after polishing as compared to milling and finish machining operations [151].

The alternative theory emerges from the work by Beilby [24] who proposed surface smoothening occurring via surface flow and material redistribution. Here, it is believed that the material from surface peaks 'flows' to fill up the valleys and forms a thin vitreous surface layer, generally referred to as the "Beilby layer". Bowden and Hughes [30] further developed this theory and proposed that surface flow is in fact mediated by local melting at the surface–abrasive contacts. Electron diffraction measurements of polished surfaces have been presented as indirect evidence for the Beilby layer formation, but these observations were later proved to be inconclusive. To our knowledge, no conclusive evidence for the surface flow or melting has been provided to date. Other theories of polishing also exist, among which noteworthy is the molecular level material removal mechanism put forward by Rabinowicz [119] based on energy considerations.

More recently, the emergence of AM technology has renewed the interest in polishing processes [39, 77]. AM technologies are severely limited in terms of creating controlled surface morphology [62] and suffers from poor surface quality and porosity issues [139]. Consequently, the existing AM technologies are typically coupled with some form of post-processing mechanism to improve the surface finish and reduce surface porosity. Mechanical polishing is one of the most commonly employed post-processing approaches in this context. Surface finish requirements vary depending upon the applications, from biomedical implants that call for differential surface roughness (sub-micron finish at bearing locations while rough, textured surface at the bone-implant interaction site [140]) to mechanical applications that require a uniform specular finish (average surface roughness, $S_a < 25$ nm). Therefore, it is important to understand the exact phenomenology governing surface modification during the post-processing stages and develop accurate modeling approaches to achieve the desired specifications.

However, unlike machining processes such as milling and turning, modeling and simulation of the polishing process is extremely challenging due to the complexities arising from the stochastic nature of the asperity-abrasive interaction (such as depth of cut and rake angle) as well as the deformation mode at asperities (abrasion versus surface material flow). Additionally, in the context of AM surfaces, where surface roughness is almost two orders of magnitude higher, little to no studies exist on the mechanism of surface modification during polishing. Lack of a unified theory hinders accurate modeling of the surface modification during polishing. For example, if polishing is driven purely via abrasion, it is highly unlikely to get rid of surface pores as the subsurface pores (created during the metal powder sintering process) would get exposed on continued material removal. On the contrary, if surface material redistribution is considered as the driving mechanism for surface smoothening, then opportunities may exist to exploit surface plastic flow in polishing processes to minimize residual surface porosity in AM components.

In this chapter, we present direct experimental evidence that support the surface plastic flow as the dominant mechanism in the polishing of rough metal surfaces, fabricated via the EBM process. We present scanning electron microscopy (SEM) observations of polished surfaces that reveal viscous flow at the asperity-abrasive sliding contacts, involving material flow towards the asperity sides in the form of thin fluid-like layers. The subsequent stages of polishing involve bridging of these layers among different asperities to result in a smooth finish. The observations suggest that as polishing ensues, surface smoothening is mediated mostly via material redistribution as opposed to material removal. We establish that the viscous flow at the asperity-abrasive contact is mediated by the high flash temperatures of the order of 700-900 K which is in the range of dynamic recrystallization temperature of the material considered, thus supporting the experimental observations. To determine the flash temperatures generated from frictional heating during the sliding of carefully tuned (spherical) asperity surface against the abrasives we use a circular moving heat source model. By taking into account the distribution of abrasive and asperity profiles, we show that such high flash temperatures are highly likely (>33%) to occur during the repetitive interactions. We also conduct *ex post facto* microstructural analysis to further support the occurrence of viscous flow at the asperity-abrasive interface and present possible microscopic mechanisms underlying the plastic flow during the polishing process.

3.2 Results

3.2.1 Surface plastic flow

Electron microscopy of the surface asperities enabled us to capture key phenomenological details of the polishing process. Based on these observations, we subdivide the polishing process into four different stages as discussed in the following. These stages may exist at the same time depending upon the characteristics of asperity-abrasive interaction, e.g., contact area, asperity height, etc. Polishing begins with the interaction between the abrasive particles and the asperities, initially spherical as shown in Figure 3.1(a). At this stage, material removal could be observed macroscopically, however, the electron microscopic investigation shows that in addition to the material removal, thin layers of material begin to stack on the asperity sides. Figures 3.1(b) and (c) show typical asperity structures after 90 s of polishing. Severe shear of the asperity surface and accumulation of the material towards asperity edges (see at arrow) is evident from Figure 3.1(c). This flow pattern is reminiscent of plastic sliding between surfaces oriented at shallow angles, such as in tribological contacts or 'machining' under highly negative rake angles [44, 89]. The sheared surface material then flows to the

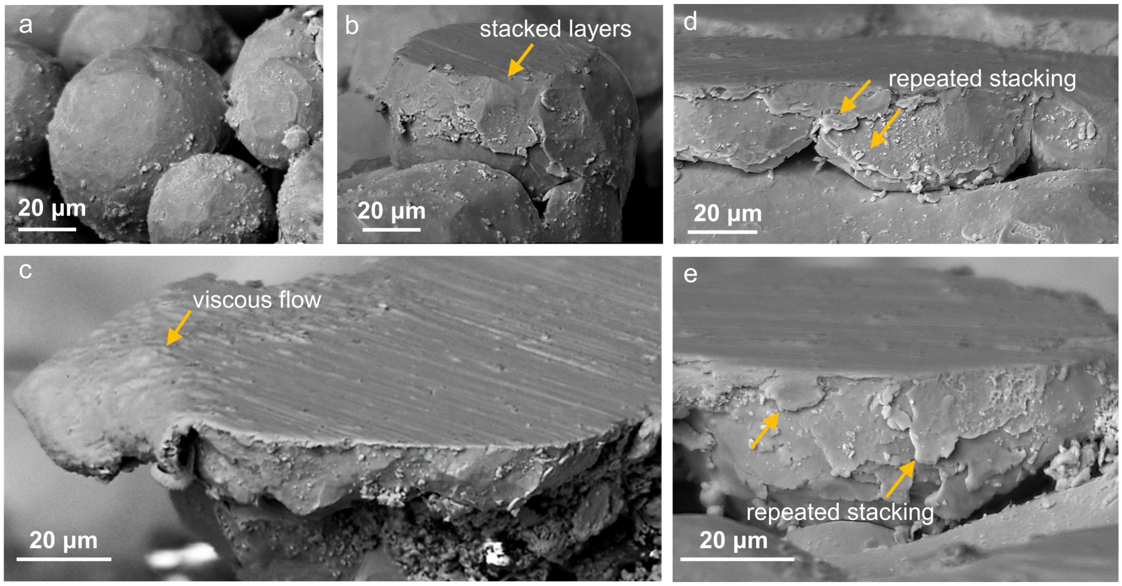

Figure 3.1: SEM images showing (a) the spherical asperity structure at $t = 0$ s, (b-c) surface asperities after 90 s of polishing showing the evidence of complex material flow patterns. (b) lateral plastic flow and deposition of material on the asperity sides, (c) shear deformation of the asperity surface and material flow towards the edge of the asperity in the form of thin, fluid-like layers of the order of $1 - 10$ μm and (d-e) surface asperities showing repeated formation and deposition of thin material layers as the asperity progressively flattens out on continued polishing.

lateral sides of the asperity as thin layers, usually in the range of $1 - 10$ μm. Interestingly, the flow is seen to be quite symmetric around the periphery of the sheared surface, with deposited material layer showing a molten-like appearance. The sliding direction between the asperity and abrasive particle can be inferred from the sliding marks in Figure 3.1(c). This omnidirectional flow at the surface, coupled with the observation of rheological flow features at the asperity edges (Figure 3.1(c)), suggests viscous behavior of the surface plastic flow in polishing.

The electron microscopic investigation of the subsequent polishing stages provides further evidence of the surface flow theory in that the surface smoothening is mediated by material redistribution more so than material removal. Figures 3.1(d-e) show the progression of the plastic flow at the asperity surface on continued polishing (beyond 90 s). This forms the second stage of the polishing process. The repeated shearing at the asperity surface upon

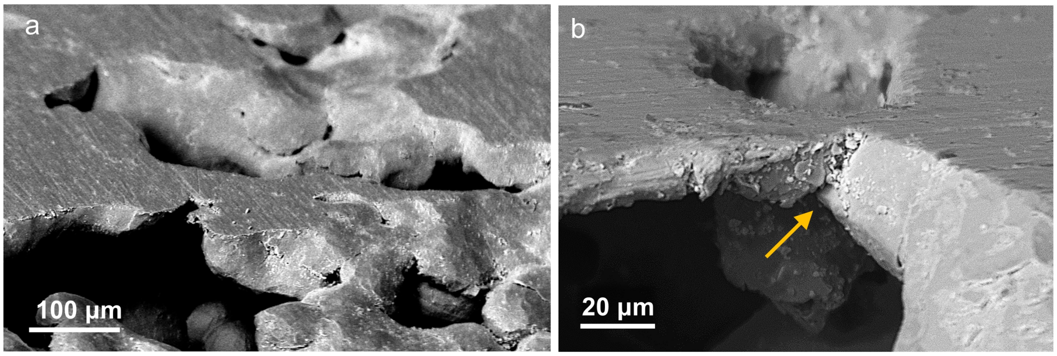

Figure 3.2: Surface smoothening during later stages of polishing by bridging between neighboring asperities. (a) SEM image showing the interconnection of flat ("smooth") regions surrounded by unfilled depressions; (b) a high-magnification image of the bridge (see at arrow) that has formed between neighboring asperities.

encountering a sliding abrasive result in the stacking of multiple thin layers on the lateral sides of the asperity (see at arrow). In effect, this lateral flow of material results in a radial increase in the flattened area of the asperity.

Figure 3.2 illustrates the surface morphology characteristics on continued polishing, at 180 s. In this third stage of polishing, individual asperity surfaces are unresolvable, and the surface can be described as an interconnected network of flat islands as seen in Figure 3.2(a). Interspersed among these regions are the unfilled depressions. A closer inspection of the flattened regions (Figure 3.2(b)) reveals that their formation is mediated by bridging of the smeared surface material between the neighboring asperities. Therefore, the third stage of the polishing process is characterized by the bridging of neighboring asperities. Indeed, this "welding" between the asperities may be expected given the occurrence of severe plastic flow and temperatures (see Section 3.2.2) at the asperity surfaces. In our experiments, this bridging phenomenon was noted only when the distance between the edges of two neighboring asperities approached 30 μm. For asperities separated by larger distances, lateral flow of the material was seen to continue until the effective distance between the asperities approached the critical value. Continued polishing causes complete bridging of individual asperities, resulting in a nominally smooth surface. This final stage (fourth stage) in the polishing

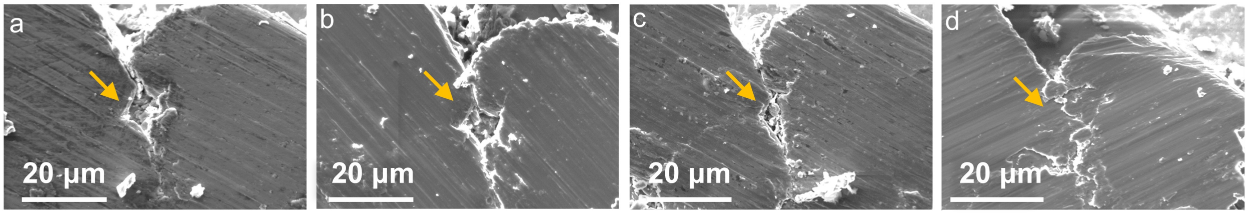

Figure 3.3: SEM observations of the temporal evolution of a representative surface depression $\sim$ 10 μm in size (indicated by arrow). Images in (a)-(d) are taken repeatedly at the same location at 90 s time interval beginning with $t = 180$ s). The depression is progressively filled up as a result of material flow from the neighboring surface.

involves elimination of microscale depressions. Flattening of these microscopic depressions during the final stage of polishing again seems to occur as a result of material flow from neighboring flat regions. A series of SEM images showing the progression of a representative surface depression is presented in Figure 3.3. The images were taken at the same location repeatedly at 90 s time interval beginning with $t = 180$ s. We note that the effective diameter of the depression gradually decreases as a result of the material flow from the neighboring flat surface, that is, surface depressions are smoothened out via plastic flow of the neighboring surface and not by abrasion. This is also in agreement with the observations presented in [8] where the authors showed, in a similar fashion, closing of a microindentation mark after repeated sliding contacts.

The observations presented in the foregoing suggest that polishing primarily involves material redistribution in the form of thin fluid-like layers towards the asperity sides as well as during the bridging process. In contrast, material removal (or abrasion) is mostly limited to the initial stages of polishing.

3.2.2 Asperity-abrasive contact temperature

To explore the possible origin for this flow behavior, we estimated the “flash” temperature at the asperity-abrasive sliding contacts using the circular moving heat source model [42], where the abrasive particle was treated as a semi-infinite moving body over which a stationary heat source acts. The heat source intensity was taken as the heat dissipation due to plastic

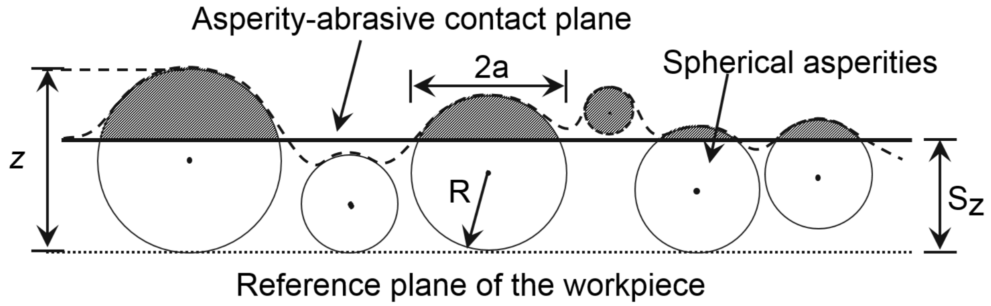

Figure 3.4: Schematic showing contact (solid line) between the workpiece surface consisting of spherical asperities and the polishing pad at a distance S_z (average asperity heights) from the workpiece reference plane (dotted line). Here, the asperity height, z, is measured with respect to the workpiece reference plane.

shearing of the asperity at the sliding asperity-abrasive contact.

For a given asperity height (z) distribution, only the asperities for which $z > S_z$ and $z \leq S_z + 2R$ are involved in the polishing process, as schematically shown in Figure 3.4. Here, the asperity height, z, is measured with respect to the workpiece reference plane (dotted line in the schematic in Figure 3.4). We assume that the clearance between the workpiece reference plane and the polishing pad (solid line) is equal to the average surface asperity heights, S_z, of the workpiece. The diameter of asperity–abrasive contact ($2a$) can then be calculated for a given value of S_z, asperity radius (R) and height (z) distribution.

Given the radius of contact, we calculate flash temperature by treating the contact as a moving circular heat source (Figure 3.5). The heat source intensity is taken as the heat dissipation due to plastic shearing of the metal asperity at the sliding interface. The heat partition between the asperity and the abrasive particle is determined by setting equal the maximum (quasi-steady state) temperatures of the asperity and abrasive particle within the contact, according to Blok's postulate [28]. Here, we treat the abrasive as a semi-infinite moving body (with velocity V) over which a stationary heat source (with uniform heat flux) acts. The steady state flash temperature occurring at the contact center can accordingly be given by the first order approximation to Jaegar's circular moving heat source model

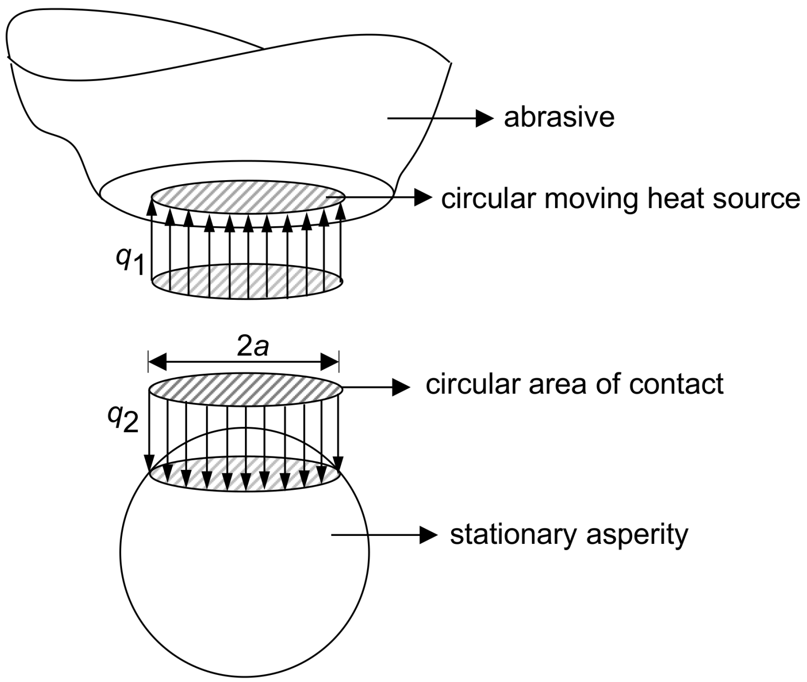

Figure 3.5: Moving circular heat source model for the contact between asperity and abrasive to calculate the temperature rise during polishing. Here, the abrasive is considered as the semi-infinite moving heat source and the asperity acts as a stationary heat source.

[42, 142] as:

$$\Delta T_{max}\big|_{abrasive} = \frac{2q_2 a}{k_2\sqrt{(\pi(P_{e2}+1.273))}} \tag{3.1}$$

where, Peclet number, $P_{e2} = Va/2K_2$ and $K_2 = k_2/\rho_2 C_2 \approx 4 \times 10^{-5}$ m^2/s. For $V = 5$ m/s and contact radius a, we have $P_{e2} = 6.25 \times 10^5 a$. For the asperity (which is treated as a stationary source), we have:

$$\Delta T_{max}\big|_{asperity} = \frac{q_1 a}{k_1} \tag{3.2}$$

Assuming adiabatic conditions, where plastic dissipation at the interface is completely converted into heat, the total heat flux, q, at the circular contact is given by:

$$q = q_1 + q_2 = \mu H V \tag{3.3}$$

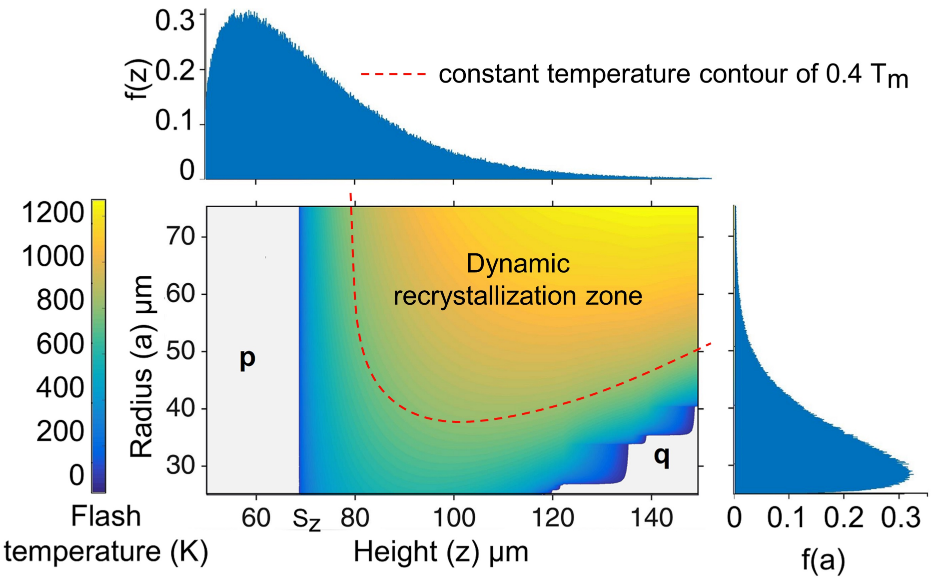

Figure 3.6: Flash temperature map for Ti-6Al-4V as a function of asperity-abrasive contact radius (a) and height (z), both of which follow a truncated Weibull distribution with average at 36 μm and 64.5 μm, respectively, and a standard deviation $\sim$ 15 μm. S_z corresponds to the average asperity height. The dynamic recrystallization zone ($\geq 0.4T_m$) is also indicated on the temperature map.

By equating the maximum temperatures at the asperity and abrasive surface, we have:

$$\Delta T_{max} = \frac{\mu H V a}{k_1}\left(1 + \frac{k_2}{2k_1}\sqrt{\pi(P_{e2} + 1.273)}\right)^{-1} \tag{3.4}$$

We solve for ΔT_{max} for Ti-6Al-4V using the values in Table 1, and the corresponding flash temperature map as a function of asperity height and abrasive-asperity contact radius is shown in Figure 3.6 Any asperity for which $z < S_z$ or $z \geq S_z + 2R$ would not be involved in the polishing process as it would either make no contact with the abrasive or lie outside the asperity–abrasive contact region (solid line in Figure 3.4). These two cases are marked as "**p**" and "**q**" in Figure 3.6. Elsewhere, we notice that larger values of a and z result in higher flash temperatures.

While the assumption of abrasive as a semi-infinite plane maybe reasonable during the initial stages of polishing, the configuration is reversed as polishing process progresses. During the intermediate and final stages, polishing maybe represented as individual abrasive particles sliding across a semi-infinite workpiece surface. For this latter configuration, we assume abrasive particles as sliding conical indenters plastically deforming the workpiece surface. Again for this case, the problem is that of a moving semi-infinite body (workpiece surface) over which stationary heat source (abrasive-workpiece surface contact) acts. The maximum flash temperature rise at the contact in this case is given as:

$$\Delta T_{max} = \frac{\mu H V a}{k_2}\left(1 + \frac{k_1}{2k_2}\sqrt{\pi(P_{e1} + 1.273)}\right)^{-1} \tag{3.5}$$

The calculated sliding temperatures for this configuration are slightly larger than those in the earlier configuration where abrasive was taken as a semi-infinite plane (Figure 3.5). The difference between temperature estimates for these two configurations is within 20% (at a contact radius of ∼40 μm) for the contact areas considered here. In both the configurations, for ∼ 30% of the sliding contacts, maximum flash temperatures are above the dynamic recrystallization temperature of the alloy (∼ 700 K). Similar calculations for Ta_2O_5 showed the flash temperature to be in the range of 750 K. In this case, the average radius of the asperity–abrasive contact area was inferred from Figure 3.7 as ∼ 15 μm. V was taken as 5 m/s, as for Ti-6Al-4V polishing. Again the calculated flash temperatures at the asperity–abrasive contacts are high enough, $\sim 0.4T_m$, where viscous-like flow may be expected.

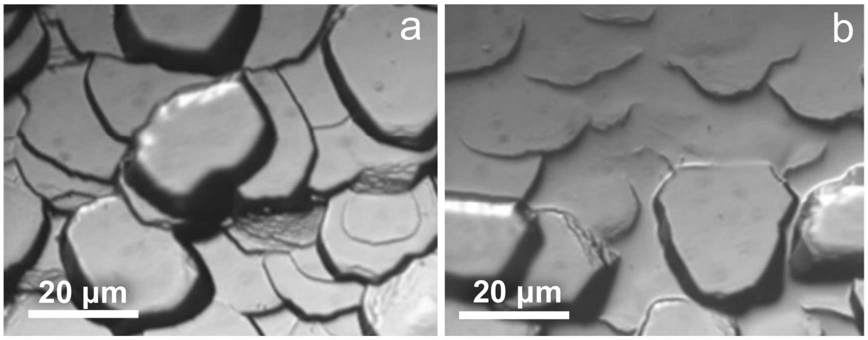

Figure 3.7: Scanning electron micrographs showing surface morphological changes in Ta_2O_5: (a) before and (b) after polishing.

From Figure 3.6, we note that the calculated flash temperatures for $\sim 30\%$ of the sliding contacts were above 700 K. While these temperatures are well below the melting temperature ($T_m = 1925$ K) of Ti-6Al-4V, they are in the typical dynamic recrystallization temperature range ($700-900$ K) for this alloy where significant flow softening occurs [94]. At such temperatures, rate-dependent viscous plastic flow is not uncommon in metals [16]. Recent studies [122] show that the flow softening is primarily caused due to the formation of dynamically recrystallized nanograins with very low dislocation density within the shear bands. Similar fluid-like flow phenomenon in metals have been also noted previously in other sliding configurations [138] and shear bands [123].

3.2.3 Microstructural analysis

SEM analysis of the microstructure further supports the predictions that flash temperatures above 700 K are possible. In comparison to the as-fabricated microstructure (see Figure 2.2(d)), we observe regions with significant coarsening of the β phase on the polished surface (Figure 3.8(a)). β phase with an average width of 0.7 μm was observed along with a significant decrease in the volume fraction of α phase from $\sim 90\%$ before polishing to $\sim 60\%$ after polishing. This is also evident from the distribution of the widths of β phase before and after polishing as shown in Figures 3.8(c&d). This transformation is likely due to the high flash temperatures in the range of $700-900$ K during polishing, coupled with extremely high cooling rates ($\sim 10^6$ K/s) as estimated from the moving heat source model. Additionally, such high flash temperatures can cause migration of β colony boundaries resulting in coarsening of the β phase as noted in Figure 3.8(a). Furthermore, polished surfaces are also often characterized by regions of very coarse β phase, a fact that is consistent with the stochastic nature of asperity-abrasive interactions where flash temperatures may last from less than 10 μs to several seconds (due to repeated rubbing) [86].

Widening of the β phase is further confirmed by the X-ray diffraction of the polished surface as shown in Figure 3.8(e). Higher concentration of β phase is evident in the XRD

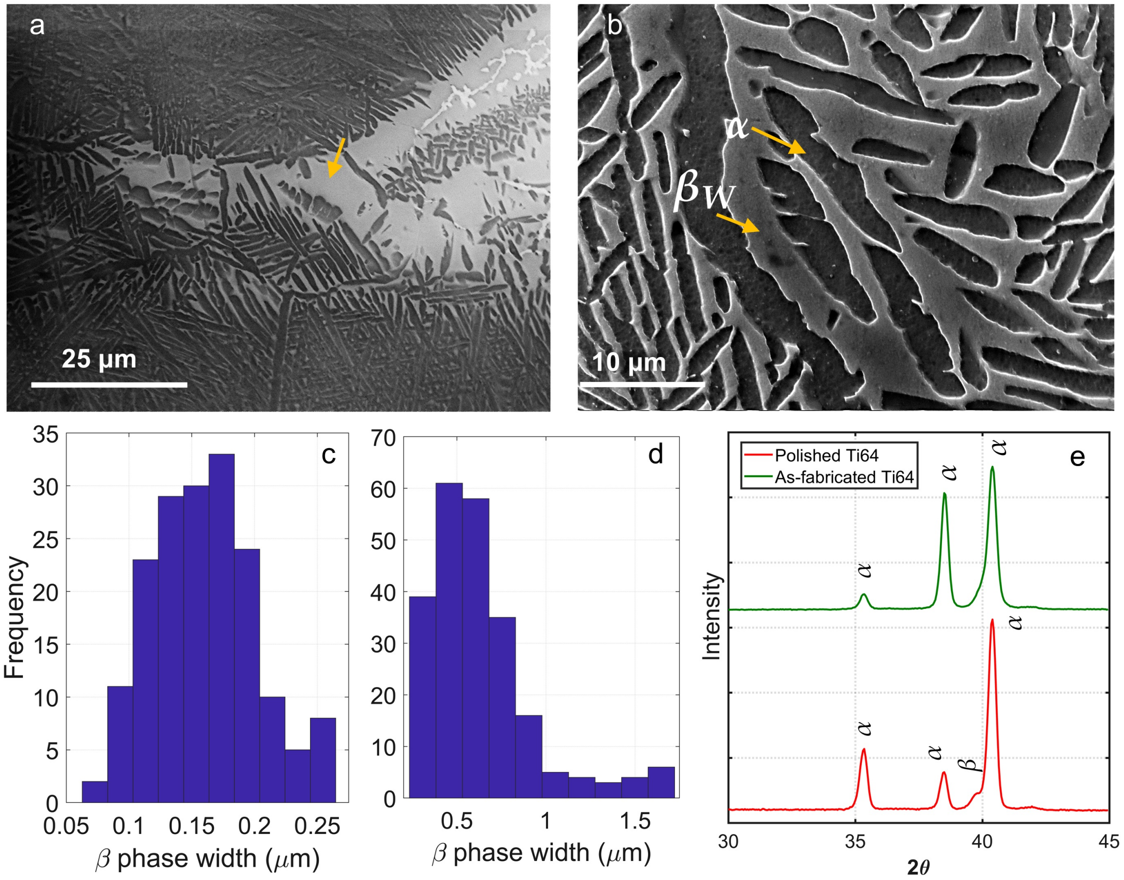

Figure 3.8: Microstructural characterization of the polished surface. (a-b) SEM images showing extreme coarsening at scattered locations (see arrow in (a)) and overall widening of the β phase (≥ 3 μm average width). (c) and (d) show the width distribution of the β phase before and after polishing, respectively. (e) XRD profile of the surface in as-fabricated (top, green) and polished (bottom, red) condition.

profile of the polished surface as compared to the as-built sample. It has also been shown in [69] that the emergence of β phase in XRD profile was observed when the sample was heated in the range of $\sim$ 1200 K. The microstructure evolution observed in the polished samples suggests that the work hardening (as a consequence of dislocation generation) during polishing is likely to be accompanied by some dislocation annihilation mechanism, akin to annealing at high temperatures. Given the flash temperatures at the asperity-abrasive contacts are in the range of $\sim 0.4T_m$, dynamic recrystallization/recovery may be the dominant mechanism in this regard. An important consequence of repeated surface plastic flow is the refinement of α lamellae at the surface and the associated increase in the strength. Indeed, hardness measurements (Vickers indentation, load 500 g) showed the surface to be characterized by a higher hardness (375 kg/mm^2) compared to the base material (350 kg/mm^2).

3.2.4 Microscopic view of the plastic flow

Plastic deformation in metals and alloys generally takes place via an interplay between generation, motion, and annihilation of dislocations [143]. Given the stochastic nature of the polishing process, many of these deformation mechanisms may co-exist. In this section, we utilize our estimates of temperature coupled with the order-of-magnitude analysis of typical strain rates and stresses to identify the dominant mechanisms underlying the plastic flow during the polishing process.

Given the surface plastic strains [127] in polishing are well above 1, at a polishing speed of 5 m/s, the strain rate ($\dot{\gamma}$) should be of the order of $10^3 - 10^5$ s^{-1}. At such high strain rates and typical flash temperatures of about 900 K, the dislocations motion should be drag controlled, with the drag on the mobile dislocations primarily arising from phonon interactions [124]. For example, in phonon-limited dislocation glide the strain rate is proportional to $\rho_m \sigma_s / B$ where σ_s is the applied stress, ρ_m is the mobile dislocation density ($\approx 10^{15} - 10^{17}$ m^{-2} for heavily deformed metals) and B is the phonon viscosity drag coefficient ($\approx 10^{-5}$ Pa·s) [100]. Considering an average applied stress of 100 MPa, the estimated strain rate under the phonon limited glide is about 10^4 s^{-1}, which is within the expected range of strain rate. A similar analysis for diffusion-based mechanisms (e.g., lattice or grain boundary diffusion) reveals that these mechanisms are likely to be minor contributors to the flow at strain rates and temperatures relevant to polishing. However, at flash temperatures exceeding 1200 K, dislocation motion via climb as well as grain boundary sliding (GBS) are the plausible secondary mechanisms that could contribute to the plastic flow. Recent studies have shown that GBS can also accommodate some other deformation modes, including grain rotation [147] and twinning [146]. Delineation of the individual contributions of these various mechanisms to to the overall plastic flow in polishing is a challenging task that remains to be tested.

3.3 Discussion

The foregoing observations of surface morphology suggest that material redistribution is the dominant mechanism of polishing as opposed to material removal, especially for extremely rough surfaces that are peculiar to conventionally adopted additive manufacturing processes (layer by layer deposition of metal powder). Analytical investigations of asperity-abrasive flash temperatures as well as the microstructural evolution (widening of the β phase) suggest that the formation of thin fluid-like viscous layers is driven by the occurrence of high flash temperatures in the range of $700 - 900$ K.

3.3.1 Mechanism of polishing and generality of the observations

It may be noted that our observations of surface plastic flow and material redistribution presented in this work are somewhat contrary to the conventional theories of polishing, originally advocated by Hooke, Newton [108], Herschel [15] and Rayleigh [40], viewing polishing essentially as an abrasion or a grinding process at a very fine scale. Here, surface irregularities were believed to be removed by cutting action of the abrasives. Studies presented by Samuels and Aghan [5, 127] showed that polishing and abrasion are phenomenologically the same process and differed only in the degree of material removal. Direct observations of the polished copper surfaces under SEM demonstrated the formation of micro-chips that established cutting and ploughing as the dominant mechanisms of surface smoothening [155]. The study also established that the molecular material removal theory proposed by Rabinowicz [119] is highly unlikely to occur.

Interestingly, however, our observations point to an alternate surface flow and material redistribution theory of polishing proposed by Beilby and Bowden [24]. However, several important distinctions are noted with respect to this theory. First, no evidence for surface melting or amorphization was noted in contrast to the original hypotheses [24, 30], although the microscopy observations of the surface flow profiles, together with the temperature calculations of the asperity-abrasive sliding contacts, strongly suggest the occurrence of viscous flow. Second, as demonstrated in Figure 3.1, the material redistribution is facilitated by the material flow as thin layers ($1-10$ μm) that make self-contact with the asperity sides. This is again at variance with the original ideas where the surface valleys are believed to be filled purely via compression (and lateral flow) of the asperities. Lastly, bridging among asperities is seen to be an important mechanism by which neighboring asperities merge to form a smooth surface network.

We note that the material properties, as well as the starting asperity structure obtained via AM (that was not feasible in the previous studies), may play a key role in determining the dominant mechanism in polishing. For example, the low thermal diffusivity of Ti-6Al-4V ($\approx 3.6 \times 10^{-6}$ m^2/s) undoubtedly contributes to the high temperatures localized near the asperity-abrasive interface, causing sufficient softening and material flow. We believe that it is the lack of controlled starting asperity structure (to track unit plastic flow events) and the limitations on the microscopic power that contributed to the dismissal of Beilby's surface flow theory [127]. While other factors such as down force and the polishing speed could also influence the findings presented in the chapter, e.g., flash temperature rise and the subsequent viscous flow, the values chosen for polishing load and speed in our study are representative of most metallographic polishing processes [127]. Among others, such as lubricants only control the nominal surface temperature rise and has been shown to have negligible effect on the local flash temperatures [141].

Nonetheless, we believe that the current findings are likely to be more generic to the polishing of a range of other material systems. Similar observations in oxide materials have been noted [78]. While these observations are at first surprising given their inherent brittle behavior, can be explained by the high asperity-abrasive contact pressures that typically exceed the work piece material's hardness. It is well known that such high pressures can, in turn, promote plastic flow even in highly brittle materials [35]. Additionally, the asperity-abrasive contact temperature calculations for polishing of Ta_2O_5 (see Figure 3.7)showed that the flash temperatures can be a significant fraction ($\sim 0.4T_m$) of its melting temperature, which could potentially enhance the propensity for viscous-type flow at asperity surfaces. Nonetheless, understanding the mechanism behind such flows require further studies and still remains an open problem. Besides polishing, our observations are also of relevance to a range of other engineering and physical systems where micro-scale asperity contacts, characterized by high pressures, are of intrinsic interest, e.g., tribological systems, erosion, and earthquakes.

3.4 Summary and conclusions

The physics by which rough surfaces are smoothened during polishing has remained a controversial topic because of the inherent complexity and the stochastic nature of the process. The speculations on the exact phenomenology of the polishing process, therefore, have largely been based on the postmortem analysis of the polished surfaces. However, no conclusive evidence exists till now to support either the surface flow or the fine scale abrasion (material removal) theory.

In this chapter, we have presented experimental characterization, thermal and microstructural studies to settle this paradox by gathering direct evidence of basic flow events through which surface morphological changes occur in polishing. Using a carefully designed (spherical) asperity structure, we analyze the deformation state of the asperities after every 90 s of the polishing process using scanning electron microscopy. Towards this end, we present observations that not only provide conclusive evidence for the general Beilby–Bowden's surface flow picture, but also bring out new phenomenology of polishing pertaining to viscous flow at asperity-abrasive contacts, self-contact of *flown* layers with the asperity sides, and subsequent bridging among these layers that closely resembles evolution of a complex network. Subsequently, the stochastic circular moving heat source model as well as the microstructural observations suggest that the formation of viscous thin-fluid like layers is driven by the occurrence of high flash temperatures of the order of 700-900 K that are in the range of dynamic recrystallization temperature of the material system (Ti-6Al-4V) considered in this study. These results altogether establish an alternative mechanism of surface smoothening that is mediated by viscous flow and redistribution of surface asperities and contradicts the widely adapted fine scale abrasion and chip formation theory.

The experimental observations have also allowed us to quantitatively capture the evolution of surface morphology during the polishing process using a random planar graph theoretic approach. Results suggest that the spectral characteristic (λ_2) of the planar graph is a better quantifier of the surface morphology and an efficient estimator of the process endpoint as compared to the average surface roughness, particularly in the case of rough metal surfaces. These results are significant as accurate predictions of process endpoints and surface morphological modeling are becoming crucial in the additive manufacturing industry where post-processing efforts account for over 25% increase in the production costs and 17-100% increase in the cycle times [39].

The new perspective on surface plastic flow and bridging phenomena presented in this work creates opportunities to exploit the viscous flow behavior of polishing to tailor the mechanical properties along with controlling the surface roughness and porosity. From an analytical perspective, these observations can also help in developing models that can accurately predict the surface morphologies at different polishing stages by accounting for material redistribution rate along with the material removal.

4. PHYSICS-BASED RANDOM PLANAR GRAPH REPRESENTATION OF SURFACE MORPHOLOGY *

Robust and accurate representations of surface morphological evolution during the post-processing, especially surface finishing of additively manufactured components are imperative to ensure effective monitoring and control strategies. Due to the lack of robust surface representations, current methods of surface quality inspection tend to be mostly manual and account for 20-70% of the cycle time in part production. In light of this, this chapter presents a physics-based random planar graph approach that is based on tracking the surface morphology at different finishing stages via *in situ* images. To ensure a statistically consistent representation, we consider the surface morphology—consisting of undulations or asperities to be a random field that evolves during the surface finishing process. As the finishing progresses, the asperities, considered as nodes deform and merge with the neighboring asperities resulting in a smooth surface. To complete the network formulation, we estimate the edge weights as the probability of neighboring asperities to merge. At every stage of the finishing process, we employ a Bayesian transformed Gaussian model to predict the increase in the radius of the asperities followed by a copula model to estimate the probability that a pair of neighboring asperities would merge. We show that tracking the second smallest eigenvalue of the resulting network (also known as Fiedler value) offers a robust approach to monitor the surface morphology. We also discuss the relevance of the Fiedler value to the physics of the polishing process and associate these results with the endpoint in polishing.

4.1 Introduction

Advances in image-based monitoring offer an interesting opportunity to track the physical as well as chemical transformations taking place at every conceivable resolution-of-interest

---

*Reprinted with permission from S. T. S. Bukkapatnam, A. S. Iquebal, and S. R. T. Kumara, "Planar random graph representations of spatiotemporal surface morphology: Application to finishing of 3D printed components," CIRP Annals, vol. 67, no. 1, pp. 495–498, Copyright 2018 Elsevier

([56]). While image data have been used for process characterization such as defect identification ([76, 37]) and process control ([101, 72]), quantification and subsequent endpoint detection, i.e., deciding when a product/process has reached its specified quality levels remain limited ([120]). Effective quantification of the process evolution is the *sine qua non* to enabling automated decision making in advanced manufacturing processes. Examples include quantification of the surface morphology as surface irregularities are smoothed out during a mechanical polishing process ([120, 39]), growth/agglomeration of nanoparticles to reach certain size distribution ([118]), deterioration of the machine tool during machining, etc.

Image-based monitoring and quantification of process evolution are hampered due to the lack of a consistent and robust representation scheme to capture the morphological changes from the images. A majority of the existing works have focused on tracking the image features by using profile monitoring techniques. For instance, images may be transformed into linear profiles using Q-Q plots that can be subsequently monitored using profile monitoring approaches ([145, 101]). Other commonly employed methods include Fourier and wavelet transforms that utilize the frequency characteristics ([136, 81, 82]), fractal dimensions ([38]), functional representations ([164]), etc.

Since these methods are based on tracking the salient descriptors (e.g., size and shape of pores ([101])), they require an “in-control” distribution of the descriptors. Consequently, these approaches have focused largely on monitoring defects or anomalies from image data streams ([37, 72]), and not necessarily on quantifying the process evolution where the descriptors may evolve over time. Only a handful of methods have been developed in the past to deal with the issue of efficient representation schemes to capture the process evolution. For example, [120] developed a graph-theoretic approach to represent the surface morphology variations by using pixel intensities, [133] proposed a point set representation to capture the geometric features of various objects (such as nanoparticles) identified in the microscopic images, [113, 112] used a time-varying radius function to track the growth of nanoparticles. Although these approaches present interesting insights into the process evolution, they only exploit the image characteristics without considering the physics of the process. As a result, these approaches merely provide an empirical snapshot of the underlying process and may not offer an efficient representation scheme to capture the process evolution.

Moreover, representations that are derived empirically from images may be extremely limited because (a) images capture only small snapshots in time and space and (b) complex, seemingly irregular, evolution patterns do not lend themselves to conventional statistical descriptions. These evolution patterns are also influenced by the phase and chemical transformation phenomena, which are inherently stochastic. Consequently, robust representation and quantification of the spatiotemporal evolution in the surface morphologies and connecting these with the underlying process physics and the endpoint detection remain open issues. From a statistical standpoint, these images may be viewed as realizations from a random field evolving over time. Since the images capture the snapshots into the physics of the underlying real-world processes, the corresponding random fields are noticeably non-Gaussian (e.g., see [70]). Gaussian or Gaussian-like random field assumptions may therefore not capture the dynamics of the underlying physics of the process. Moreover, ad-hoc transformations of the random field (e.g., log-transform) have been shown to induce bias and underestimate the prediction uncertainty ([53]). Another important challenge that arises when working with a non-Gaussian random field is specifying the joint behavior of the random variables ([37]). Without assuming any specific covariance structure, directly estimating the joint distribution remains a non-trivial problem. More recently, [39] presented a random planar graph representation to capture the evolution in surface morphology during a mechanical polishing process. However, the representation was empirically derived without considering the underlying correlation structure and the joint distribution of the surface morphological features.

In this work, we are concerned with utilizing the physics of the process to develop a robust and accurate representation of the process evolution, thereby enabling quantification and endpoint detection. We consider the case of surface morphology evolution during mechanical polishing processes and the underlying physics ([78]) to develop a random planar graph representation of the spatiotemporal evolution in the surface morphology. The evolution in the surface morphology during the polishing process is reminiscent of an evolving planar graph where the undulations in the surface, also known as particles (or nodes in the graph) bridge with neighboring undulations to form a flat, smooth surface (see [78] for details). In light of this, we show that the surface morphology at any time t is essentially a realization of a (non-Gaussian) random field over the particles. However, owing to the stochastic nature of the polishing process ([159]), only limited information about the state of this random field is available through *in situ* images. We first employ a Bayesian transformed Gaussian (BTG) model to predict the missing information in the random field. Subsequently, we develop a copula-based model to construct a planar graph representation over the random field representing the surface morphology. In the sequel, we show that the spectral characteristics of the resulting graphs, specifically the second smallest eigenvalue (λ_2) serve as improved quantifiers to capture the progression of the polishing process. We also discuss the relevance of the λ_2 value to the physics of the polishing process and associate these results with the endpoint in polishing. Finally, we establish the sensitivity of λ_2 in capturing the evolution in the surface morphology as well as the effect of node density lying near the boundary of the image.

The remainder of this chapter is organized as follows: Section 4.2 presents the random planar graph representation and shows how this representation captures the evolution of manufacturing processes as gathered by images. Subsequently, in Sections 4.2.1-4.2.3, we elaborate on the random field view of the morphological variations followed by the Bayesian transformed Gaussian model and a physics-based copula approach for random planar graph representation. In Section 4.3, we discuss the spectral characterization of resulting graphs. Section 4.4 presents the application of the proposed methodology on the sequence of images obtained during polishing along with sensitivity analysis. Concluding remarks are presented in Section 4.5.

4.2 Planar graph representation

In this study, a sequence of mechanical polishing and imaging steps were executed to record the surface morphological evolution of an additively manufactured (AM) Ti-6Al-4V workpiece (see [78] for details on the polishing process). Figure 4.1(a) shows a representative progression of the surface morphology as recorded by a scanning electron microscope (SEM) during multiple polishing stages. Note that the successive images presented in Figure 4.1(a) are longitudinal, i.e., repeated measurements at the same location at different points in time.

From a process standpoint, surface smoothening during polishing occurs as a result of redistribution of material from the particle tops to the neighboring depressions (see Figures. 4.1(b)&(c)). This redistribution of the material results in an effective increase in the diameter of the particles, gradually filling the depressions on the surface as depicted in Figure 4.1(c). The particle diameter continues to increase until the neighboring particles bridge (or merge), resulting in the formation of a smooth interconnected flat surface ([78]). This progressive bridging of the neighboring particles motivates a graph-based representation of the surface morphology where the particles represent the nodes and the edges connecting these nodes capture the probability that a pair of neighboring particles would be bridged after a particular polishing stage. Such a merger or clustering of elementary particles is quite common and has been an active area of research, e.g., diffusion and self-assembly of nanoparticles ([118]), microstructure and defect evolution([68]). In the following, we present an approach for a random planar graph representation of the SEM images gathered during the polishing process. But first, we begin with a statistical description of the surface morphology.

4.2.1 Surface morphology as random fields

Statistically speaking, it is convenient to represent the surface morphology as a random field $\{r(t,x),\ t \in \mathbb{R}_+, x \sim \mathcal{P}(\mu)\}$ over the particles where $\mathcal{P}(\mu)$ denotes a Poisson process in $\mathbb{R}^2$ such that $\boldsymbol{r}(t) = (r(t,x_1), r(t,x_2), \ldots, r(t,x_n))$ is a single realization of this random field denoting the particle radii observed at time t and locations $x_1, x_2, \ldots, x_n$. Since the

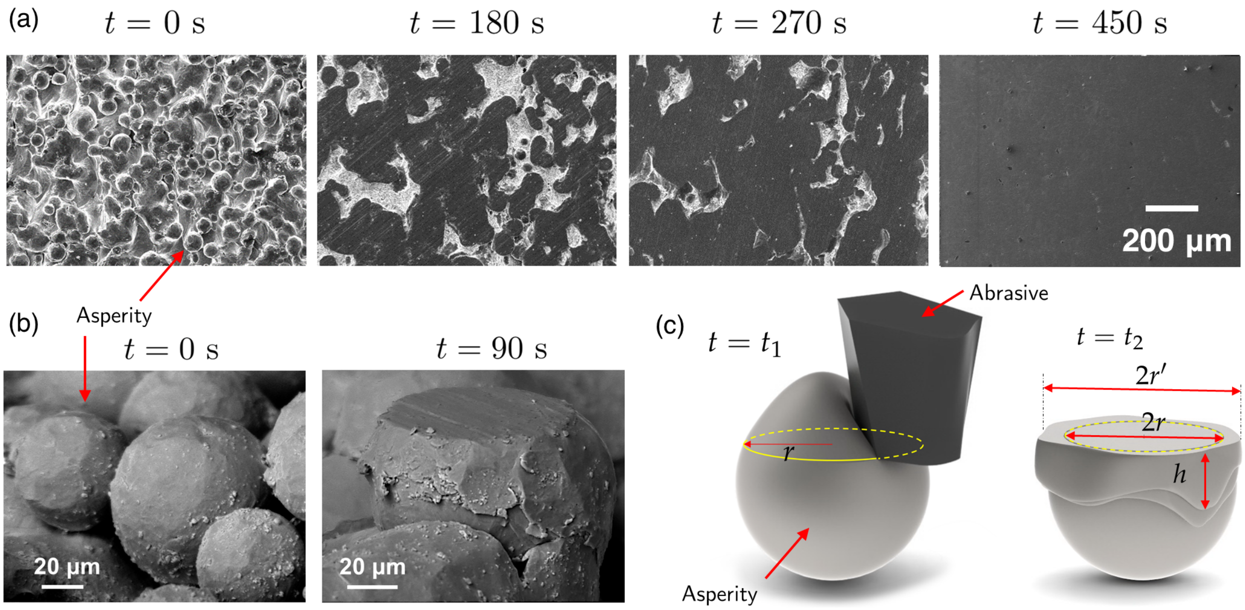

Figure 4.1: (a) Representative progression of surface morphology during polishing with $t = 0$ s showing the initial surface morphology and $t = 450$ s as the final surface morphology. (b) Isometric view of the particle morphology at $t = 0$ s and $t = 90$ s (c) schematic showing the increase in the diameter of the particles from time t_1 to t_2.

particles are randomly dispersed on a two-dimensional surface during the fabrication process (i.e., while powder deposition in AM), it is reasonable to consider that x_i's are drawn from a Poisson process $\mathcal{P}(\mu)$ with some parameter μ ([54]).

During the polishing process, the surface morphology evolves via an increase in the particle radius, and the evolution in the neighboring particles show similar, often correlated behavior. Let us denote the increase in the particle radius by $\delta r(t, x)$ such that $\boldsymbol{\delta r}(t) = (\delta r(t, x_1), \delta r(t, x_2), \ldots, \delta r(t, x_n))$ is the increase in particle radius observed at time t. Since the exact specification of the joint distribution of $\delta r(t, x_i)$'s is not feasible, we consider that the values of $\delta r(t, x_i)$ are drawn from some unknown marginal distribution $F_i(.)$, generally non-Gaussian. A highly right-skewed distribution for $\delta r(t, x_i)$ is more appropriate because at any given time instant, only a limited number of particles are engaged with the abrasives and undergo material redistribution. These are the particles that lie near the tail of the particle height distribution (see [70] for example).

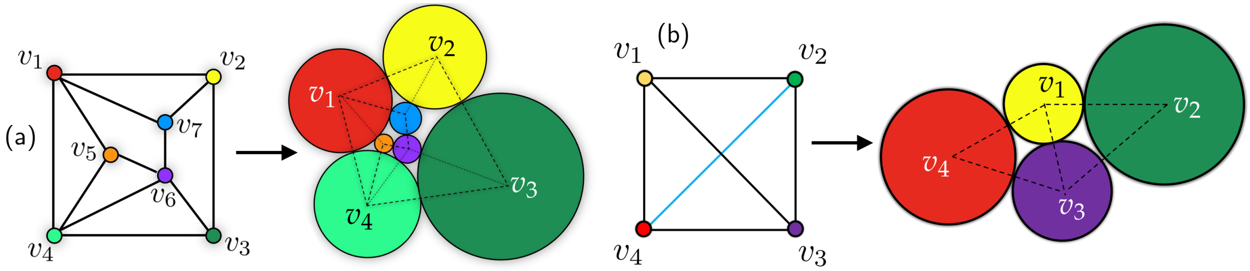

Figure 4.2: (a) Embedding a planar graph using disks (b) Attempt at embedding non-planar graph using disks.

4.2.2 From images to graph representation

The polishing process can be thought of as a transfer function that modifies the random field $r(t, x)$ over time via material redistribution and bridging. In essence, the phenomena of bridging of the neighboring particles represent an evolving random planar graph $G(t) = (V, E(t))$ where the nodes V represent the particles and the edge weights $E(t)$ denote the propensity of a pair of neighboring particles (nodes) to bridge over time. As observed from the *in situ* electron micrographs (see Figure 4.1(a), the evolving morphological features (here, the particle morphology) are embedded in a two-dimensional plane. To ensure that the graph representation is consistent with the planar disposition of the surface features, we subscribe to the following planar graph representation in this study.

Definition 1. *A graph $G = (V, E)$ with nodes V and edge weights connecting any pair of nodes denoted by E is planar if it can be drawn in a plane without edges intersecting.*

This formal representation allows for the description of morphological features, including particles as circles in a plane and the edge weights $E(t)$ capture the probability of a pair of neighboring particles to bridge. An example of the planar graph is presented in Figure 4.2(a). Note that the planar disposition of the graph contains circles that only intersect at the boundary. In contrast, the graph in Figure 4.2(b) is non-planar as the planar embedding is infeasible without circles v_2 and v_4 intersecting through circles v_1 and v_3.

Let $N_i(t)$ denote some neighborhood of a node i, e.g., the set of its immediate neighbors.

Then the probability $e_{ij}(t) \in E(t)$ of node i to bridge with its neighboring node $j \in N_i(t)$ can be expressed as:

$$e_{ij}(t) = P(\delta r(t, x_i) + \delta r(t, x_j) > \Delta r_{ij}(t-1) | \Delta r_{ij}^{(t-1)}, \omega_1(t-1), \ldots, \omega_m(t-1)) \tag{4.1}$$

where $\Delta r_{ij}(t-1)$ is the inter-particle distance recorded instantly before time $t-1$ and $\omega_1(t-1), \omega_2(t-1), \ldots, \omega_m(t-1)$ represent the parameters concerning the thermomechanics of the polishing process for instance friction, temperature [71]. In other words, two neighboring particles i and j will be considered bridged at time t, if the increase in the radius of the particles i and j when polished from time $t-1$ to t is greater than the inter-particle distance at time $t-1$ given the thermomechanical properties recorded at time $t-1$. However, given the length scales at which polishing happens, it is difficult to measure such properties experimentally. In the absence of these measurements, we directly estimate the probabilities by using a data driven approach. To estimate the probability $e_{ij}(t)$, we need to estimate the joint distribution function of $\delta r(t, x_i)$ and $\delta r(t, x_j)$. However, the $\delta r(t, x_i)$ values are known only at limited locations and it is non-trivial to estimate $\delta r(t, x_i), \forall i = 1, 2, \ldots, n$ directly from the images. This is a common problem in several physical processes where estimating the state change ($\delta r(t, x_i)$) requires performing costly experimentation. In the following, we first refer to a Bayesian transformed Gaussian (BTG) model to predict the state change, i.e., $\delta r(t, x_i)$ and then present a copula model to estimate the joint distribution of $\delta r(t, x_j)$'s.

Recall that $\delta r(t, x_i)$ is the increase in the particle radius value at time t. If the increase in the particle radius i and j is larger than the inter-particle distance ($\Delta r_{ij}(t-1)$), the two particles are merged and form a flat surface locally. This is reflected in the SEM images in the form of "almost constant" pixel intensity as we traverse from the center of one particle to the other. We estimate the increase in the radius of these bridged particles, say i and j, as one-half of the total inter-particle distance $\Delta r_{ij}^{(t-1)}$ as measured in the previous stage. The assumption is reasonable as the polishing process is omni-directional ([78]). We refer to these locations as the “known” locations.

A natural approach to predict the increase in the particle radius at the remaining “missing” locations in the random field is to employ kriging. However, as mentioned in the foregoing, the random field in most physical processes are non-Gaussian. Although several nonlinear transformations exist in the literature, any particular transformation function may not always hold, especially during various stages of the polishing process. Under such circumstances, kriging would significantly underestimate the prediction uncertainty. To avoid such issues, we employ a Bayesian transformed Gaussian model as proposed by [53]. Under the BTG model, we assume that there exists some transformation $\mathcal{G} = \{g_\kappa(.) : \kappa \in \varkappa\}$ that belongs to a parametric family such that the transformed field $\{\rho(t, x) = g_\kappa(r(t, x)), x \sim \mathcal{P}(\mu)\}$ is approximately Gaussian. Here, $g_\kappa(.) \in \mathcal{G}$ is a nonlinear monotone transformation that is first order differentiable and continuous in $\varkappa \times \mathbb{R}$. The assumption is quite reasonable for unimodal skew distributions as noted in [125]. In the following, we refer to this transformed random field as g_κ-Gaussian random field.

The problem of predicting unknown the $\delta r(t, x_i)$ in $\mathbb{R}^2$ is essentially a spatial prediction problem. Referring to our previous notation, $\boldsymbol{\delta r}(t) = (\delta r(t, x_1), \delta r(t, x_2), \ldots, \delta r(t, x_n))$ denotes a single realization of the random field representing the increase in the particle radius at known locations $x_1, x_2, \ldots, x_n \sim \mathcal{P}(\mu)$ at time t. Our objective is to employ $\boldsymbol{\delta r}(t)$ and predict the increase in the radius values at unobserved locations. Let $\boldsymbol{\delta r}_0(t) = (\delta r(t, x_{01}), \delta r(t, x_{02}), \ldots, \delta r(t, x_{0k}))$ denote a random vector where $x_{01}, x_{02}, \ldots, x_{0k} \sim \mathcal{P}(\mu)$ are the unobserved locations in the random field. Given the transformation $\mathcal{G}$, we have

$$(g_\kappa(\boldsymbol{\delta r}_0(t)), g_\kappa(\boldsymbol{\delta r}(t))) \sim \mathcal{N}_{k+n}\left(\begin{pmatrix}\mathbf{X}_0(t)\boldsymbol{\beta} \\ \mathbf{X}(t)\boldsymbol{\beta}\end{pmatrix}, \frac{1}{\tau}\begin{pmatrix}\mathbf{E}_{\boldsymbol{\vartheta}}(t) & \mathbf{B}_{\boldsymbol{\vartheta}}(t) \\ \mathbf{B}'_{\boldsymbol{\vartheta}}(t) & \boldsymbol{\Sigma}_{\boldsymbol{\vartheta}}(t)\end{pmatrix}\right) \tag{4.2}$$

for some parameter $\kappa \in \varkappa$, covariance parameters $\boldsymbol{\vartheta}$ and precision of the g_κ-Gaussian random field $\tau^{-1} = \mathrm{Var}(\rho(t, x))$. $\mathbf{X}(t)$ and $\mathbf{X}_0(t)$ are the design matrices comprising of particle locations, $x \in \mathbb{R}^2$ and radii $r(t, x)$, $\boldsymbol{\beta} = (\beta_1, \beta_2, \ldots, \beta_p)$ are the unknown regression parameters and $\mathbf{E}_{\boldsymbol{\vartheta}}(t), \mathbf{B}_{\boldsymbol{\vartheta}}(t)$ and $\boldsymbol{\Sigma}_{\boldsymbol{\vartheta}}(t)$ are the $k \times k$, $k \times n$ and $n \times n$ correlation matrices given as: $\mathbf{E}_{\boldsymbol{\vartheta},ij}(t) = K_{\boldsymbol{\vartheta}}(||x_{0i} - x_{0j}||), \mathbf{B}_{\boldsymbol{\vartheta},ij}(t) = K_{\boldsymbol{\vartheta}}(||x_{0i} - x_j||)$, and $\boldsymbol{\Sigma}_{\boldsymbol{\vartheta},ij}(t) = K_{\boldsymbol{\vartheta}}(||x_i - x_j||)$. Here, $K_{\boldsymbol{\vartheta}}(\cdot)$ is the covariance function.

Note that the transformation parameter κ directly affects the inference of the model parameters $(\boldsymbol{\beta}, \tau, \boldsymbol{\vartheta})$. To capture the dependence between κ and the model parameters, [53] proposed the following prior for the unknown parameters,

$$p(\boldsymbol{\beta}, \tau, \boldsymbol{\vartheta}, \kappa) \propto \frac{p(\boldsymbol{\vartheta})p(\kappa)}{\tau J_{\kappa}^{p/n}} \tag{4.3}$$

where $p(\boldsymbol{\vartheta})$ and $p(\kappa)$ are the prior marginals of $\boldsymbol{\vartheta}$ and κ, and J_{κ} is the Jacobian of the transformation. The use of Jacobian in the denominator is argued by [31] as follows: since g_{κ} belongs to a family of smooth functions any transformation $g_{\kappa}(.)$ may be represented as a linear function of a reference transformation $g_{\kappa_1}(.)$, i.e.,

$$g_{\kappa}(r(t,x)) \simeq a_{\kappa} + l_{\kappa} g_{\kappa_1}(r(t,x)) \tag{4.4}$$

where κ_1 is some reference value of κ. Therefore, the choice of the prior for which κ and κ_1 are consistent with Equation (5.3) is $v(\kappa) = l_{\kappa}^{-p}$. A pragmatic choice of l_{κ} was suggested by [31] as $l_{\kappa} = J_{\kappa}^{p/n}$.

Finally, to make conditional inference about $\boldsymbol{\delta r}_0(t)$, we refer to the posterior predictive density using a fully Bayesian approach as:

$$p(\boldsymbol{\delta r}_0(t)|\boldsymbol{\delta r}(t)) = \int p(\boldsymbol{\delta r}_0(t)|\boldsymbol{\delta r}(t), \boldsymbol{\beta}, \tau, \boldsymbol{\vartheta}, \kappa) p(\boldsymbol{\beta}, \tau, \boldsymbol{\vartheta}, \kappa|\boldsymbol{\delta r}(t)) d\boldsymbol{\vartheta} d\kappa \tag{4.5}$$

where $p(\boldsymbol{\delta r}_0(t)|\boldsymbol{\delta r}(t), \boldsymbol{\beta}, \tau, \boldsymbol{\vartheta}, \kappa)$ is the likelihood of the unobserved data $\boldsymbol{r}_0(t)$ given the parameters and the observed data. The likelihood may be obtained analytically since from Equation (5.2), we know that $g_{\kappa}(\boldsymbol{r}_0(t)) \sim \mathcal{N}_k(\mathbf{M}_{\boldsymbol{\vartheta},\kappa}, \tau^{-1}\mathbf{D}_{\vartheta})$ where $\mathbf{M}_{\boldsymbol{\vartheta},\kappa} = \mathbf{B}_{\boldsymbol{\vartheta}} \boldsymbol{\Sigma}^{-1} g_{\kappa}(\boldsymbol{\delta r}(t)) + \mathbf{H}_{\boldsymbol{\vartheta}} \boldsymbol{\beta}$, $\mathbf{D}_{\boldsymbol{\vartheta}} = \mathbf{E}_{\boldsymbol{\vartheta}} - \mathbf{B}_{\boldsymbol{\vartheta}} \boldsymbol{\Sigma}_{\vartheta}^{-1} \mathbf{B}'_{\boldsymbol{\vartheta}}$, and $\mathbf{H}_{\boldsymbol{\vartheta}} = \mathbf{X}_0 - \mathbf{B}_{\boldsymbol{\vartheta}} \boldsymbol{\Sigma}_{\vartheta}^{-1} \mathbf{X}$. Marginalizing over $\boldsymbol{\beta}$ and τ, we note that $(g_\kappa(\boldsymbol{\delta r}_0(t))|\boldsymbol{\delta r}(t), \boldsymbol{\vartheta}, \kappa) \sim T(n-p, \boldsymbol{m}_{\boldsymbol{\vartheta},\kappa}, q_{\boldsymbol{\vartheta},\kappa}\boldsymbol{C}_{\boldsymbol{\vartheta}})$, a t-distribution with $n-p$ degrees of freedom, location parameter vector $\boldsymbol{m}_{\boldsymbol{\vartheta},\kappa}$ given as

$$\boldsymbol{m}_{\boldsymbol{\vartheta},\kappa} = \mathbf{B}_{\boldsymbol{\vartheta}}\boldsymbol{\Sigma}^{-1}g_\kappa(\boldsymbol{\delta r}(t)) + \mathbf{H}_{\boldsymbol{\vartheta}}\hat{\boldsymbol{\beta}}_{\boldsymbol{\vartheta},\kappa}$$

and the scale matrix $q_{\boldsymbol{\vartheta}}\mathbf{C}_{\boldsymbol{\vartheta}}$ is given as,

$$\mathbf{C}_{\boldsymbol{\vartheta}} = \mathbf{D}_{\boldsymbol{\vartheta}} + \mathbf{H}_{\boldsymbol{\vartheta}}(\mathbf{X}'\boldsymbol{\Sigma}_{\vartheta}^{-1}\mathbf{X})^{-1}\mathbf{H}'_{\boldsymbol{\vartheta}}$$

To determine the estimates of $\boldsymbol{\delta r}_0(t)$, we decide to work with Mateŕn covariance function, especially because it offers more flexibility in terms of modeling the covariance matrix. The Monte Carlo algorithm to sample from the posterior predictive distribution is as follows:

1. Define and discretize an interval over which the predictive density of $\boldsymbol{\delta r_0(t)}$ is to be defined.
2. Generate $\boldsymbol{\vartheta}_1, \boldsymbol{\vartheta}_2, \ldots, \boldsymbol{\vartheta}_m$ and $\kappa_1, \kappa_2, \ldots, \kappa_m$ independently and identically from $p(\boldsymbol{\vartheta})$ and $p(\kappa)$, respectively
3. Approximate the posterior predictive density of $\delta r_0(t,x)$ as:

$$\hat{p}(\delta r_0(t,x)|\boldsymbol{\delta r}(t,x)) = \sum_{i=1}^{m} p(\delta r_0(t,x)|\boldsymbol{\delta r}(t,x), \boldsymbol{\vartheta}_i, \kappa_i)w(\boldsymbol{\vartheta}_i, \kappa_i) \tag{4.6}$$

where

$$w(\boldsymbol{\vartheta}_i, \kappa_i) = \frac{p(\boldsymbol{\delta r}(t)|\boldsymbol{\vartheta_i}, \kappa_i)}{\sum_{j=1}^{m}\boldsymbol{\delta r}(t)|\boldsymbol{\vartheta_j}, \kappa_j)}$$

Please refer to [66] for results on the consistency of the posterior predictive density estimator in Equation (4.6). As suggested in [53], we use the median of the predictive density function as the predictor of $\delta r(t,x)$ and not the mean. This is because the mean may not be defined for all transformations, e.g., the posterior density $p(\delta r_0(t,x)|\boldsymbol{\delta r}(t,x), \boldsymbol{\vartheta}_i, \kappa_i)$ of a class of Box-Cox family of transformation is $\log t$ for which mean does not exist.

4.2.3 Copula for joint probability estimation

As noted in the foregoing, $r(t,x)$ is a $g_\kappa-$Gaussian random field, i.e.,

$$g_\kappa(\delta r(t,x)) = m(x)\boldsymbol{\beta} + e(x), e(x) \sim \mathcal{N}(0,\Sigma)$$

Here, the marginal distribution of the random field is characterized by the $g_\kappa-$Gaussian random field. Although the joint distribution of the random variables in the Gaussian random field is jointly Gaussian, the $g_\kappa(.)-$transformation could significantly change the covariance structure and likely to induce asymmetry ([22, 53]). In such situations, copula-based approaches allow us to model the joint distribution of random variables $\delta r(t,x_i), i = 1,2,\ldots,n$ by separately modeling the dependence structure and the marginals.

Copulas arise in a variety of scenarios when modeling the joint distribution of random variables ([107]) and offer a simple, yet powerful approach to sample from the joint distribution of random variables with known marginals. Specifically, a copula function $C = C(u_1,u_2,\ldots,u_n)$ is a multivariate distribution defined on a unit hypercube with uniform marginals, i.e.,

$$C(u_1,u_2,\ldots,u_n) = P(U_1 \leq u_1,\ldots,U_n \leq u_n) \tag{4.7}$$

where $U_i \sim$ uniform$(0,1), i = 1,2,\ldots,n$. Given a vector of random variables denoted by $\mathbf{Z} = \{Z_1,Z_2,\ldots,Z_n\}$ with joint distribution function $F(z_1,z_2,\ldots,z_n) = P(Z_1 \leq z_1, Z_2 \leq z_2,\ldots,Z_n \leq z_n)$, then from the Sklar's theorem [134], the copula associated with F is unique and satisfies

$$F(z_1,z_2,\ldots,z_n) = C(F_1(z_1),\ldots,F_n(z_n)) \tag{4.8}$$

where $F_i, i = 1,2,\ldots,n$ are continuous marginal distributions. What we have realized here is an n-dimensional copula that expresses the joint distribution of a multivariate distribution in terms of its marginals only.

Over the years, several copula functions have been proposed depending on the dependence structure and the methods of constructing copulas, e.g., Archimedean copula for modeling dependence in arbitrarily high dimensions ([83]). Generally, the copula function is modeled parametrically with some recent works focusing on nonparametric modeling. In this work, we restrict to bivariate parametric copulas and use an exact maximum likelihood (EML) estimation approach to estimate the parameters of the copula model. Let X and Y denote two continuous random variables with marginal density $f(x)$ and $g(y)$, respectively and $\boldsymbol{\theta} = [\psi, \gamma, \eta]$ denote the unknown parameter vector where $\psi \in \Psi$ denotes the parameter(s) of $f(x)$, $\gamma \in \Gamma$ denotes the parameter(s) of $g(x)$, and $\eta \in H$ denotes the parameter(s) of the copula $C(F(x), G(x))$. Using copula decomposition of a joint distribution function, i.e.,

$$h(x, y|\boldsymbol{\theta}) = f(x|\psi) \cdot g(y|\gamma) \cdot c(F(x|\psi), G(y|\gamma)|\eta) \tag{4.9}$$

the corresponding log-likelihood function is given as,

$$\mathcal{L}_{XY} = \sum_{i=1}^{N} \log f(x_i|\psi) + \sum_{i=1}^{N} \log g(y_i|\gamma) + \sum_{i=1}^{N} \log c(F(x_i|\psi), G(y_i|\gamma)|\delta) \tag{4.10}$$

such that $\hat{\boldsymbol{\theta}}$ is obtained by maximizing the log-likelihood function $\mathcal{L}_{XY}$. Subsequently, we employ the Akaike Information Criterion (AIC) to select the best copula model. With the best copula model at hand, we can draw samples from the joint distribution function and estimate the probability of bridging as shown in Equation (5.2).

4.3 Quantification of surface morphology

In the foregoing sections, we looked at an approach for constructing planar graphs from images. We now discuss an approach for quantifying the graph configuration and therefore make inference on endpoint detection.

Spectra of planar graphs defined based on the eigenvalues and eigenvectors of $E(t)$ and functions thereof, exhibit interesting properties that reveal certain important graph characteristics ([105]). Among these, the second smallest eigenvalue (λ_2) of the normalized Laplacian $\mathcal{L}$ also known as Fiedler value has been extensively studied in the context of graph-based image segmentation and partitioning problems ([132]) where the eigenvector associated with λ_2 allows for efficient graph partitioning. Formally, the normalized Laplacian $\mathcal{L}$ of the graph G is given as, $\mathcal{L} = \mathcal{D}^{-1/2} \times L \times \mathcal{D}^{1/2}$ where L is the combinatorial Laplacian defined as $L = \mathcal{D} - E$ where $\mathcal{D}$ is the diagonal matrix representing the degree of each node and is given as,

$$\mathcal{D} = \begin{bmatrix} \sum_{j=1}^{n} e_{1j} & \sum_{j=1}^{n} e_{2j} & \dots & \sum_{j=1}^{n} e_{nj} \end{bmatrix} \tag{4.11}$$

Returning to the polishing process, we note that every particle j could only bridge with only a limited number of particles that lie in its immediate neighborhood $(N_j(t))$. At any polishing stage, λ_2 quantifies how easily the graph could be partitioned into two disjoint sets. As polishing progresses, more and more particles bridge, making it difficult to find such a partition, and therefore, λ_2 increases. The values of λ_2, therefore, serve as a natural quantifier to capture the evolution in the neighborhood structure and consequently the effects of polishing on the surface morphology. For example, $\lambda_2 = 0$ indicates the complete absence of bridge formation; in contrast, larger values suggests a higher degree of bridging where every node is connected to a certain number of other neighboring nodes. However, there is a finite upper bound on the value of λ_2 and is achieved when no more bridging between the particles can occur. This is when the endpoint of the polishing process is achieved. What remains now to establish is how much can the λ_2 value increase during the polishing process.

As noted in the foregoing, each of the particles during the polishing process can bridge only with a limited number of particles depending upon the packing density. For a surface morphology as shown in Figure 4.5(a), it is pragmatic to assume a random loose packing structure with packing density ϕ_{rlp}. Using ϕ_{rlp}, we study the relationship of the Fiedler value with the corresponding connectivity structure as described in the foregoing. We first present the following important result on the embedding of a planar graph in a Euclidean space and its relation with the Fiedler value ([135]).

Lemma 1. *Let $G = (V, E)$ be a planar graph. Then λ_2 of the Laplacian is given by*

$$\lambda_2 = \min_{v_i \in R^N} \frac{\sum_{i,j \in E} ||\vec{v}_i - \vec{v}_j||^2}{\sum_{k=1}^{N} ||\vec{v}_k||^2} \tag{4.12}$$

where $\{\vec{v}_1, \vec{v}_2, \ldots, \vec{v}_n\}$ are the eigenvectors of the Laplacian such that $\sum_{i=1}^{N} \vec{v}_i = \vec{0}$

Proof of the result can be found in [135]. The lemma relates the embedding of a graph in the Euclidean plane with its Fiedler value. The next lemma discusses an approach to embed the graph on a plane by using kissing disks–disks that intersects only at the boundary.

Lemma 2. *Let $G = (V, E)$ be a planar graph with N nodes. Then, there exists a set of disks, say $\{D_1, D_2, \ldots, D_N\}$, in the plane with disjoint interiors such that D_i and D_j touch if and only if $(i, j) \in E$.*

Such an embedding is also known as kissing disk embedding and was proposed by Koebe, Andreev, and Thurston individually [12]. With this geometric embedding and with an appropriate stereographic projection of disks on a unit sphere (see [135]), we first present an existing result on the upper bound on λ_2.

Theorem 1. *Let $G = (V, E)$ be a planar graph with N nodes of degree at most Δ. The Fiedler value of G is at most $8\Delta/N$.*

The theorem provides an upper bound on the connectivity of individual nodes, i.e, Δ for a given value of λ_2. The result uses the geometric embedding proposed by Koebe, Andreev, and Thurston ([12]) followed by a stereographic projection of disks on a sphere. The embedding, however, emphasizes only on maintaining tangency and not the packing density ([50]). This suggests that as the packing density of disks (in the present case, metallic spheres) decreases, the bound becomes loose. In fact, packing with low density is often encountered when spherical particles are dispersed loosely as in during the sintering process in AM. This motivates the need for a lower bound to accurately quantify the process of bridging during polishing. Using the random loose packing density ϕ_{rlp}, we obtain the following result.

Theorem 2. *Let $G = (V, E)$ be a planar graph with N nodes of degree at least δ. The Fiedler value of G is at least $8\phi_{rlp}\delta/N$.*

Proof. From Theorem 4 and Lemma 3, there exists a stereographic projection of G on a unit sphere using kissing caps–analogous to kissing disks–each with radii r_i. Note that a cap is essentially the intersection of the half space with the sphere. If cap i and cap j belong to the kissing set, then $||\vec{v}_i - \vec{v}_j||^2 \leq (r_i + r_j)^2 \leq 2(r_i + r_j)^2$ and therefore,

$$\sum_{i,j \in E} ||\vec{v}_i - \vec{v}_j||^2 \leq 2\Delta \sum_{i=1}^{N} r_i^2 \tag{4.13}$$

Assuming that the caps do not intersect due to planarity of G and sphere preserving stereographic projection,

$$\sum_{i=1}^{N} r_i^2 \leq \frac{1}{\pi}[4\pi(1)^2] \tag{4.14}$$

Using Lemma 2, Equations (4.13), and (4.14), we have

$$\sum_{i,j \in E} ||\vec{v}_i - \vec{v}_j||^2 \leq 2\Delta \sum_{i=1}^{N} r_i^2 \leq \frac{2\Delta}{\pi}[4\pi(1)^2]$$

$$\implies \lambda_2 \leq \frac{8\Delta}{N}$$

Assuming that the particle distribution follows a random loose packing structure with packing density ϕ_{rlp}, we have,

$$\sum_{i=1}^{N} r_i^2 \geq \phi_{rlp}\frac{1}{\pi}[4\pi(1)^2] \implies 2\delta \sum_{i=1}^{N} r_i^2 = \phi_{rlp}\frac{2\delta}{\pi}[4\pi(1)^2]$$

$$\implies \frac{\sum_{i,j \in E} ||\vec{v}_i - \vec{v}_j||^2}{\sum_{k=1}^{N} ||\vec{v}_k||^2} \geq \phi_{rlp}\frac{8\delta}{N}$$

□

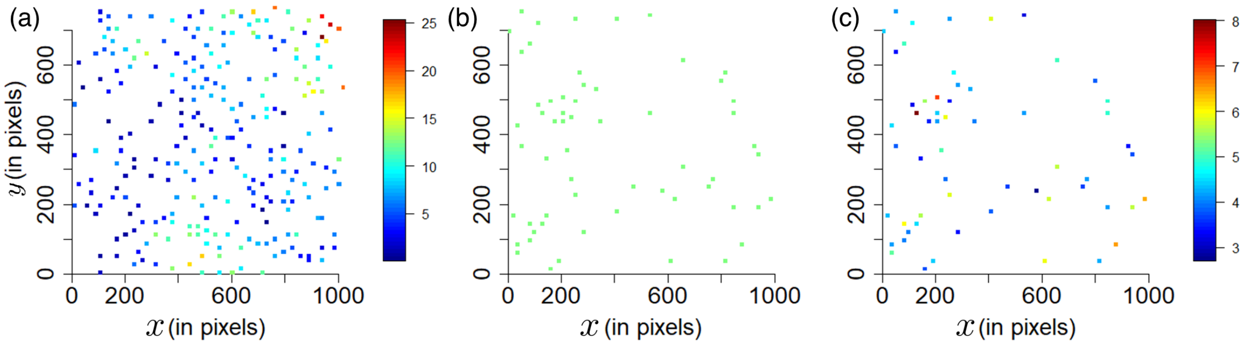

Figure 4.3: (a) Particle locations for which the increase in radius is known (b) unknown locations for prediction (c) prediction of the increase in particle radius as obtained using BTG.

Combining the above two results, we have,

$$\phi_{rlp}\frac{8\delta}{N} < \lambda_2 \leq \frac{8\Delta}{N} \tag{4.15}$$

As bridging between the neighboring particles increases during polishing, the value of λ_2 increases and is expected to stay within the bound specified in Equation (4.15). In addition to this, we note from Theorem 4 that $\Delta \geq N\lambda_2/8$. Given λ_2, this inequality allows us to lower bound the value of Δ, i.e., the maximum node density and will be employed in the next section for endpoint detection.

4.4 Results

A representative sequence of images collected during various stages of the polishing process is shown in the top row of Figure 4.5. The surface was imaged at five different timestamps, 0, 180, 270, 360, and 450 seconds during the polishing process. As time progresses, bridging between particles results in local smoothening of the surface. These locations have a darker gray pixel value. In contrast, light regions indicate unpolished areas or depressions.

To obtain the graph representation of these images, we first employ the BTG model to estimate the increase in particle radius followed by the probability of bridging (i.e., $e_{ij(t)}$)

using the copula model. Figure 4.3(a) shows a representative example indicating the locations where $\delta_r(t,x)$ is known. Unknown locations are marked in Figure 4.3(b). Prediction results obtained from the BTG model at the unknown locations are shown in Figure 4.3(c). With the estimates of $\delta r(t,x_i)$ available, we now invoke our copula model to determine the joint distribution function of the $\delta r(t,x_i)$ and $\delta r(t,x_j)$ for some $x_i, x_j \in \mathcal{P}(\mu)$ over the random field $\delta r(t,x)$.

In this regard, we determine the best fitting copula. We investigated 40 different families of copula as provided by the VineCopula package in R ([129]) and employ the EML approach to estimate the parameters of the copula model. Among different copulas, we note that three different copulas were selected across all the polishing stages using AIC, namely Frank copula, student t-copula, and BB8 copula. Except for the Frank copula which is a bivariate single parameter copula, both student t-copula and BB8 copula are bivariate two-parameter copulas. However, BB8 copula remains consistently either the best choice or has only slightly higher AIC value as compared to the AIC values of Frank or student t-copula. To avoid working with three different copulas, we only consider the BB8 copula. The functional form of the BB8 copula is given as,

$$C(u,v|\theta,\eta) = \frac{1}{\eta}\left(1 - \left(1 - \frac{h(\eta u)h(\eta v)}{h(\eta)}\right)^{1/\theta}\right) \tag{4.16}$$

where $h(t) = 1-(1-t)^\theta$ and $\theta \geq 1$, $0 \leq \eta \leq 1$.

The simulated BB8 copula for a representative stage is shown in Figure 4.4 with parameter values $\theta = 5.06$ and $\eta = 0.48$. We use a conditional distribution method to sample from the copula described as follows. Let $C_u(v)$ be the conditional distribution function of V given $U = u$ as,

$$C_u(v) = P(V \leq v|U = u) = \lim_{\Delta u \to 0} \frac{C(u+\Delta u, v) - C(u,v)}{\Delta u} = \frac{\partial C(u,v)}{\partial u} \tag{4.17}$$

We now use the following steps to sample from the copula $C(u,v)$,

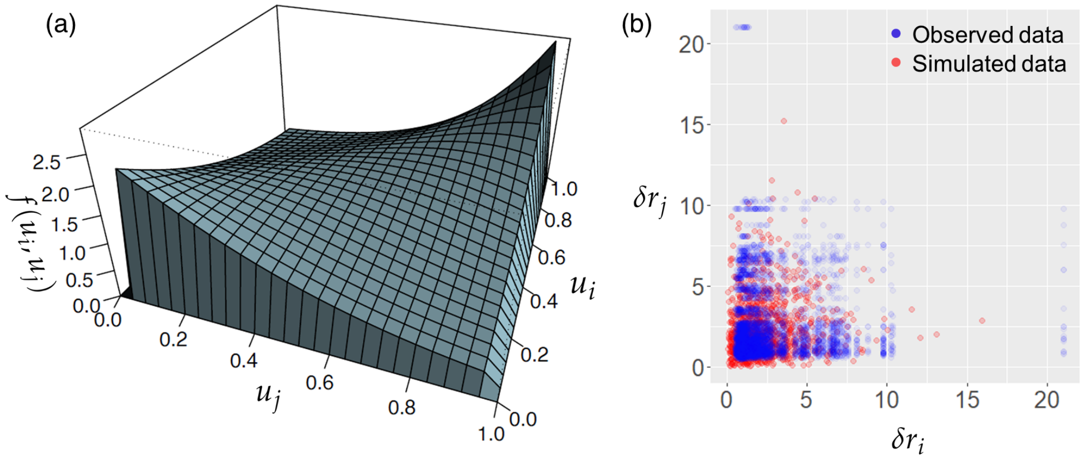

Figure 4.4: (a) Density function of the copula (b) observed and simulated data.

1. Generate two independently distributed uniform $(0, 1)$ random numbers u and ζ.
2. Set $v = C_u^{\leftarrow}(\zeta)$, where $C_u^{\leftarrow}(\zeta)$ is the quasi-inverse of $C_u(v)$
3. The pair (u, v) is now a sample from the copula $C(u, v)$

From the density plot of the BB8 copula, we note that there is some degree of tail dependence. This might emerge from the dynamics of the polishing process itself. During polishing, if a particle is undergoing very little material redistribution (i.e., δr_j is small), then it is highly likely that particles in its neighborhood would also have very little material redistribution. Similarly, if a particle is undergoing high material redistribution, its neighboring particles would also exhibit high material redistribution.

We now return to our planar graph construction using Equation (5.1). Given the estimates of the increase in the inter-particle radius as well as the joint distribution functions of $\delta r(t, x_i), \delta r(t, x_j)$, we estimate the probability $e_{ij}(t)$ as stated in Equation (5.1). A representative network configuration obtained using the $e_{ij}(t)$ is shown in the bottom row of Figure 4.5. As polishing ensues, the neighboring particles progressively bridge, resulting in the formation of a smooth interconnected land of flat particles. This implies that the values of the network edges $e_{ij}(t)$ gradually increase, thereby increasing the connectivity among the nodes of the network. We now utilize the graph characteristics to quantify the evolution in

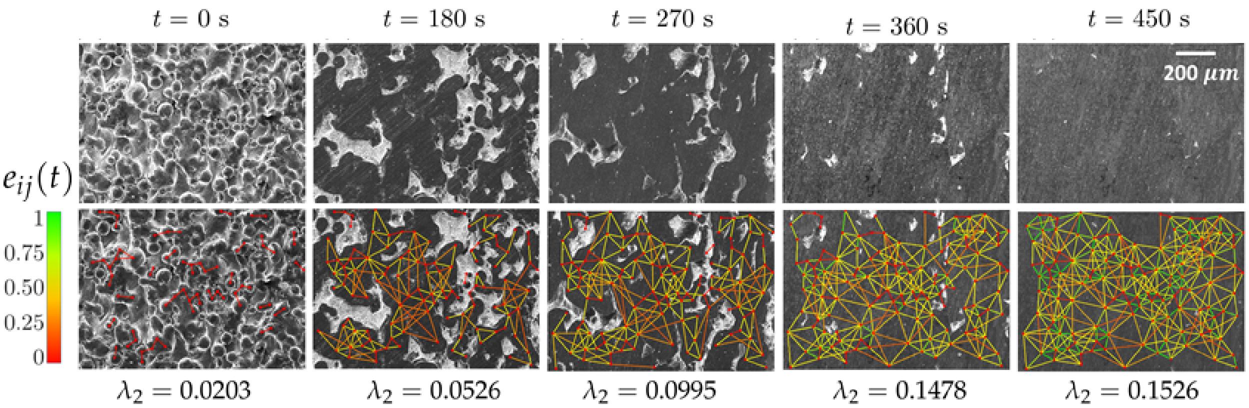

Figure 4.5: SEM images (top) and corresponding network representation (bottom) showing the surface morphology during polishing.

surface morphology and develop strategies for endpoint detection.

The surface morphology pattern as well as the corresponding λ_2 values presented in Figure 4.5 suggest that as finishing ensues and the particle diameters grow, the propensity of neighboring particles to bridge (i.e., $e_{ij}(t)$) progressively increases. Quantitatively speaking, the initial value of $\lambda_2 \approx 0.02$ indicates little bridging (average number of bridges connecting a node is < 1) as reflected in $e_{ij}(t)$ being close to zero between almost all particles. Specifically, the edges connecting the neighboring nodes are almost absent initially, and low probability edges (red) connect only a sparse set of neighboring nodes. After 450 s of finishing, λ_2 increases to approximately 0.15, suggesting a higher degree of bridging among all neighboring particles, and high $e_{ij}(t)$ values. Figure 4.6 shows the value of λ_2 along with its theoretical upper and lower bounds at different stages of the polishing process. The packing density ϕ_{rlp} for estimating the bounds in this case study is estimated from the undeformed configuration of particles as shown in Figure 4.5 ($t = 0$ s) for which is $\phi_{rlp} \approx 0.40$. Note that in the final stages of polishing, the value of λ_2 stabilizes. More specifically, $\lambda_2^{450\text{ s}} \approx 0.15$ suggest that the maximum node degree in the final stage of polishing is at least five (using the inequality $\Delta \geq N\lambda_2/8$). This suggests that when polishing is done, each of the particles is expected to be bridged by five or more particles. This is in accordance with the general understanding

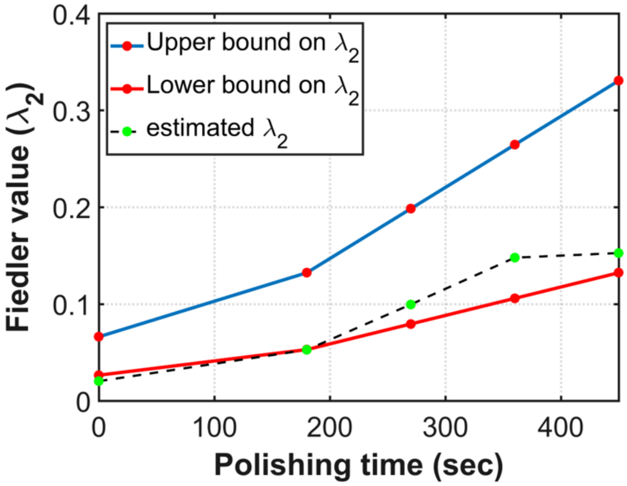

Figure 4.6: Variation of λ_2 values estimated from the micrographs and its comparison to the theoretical upper and lower bounds.

of connectivity structure of metal spheres within a random loose packing structure.

4.4.1 Effect of graph size on the inferred node degree

When dealing with graphs and especially the connectivity structure of the nodes, it is important to consider the impact of boundary nodes. Because of the planarity constraint, the connectivity of boundary nodes may be significantly different from the rest of the nodes. To address this, we take a look at the variation in the Fiedler value for different number of nodes. Since the particles have minimum overlap, increasing the number of nodes means increasing the area of scan. We consider four different cases with 32, 166, 255, and 327 (randomly generated) nodes. For each of the cases, we use Equation (4.15) to estimate the value of Δ

Table 4.1: Effect of the number of nodes on Δ

# of nodes	Stage 1	Stage 2	Stage 3	Stage 4	Stage 5
32	0.015	0.177	0.8028	2.130	5.776
166	0.047	0.229	0.9341	2.719	7.148
255	0.096	0.128	0.1548	2.069	5.231
327	0.390	0.297	0.804	2.157	5.763

and is summarized in Table 5.1. We note that the value of Δ is greater than 5 in all the cases considered. This suggests that the inference presented in the previous subsection, i.e., each of the particle is connected to at least five other particles in its neighborhood, holds irrespective of the size of the graph or the number of nodes considered.

4.4.2 Comparison with traditional surface quantifiers

Conventional quantifiers, such as average surface roughness (S_a) do not capture the evolution of micropores and voids, especially towards the end stages of polishing. Here the S_a values showed an almost negligible change of 0.37%, versus 63.8% change in λ_2 value in the last 90 seconds of the polishing process. From an endpoint detection standpoint, this means that S_a values would not be representative of the polishing process, i.e., it might not capture the surface quality improvements. In contrast, the λ_2 value is sensitive to the neighborhood structure i.e., the distance of neighboring particles (presence of porosity would result in a non-zero distance) and consequently, the λ_2 value would increase as long as the surface roughness and porosity reduce.

4.4.3 Sensitivity analysis

As seen in the foregoing our approach is based on tracking the physical transformations in particles. For a nanoparticle clustering problem, this may be individual nanoparticles. In such a scenario, the inferences gathered from the graph construction may depend on the number of particles identified in any image. Therefore, we test the sensitivity of the Fiedler value when only a subset of the particles could be recorded by the image processing algorithm, and therefore, comment on the robustness of our representation.

The nodes in the planar graph represent particles and removing a set of nodes would create a physical depression on the surface, thereby leaving the surface only partially polished. As a result, we only focus on removing a very limited number of particles that may be missed by the image processing algorithm. We consider 5 different cases with less than 10% nodes. For each case, we randomly remove $x\%, x \leq 10$ nodes and calculate the Fiedler

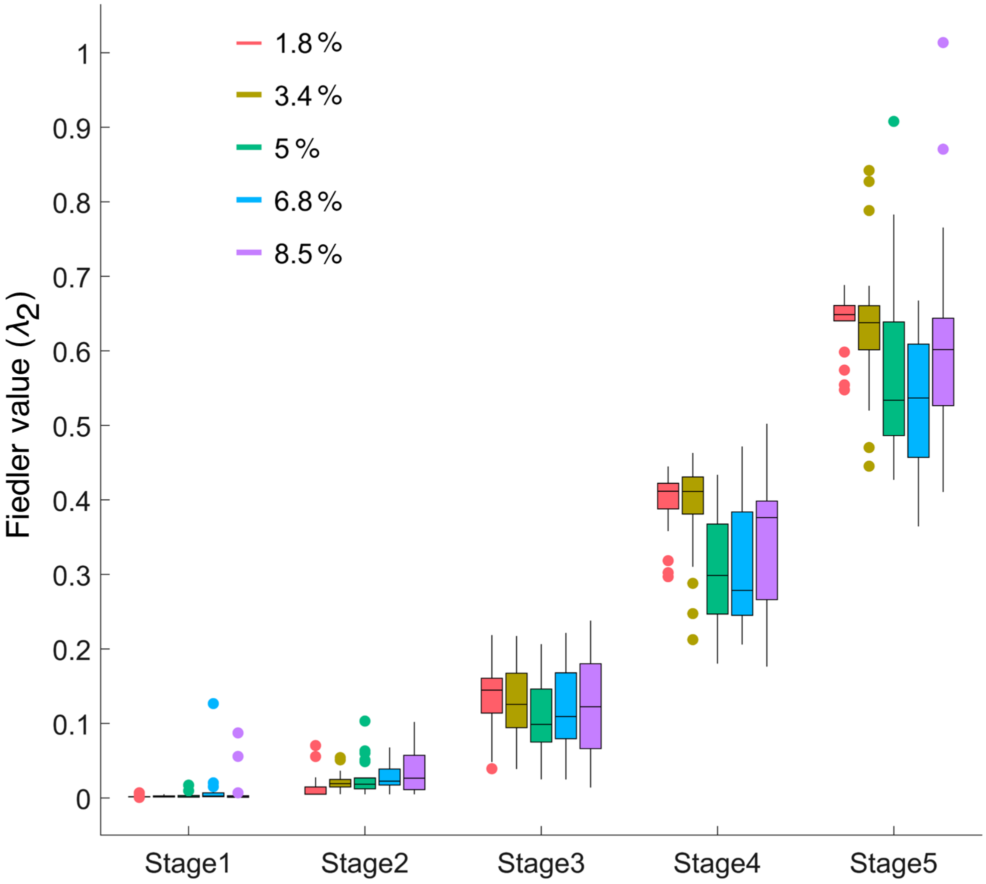

Figure 4.7: Box-plot of the Fiedler value estimated at 20 different locations across all the five polishing stages.

value for all the subsequent stages. For every case, we performed 30 replications to ensure a stable estimate of the Fiedler value. The results are summarized in Figure 4.7. At each of the five stages, we consider different cases of the percent of nodes removed in the order of 1.8%, 3.4%, 5%, 6.8%, and 8.5%. In initial stages, the surface is mostly rough and still consists of physically visible particles. From a graph standpoint, this means that there several disconnected nodes. Removing a few nodes, therefore, has very little impact on the Fiedler value. To check if all the five cases have equal means, we test the following hypothesis:

$$H_0 \quad : \quad \overline{\lambda}_{2(1)} = \overline{\lambda}_{2(2)} = \ldots = \overline{\lambda}_{2(5)}$$

$$H_1 \quad : \quad \overline{\lambda}_{2(i)} \neq \overline{\lambda}_{2(j)} \text{ for at least one } i \text{ and } j$$

where $\overline{\lambda}_{2(i)}$ denotes the Fiedler value in case i. Using ANOVA, we note that for stages 1, 2, and 3, the p-value is equal to 0.177, 0.146, and 0.691 suggesting strong evidence in the favor of the null hypothesis. However, as the surface gets into the final stages, i.e., 4 and 5, we note the p-value is significantly smaller than 0.0001, indicating that the group means are not the same. Since removing nodes essentially means removing particles from the surface, this leaves physical depressions (or voids) on the surface rendering the surface unpolished. Moreover, we note that the group mean decreases as more nodes are removed, indicating the removing nodes render the graph "weakly" connected, i.e., unpolished.

Two important inferences can be drawn from the sensitivity analysis:

1. The representation is robust as long as the error in detecting the particles is within 5%. Since the degree of overlap between the particles is minimal, any reasonably efficient algorithm would detect the particles with less than 5% error ([113]).
2. The sensitivity of the representation increases after more than 5% of the particles are removed, i.e., we note a significant drop in the Fiedler value. In comparison, methods based on average estimates such as average surface roughness tend to be insensitive to voids and depressions. This was also reported in some of the earlier studies e.g., [120]. This sensitivity of the Fiedler value demonstrates that it is able to capture the presence of voids or depressions on the surface, indicating the need for further polishing.

4.5 Summary and conclusions

We present a physics-based random planar graph representation of the surface morphological evolution during the polishing process. Phenomenologically, surface morphologies are realizations from a random field defined over the particles that gradually expand (in diameter) until they make physical connections (i.e., bridge) with the neighboring particles. We capture this process in the form of an evolving planar graph where particles represent the nodes, and the probability of particles to bridge serves as the edge weight. To specify the graph configuration, we employ a BTG model to predict the increase in the radius of the particles followed by a copula model to estimate the probability of particles to bridge. Via theoretical bounds on λ_2, we infer that during endpoint stages, each of the particle bridges with at least five neighboring particles. We also present the sensitivity analysis of the Fiedler value. Results show that Fiedler value is not sensitive if the number of missing particles is less than 5% of the total number of particles present.

5. CONSISTENT ESTIMATION OF THE MAX-FLOW PROBLEM: TOWARDS UNSUPERVISED IMAGE SEGMENTATION

Advances in the image-based diagnostics of complex biological and manufacturing processes have brought unsupervised image segmentation to the forefront of enabling automated, on the fly decision making. However, most existing unsupervised segmentation approaches are either computationally complex or require manual parameter selection (e.g., flow capacities in max-flow/min-cut segmentation). In this work, we present a fully unsupervised segmentation approach using a continuous max-flow formulation over the image domain while optimally estimating the flow parameters from the image characteristics. More specifically, we show that the maximum *a posteriori* estimate of the image labels can be formulated as a continuous max-flow problem given the flow capacities are known. The flow capacities are then iteratively obtained by employing a novel Markov random field prior over the image domain. We present theoretical results to establish the posterior consistency of the flow capacities. We compare the performance of our approach on two real-world case studies including brain tumor image segmentation and defect identification in additively manufactured components using electron microscopic images. Comparative results with several state-of-the-art supervised as well as unsupervised methods suggest that the present method performs statistically similar to the supervised methods, but results in more than 90% improvement in the Dice score when compared to the state-of-the-art unsupervised methods.

5.1 Introduction

The objective of image segmentation is to partition an image into semantically interpretable and spatially coherent entities featuring similar characteristics, e.g., pixel intensities and texture. Although, the history of image segmentation can be dated back to almost half a century ago, recent advances in the image-based diagnostics of complex biological processe, materials characterization, object tracking, etc. have brought image segmentation to the forefront of enabling automated, on the fly decision making.

A vast majority of the current image segmentation approaches are supervised, i.e., they employ models that learn from previously labeled images to determine the partitions and/or the ROIs in a given image. Their performance relies on the availability of a large collection of labeled images, and at times, the expert knowledge [87]. With the growing database of images from newer imaging technologies coupled with the increasing emphasis on on the fly detection of novel (i.e., previously unseen) ROIs, and the sheer enormity of the efforts needed to create a large pool of labels and atlases underscore the need for unsupervised segmentation methods. To illustrate this need, let us consider the problem of tumor detection from magnetic resonance (MR) images. On average each event detection involves the investigation of hundreds of slices that may vary significantly from patient to patient as well as over time. In such cases, retraining becomes inevitable, especially when novelty cases are encountered [99]. The spatial and temporal uncertainty in the morphology and location of ROIs further complicate these challenges. In addition, many a time data collection itself is extremely costly, e.g., imaging microscopic defects and microstructure anomalies in additively manufactured (AM) industrial components tend to be time intensive. Together with cost and resource constraints, it becomes infeasible to gather big datasets for any given material system and processing recipe [112].

Surprisingly, the literature on unsupervised segmentation is somewhat limited. The most notable methods include normalized cuts that is based on spectral graph partitioning [132] and its subsequent derivatives such as watershed-based normalized cut [158] and multiscale normalized cut [51], mean shift clustering using the neighborhood pixel information [49], k-means clustering, expectation maximization and Markov random field-based methods [165]. However, significant limitations exist, especially for the case of purely unsupervised approaches in terms of computational complexity, e.g., exact minimization of normalized cut is NP-complete [132], mean shift clustering requires manual specification of the kernel function and bandwidth [106].

Image segmentation approaches based on the energy minimization framework, particularly graph-based methods offer an elegant means to segment images without extensive training. Essentially, they involve minimizing an energy functional of the form [65] $E = E_{data} + E_{smooth}$ where E_{data} accounts for the disagreement between the data samples, i.e., observed pixels and the estimated labels, and E_{smooth} controls the smoothness of the labeling function. Continuous max-flow/min-cut algorithm is an efficient optimization approach to minimize the energy functions in polynomial time [88]. However, the problem of selecting the flow capacities prevents a fully unsupervised implementation. Most of the existing implementations of the continuous max-flow are either based on *a priori* selection of the flow capacities [13] or require manual interventions [162].

In this work, we present an approach to consistently estimating the flow capacities of a continuous max-flow/min-cut problem leading to fully unsupervised, fast image segmentation. Our framework is based on iteratively estimating the image labels by solving the max-flow problem while optimally estimating the flow capacities from the image characteristics. More specifically, we first setup the segmentation problem as a maximum *a posteriori* estimation (MAP) of the image labels and show that it is equivalent to solving the max-flow problem given the flow capacities are known. By using the current optimum of the max-flow problem, we subsequently estimate the flow capacities by employing a novel Markov random field (MRF) prior over the flow capacities. In the sequel, we present theoretical results to establish the posterior consistency of the flow capacities based on the MRF prior proposed in this work. We implement our methodology on benchmark tumor datasets and a case study on the segmentation of defects in AM components that are fabricated using different processing recipes. An extensive comparison with state-of-the-art unsupervised algorithms suggests more than 90% improvement in the average Dice score—a measure of the degree of overlap between the estimated labels and the ground truth (see Equation (5.16)).

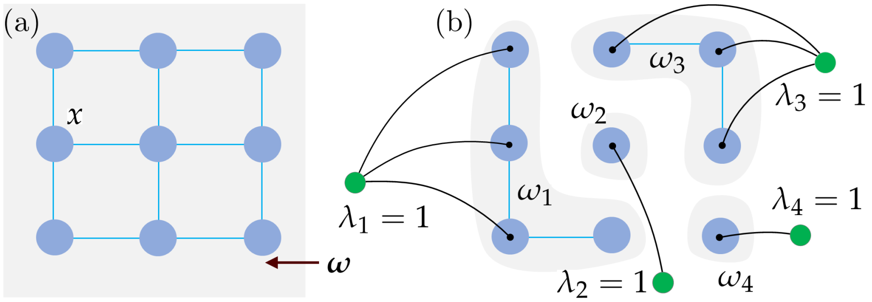

Figure 5.1: (a) Graph representation of an image $\boldsymbol{\omega}$ in a continuous domain. (b) A representative example of segmentation of the image $\boldsymbol{\omega}$ into subdomains $\omega_1, \ldots, \omega_k$ via graph cut.

5.2 Image segmentation via graph cuts

In this section, we begin with the basic notion of graph cuts. Let $\boldsymbol{\omega}$ be a continuous image domain (e.g., see Figure 5.1(a)) and x be the sites (or pixels) in $\boldsymbol{\omega}$. The problem of image segmentation can be formulated as partitioning $\boldsymbol{\omega}$ into n disjoint subdomains $\omega_1, \omega_2, \ldots, \omega_n$, with corresponding labeling function given as,

$$\lambda_i(x) = \begin{cases} 1 & x \in \omega_i \\ 0 & x \notin \omega_i \end{cases} \tag{5.1}$$

The partitioning is performed such that the resulting subdomains minimize the following energy functional [45],

$$\min_{\lambda_i(x) \in \{0,1\}} \sum_{i=1}^{n} \int_{\boldsymbol{\omega}} \{\lambda_i(x)\rho(x, \lambda_i(x)) + C(x)|\nabla \lambda_i(x)|\} dx \tag{5.2}$$

where the first term $\rho(x, \lambda_i(x))$ is the cost of assigning the site x to the subdomain ω_i and is equivalent to the E_{data} term when summed over the domain $\boldsymbol{\omega}$. The second term is the total variation (TV) regularization of $\lambda_i(x), \forall i \in \{1, 2, \ldots, n\}$ where $C(x) > 0$ controls the trade-off between the data term and the extent of regularization. TV regularization is particularly useful because of its property to selectively penalize the oscillations due to noise while preserving the discontinuities at the edges (see [137] for a mathematical justification).

Note that the minimization function in Equation (5.2) is non-convex due to the binary configuration of $\lambda_i(x)$. To ensure tractability of the energy minimization function in Equation (5.2), we consider the convex relaxation of $\lambda_i(x) = \{0, 1\}$ to the unit interval $[0, 1]$ as proposed by Chan et al. [45]. For simplification, we only consider the case of binary segmentation such that $n = 2$, $\lambda(x) = 1 - \lambda_1(x) = \lambda_2(x)$ (since $\sum_{i=1}^{n} \lambda_i(x) = 1$), $C_s(x) = \rho(x, \lambda_1(x))$ and $C_t(x) = \rho(x, \lambda_2(x))$. Consequently, the energy minimization function for the case of binary label configuration can be written as,

$$\min_{\lambda(x)\in[0,1]} \int_{\omega} (1 - \lambda(x))C_s(x) + \lambda(x)C_t(x) + C(x)|\nabla\lambda(x)|dx \tag{5.3}$$

Authors in [45] deduced that the optimal solution to Equation (5.2) can be obtained by thresholding the solution of the resulting convex problem in Equation (5.3). However, the numerical algorithms for this minimization problem still suffer from the non-differentiability of the TV term ($\int_{\boldsymbol{\omega}} |\nabla\lambda(x)|dx$) [149]. To overcome this, we investigate the dual of the energy function in Equation (5.3) and show that it is analogous to the continuous max-flow problem studied in [161, 20].

5.3 Continuous max-flow formulation

In this section, we derive the dual of the energy function reported in Equation (5.3) and subsequently show that the dual is a max-flow problem in a continuous domain. We first consider the following results.

Lemma 3. *Given* $\lambda(x)$ *is an indicator function as given in Equation* (5.1)*, it has bounded variation in* $\boldsymbol{\omega}$*, i.e., there exists a function* $p(x) \in \mathcal{C}^1(\boldsymbol{\omega})$ *with compact support and* $|p(x)| \leq 1$ *satisfying* $\sup\{\int_{\boldsymbol{\omega}} \lambda(x)\mathrm{div}p(x)dx\} < \infty$ *such that,*

$$\int_{\boldsymbol{\omega}} \lambda(x)\mathrm{div}p(x)dx = -\int_{\boldsymbol{\omega}} p(x) \cdot \nabla\lambda(x)dx$$

Lemma 4. *With $p(x)$ defined as in Lemma 1, we have,*

$$\int_{\boldsymbol{\omega}} C(x)|\nabla\lambda(x)|dx = \max_{|p(x)|\leq C(x)} \int_{\boldsymbol{\omega}} \lambda(x)\text{div}p(x)dx$$

Next, we consider functions $p_s(x) \leq C_s(x), p_t(x) \leq C_t(x) \in \mathbb{R}$ such that we get the following min-max equivalent of Equation (5.3),

$$\min_{\lambda(x)\in[0,1]} \max_{\substack{p_s(x)\leq C_s(x)\\ p_t(x)\leq C_t(x)\\ |p(x)|\leq C(x)}} \int_{\boldsymbol{\omega}} (1-\lambda(x))p_s(x) + \lambda(x)p_t(x) + \lambda(x)\text{div}(p(x))dx$$

Note that the above min-max function is convex for fixed $\lambda(x)$ and concave for fixed $p_s(x), p_t(x)$, and $p(x)$ [163]. Via minimax theorem [32], we obtain the dual of Equation (5.3) as,

$$\begin{aligned} &\max \int_{\boldsymbol{\omega}} p_s(x)dx \qquad (5.4)\\ \text{subject to } \; &p_s(x) \leq C_s(x),\; p_t(x) \leq C_t(x),\; |p(x)| \leq C(x)\\ &\text{div}p(x) - p_s(x) + p_t(x) = 0 \;\; \forall x \in \boldsymbol{\omega} \end{aligned}$$

The resulting formulation is the continuous analog of the discrete max-flow problem, i.e., maximizing the total source flow $p_s(x)$ subject to the source, sink and spatial flow capacities while satisfying the flow conservation principle.

To elaborate on the continuous max-flow problem, we begin by connecting each site x to a source s and a sink t of infinite capacities. Each site in $\boldsymbol{\omega}$ is then associated with three different flow fields: the source flow $p_s(x) \in \mathbb{R}$, the sink flow $p_t(x) \in \mathbb{R}$, and the spatial flows $p(x) \in \mathbb{R}^2$. Here, the source and the sink flow fields are directed from the source s to the site $x \in \boldsymbol{\omega}$ and from the site x to the sink t, respectively. This is shown schematically in Figure 5.2. The spatial flow field is characterized by the undirected flow through x, thereby capturing the strength of interaction with the neighborhood locations. Each of the source, sink and spatial flows are constrained by their respective capacities represented as $C_s(x), C_t(x)$ and $C(x)$.

Returning to Equation (5.4), we determine the maximum flow by writing the corresponding augmented Lagrangian as,

$$\mathcal{L}(p_s, p_t, p, \lambda(x)) = \int_{\omega} p_s(x) + \lambda(x)(\text{div}(p(x)) - p_s(x) + p_t(x))dx - \frac{c}{2}||\text{div}(p(x)) - p_s(x) + p_t(x)||^2 \tag{5.5}$$

where $c > 0$. See [161] for solving the augmented Lagrangian $\mathcal{L}(p_s, p_t, p, \lambda(x))$ using the projection gradient descent approach.

The intuition behind the max-flow segmentation can be drawn from the idea of finding a cut with minimum capacity that will result in two disjoint partitions, one associated with the source and other with the sink. Let us consider a source flow $p_s(x)$ that is optimal but unsaturated, i.e., $p_s(x) \leq C_s(x)$ (see Figure 5.3(a) for reference). Since the optimal source flow is unsaturated, it has no contribution to the total energy. As a result, any variation in the source flow should not change the total energy and therefore, $1 - \lambda(x)$ must be equal to zero,

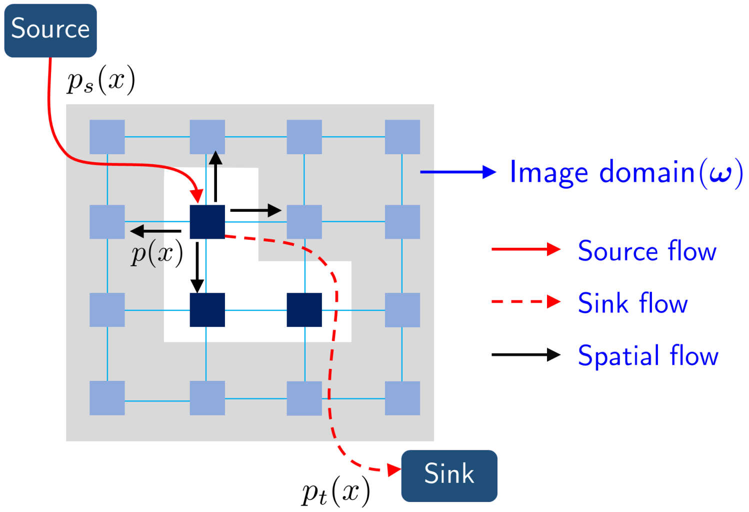

Figure 5.2: Representation of the continuous image domain where each of the sites are associated with source, sink and spatial flows represented by $p_s(x), p_t(x), p(x)$, respectively.

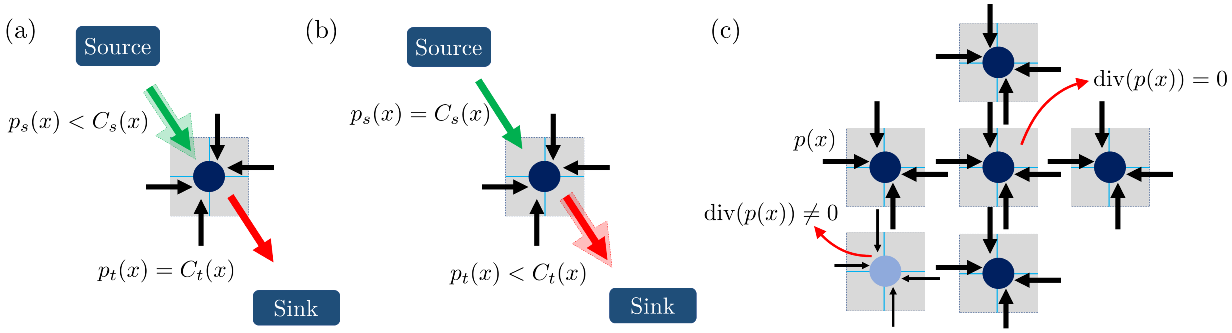

Figure 5.3: Visualization of the flow fields. (a) When the flow through x is limited by the sink flow capacity such that the sink flow contributes to the total energy (b) when the flow through x is limited by the source flow capacity such that the source flow contributes to the total energy and (c) shows two cases of divergence of the spatial flow. The spatial flow where $\mathrm{div}p(x) \neq 0$ contributes to the total energy. We omit the edges connecting non-adjacent sites for the sake of clarity.

or $\lambda(x) = 1$. This implies that $p_t(x) = C_t(x)$, i.e., the flow from site x to sink t is saturated and the minimum cut passes through this edge. Similarly, the unsaturated sink flows, i.e., $p_t(x) \leq C_t(x)$ lead to saturated flows from source s to the site x as shown in Figure 5.3(b). For this case, the minimum cut severs the source flow and assigns the site x to the sink (i.e, $\lambda(x) = 0$). Finally, for the case of spatial flows, the sites for which $\mathrm{div}p(x) \neq 0$ are the candidates for minimum cut. In other words, the maximum flow occurs through the sites that are saturated, and therefore, are the candidates for minimum cut (see Figure 5.3(c)).

However, difficulties arise when estimating the flow capacities. Generally the flow capacities are defined as $C_s(x) = D(I(x) - s(x)), C_t(x) = D(I(x) - t(x))$ where $I(x)$ is the image matrix containing pixel intensities, $D(.)$ is some user defined function and $s(x)$ and $t(x)$ are selected *a priori* [161] or defined heuristically [13]. Nonetheless, the flow capacities are generally unknown and require trial and error or user inputs in the form of bounding boxes or scribbles for estimation. To argue the importance of flow capacities in optimally solving the max-flow problem, we begin with a trivial case of uniformly constant source and sink flow capacities. In such a scenario, sites have no preference to be assigned to the source or the sink and consequently, all the sites are either assigned to the source or the

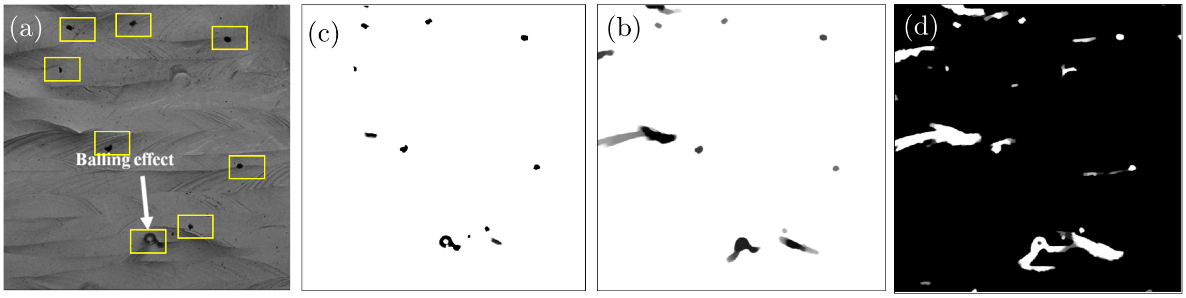

Input image $s(x) = 0.2$ $s(x) = 0.28$ $s(x) = 0.35$

Figure 5.4: Representative example to illustrate the effect of variations in the source flow capacity on the segmentation result. (a) Input image showing the defects. Segmentation using the continuous max-flow approach with $t(x)$ and spatial flow capacities fixed to 0.3 and 0.1 respectively, but with varying values of $s(x)$. (b) $s(x) = 0.2$, (c) $s(x) = 0.28$ and (d) $s(x) = 0.35$.

sink depending on which flow field is saturated first. Appleton and Talbot [13] addressed this problem by defining a weighting function that decays as per the power-law in the neighborhood of user defined initialization or seed points. Alternatively, Boykov and Kolmogorov [33] used the Cauchy-Crofton formula to arrive at the (edge) capacities. However, both of these approaches required manual intervention to define the seed points.

For cases where flow capacities are spatially varying, the segmentation result may still vary significantly if the values are not optimally chosen. To demonstrate this, we consider the problem of identifying defects (marked with yellow boxes in Figure 5.4(a)) on an additively manufactured component (see Section 6.3 for additional details). To define the flow capacities, we use $D(.) \equiv |.|$ and $t(x) = 0.3$. Figures 5.4(b-d) show the segmentation results for three different values of $s(x)$. We note that even small perturbations in the value of $s(x)$ result in vastly different segmentation; demonstrating the need for estimating the flow capacities to optimally solve the max-flow problem.

5.4 Estimation of flow field capacities

In this section, we develop an approach to estimate the image labels $\lambda(x)$ by solving the continuous max-flow problem while optimally estimating the flow capacities from the image characteristics. Towards this, we first formulate the problem of estimating $\lambda(x)$ as a MAP estimation problem. Given the image $I(x)$ and the flow capacities $\mathcal{C}(x) = \{C_s(x), C_t(x), C(x)\}$, the objective of the MAP estimation is to find the image labels $\lambda(x)$ that maximizes the posterior probability given as,

$$\lambda(x) = \arg\max_{\lambda(x)} P(\lambda(x)|\mathcal{C}(x), I(x)) \tag{5.6}$$

Since the flow capacities are unknown, we estimate the image labels $\lambda(x)$ in Equation (5.6) by iteratively solving the following two subproblems,

$$\lambda^{\tau+1}(x) = \arg\max_{\lambda(x)} P(\lambda(x)|\mathcal{C}^{\tau}(x), I(x)) \tag{5.7a}$$

$$\mathcal{C}^{\tau+1}(x) = \arg\max_{\mathcal{C}(x)} P(\lambda^{\tau+1}(x)|\mathcal{C}(x), I(x)) \tag{5.7b}$$

where $\lambda^{\tau+1}(x)$ and $\mathcal{C}^{\tau+1}(x)$ are respectively the image labels and the flow capacities at iteration $\tau+1$. The first subproblem (Equation (5.7a)) is essentially maximizing the posterior distribution of the image labels given the image $I(x)$ and the most recent estimate of flow capacities, i.e., $\mathcal{C}^{\tau}(x)$. In the second subproblem (Equation (5.7b)), we employ the updated estimate of $\lambda^{\tau+1}(x)$ to subsequently update the flow capacities. The process is repeated until a stopping criterion (or convergence) is reached.

5.4.1 Maximum a posteriori estimation of $\lambda(x)$

We now employ a MAP estimation approach to determine the optimal image labels $\lambda(x)$ by solving the first subproblem as given in Equation (5.7a). Using Bayes theorem we have,

$$\lambda^{\tau+1}(x) = \arg\max_{\lambda(x)} \log(P(I(x)|\lambda(x), \mathcal{C}^{\tau}(x))) + \log(P(\lambda(x)) \tag{5.8}$$

Here, the first term is the log-likelihood of the image labels $\lambda(x)$ given the flow capacities and the image $I(x)$. In other words, it imposes a penalty for every incorrect assignment of the labels. Assuming the observations (i.e., pixel intensities contained in $I(x)$) are independently and identically distributed we can write,

$$P(I(x)|\lambda(x), \mathcal{C}^\tau) \propto \exp(-D(\mathcal{C}^\tau, \lambda(x), I(x))) \tag{5.9}$$

where $D(\mathcal{C}^\tau, \lambda(x), I(x))$ is the data penalty function defined as,

$$D(\mathcal{C}^\tau, \lambda(x), I(x)) = \int_{\boldsymbol{\omega}} (1 - \lambda(x)) C_s^\tau(x) + \lambda(x) C_t^\tau(x) dx$$

The second term in Equation (5.8) is the logarithm of the prior over flow capacities. To enforce spatial smoothness, we define $P(\lambda(x))$ as,

$$P(\lambda(x)) \propto \exp\left(-V(C^\tau(x), \lambda(x))\right) \tag{5.10}$$

where $C^\tau(x)$ is the estimate of spatial flow capacity at iteration τ and $V(C^\tau(x), \lambda(x))$ is the smoothness penalty given as,

$$V(C^\tau(x), \lambda(x)) = C^\tau(x) \int_{\boldsymbol{\omega}} |\nabla \lambda(x)| dx$$

Substituting the values of $P(I(x)|\lambda(x), \mathcal{C}^\tau)$ and $P(\lambda(x))$ in Equation (5.8), we have,

$$\lambda^{\tau+1}(x) = \arg\min_{\lambda(x)} \int_{\boldsymbol{\omega}} (1 - \lambda(x)) C_s^\tau(x) + \lambda(x) C_t^\tau(x) + C^\tau(x) |\nabla \lambda(x)| dx$$

We note that the maximization of the posterior probability in Equation (5.7a) is equivalent to solving the max-flow problem given the flow capacities are known. We, therefore, simply use Algorithm 1 to find the optimal values of $\lambda^{\tau+1}(x), p_s^{\tau+1}(x), p_t^{\tau+1}(x)$ and $p^{\tau+1}(x)$ at iteration $\tau + 1$.

5.4.2 Maximum a posteriori estimation of $\mathcal{C}$

We now look at the second subproblem, i.e.,

$$\mathcal{C}^{\tau+1}(x) = \arg\max_{\mathcal{C}(x)} \log P(\lambda^{\tau+1}(x)|\mathcal{C}(x), I(x)) + \log P(\mathcal{C}(x)) \tag{5.11}$$

Here, the first term is the log-likelihood of the flow capacities $\mathcal{C}(x)$ given the image $I(x)$ and the most recent estimate of the image labels $\lambda^{\tau+1}(x)$ and $P(\mathcal{C}(x))$ is the prior distribution over the flow capacities. Note that the prior over the flow capacities is critical to enforce spatial smoothness and optimally solving the max-flow problem as discussed in Section 3. Several approaches have been proposed in the literature to capture the spatial smoothness, most commonly using MRF priors [34, 65, 55]. Using the prior presented in [109], we propose a new MRF prior that is computationally fast and enforces spatial smoothness. For the simplicity of notations, we only focus on the estimation of the source flow capacity given as $C_s(x) = |I(x) - s(x)|$. Results may be generalized for estimating the sink and spatial flow capacities similarly.

5.4.2.1 Prior over the flow fields

MRF priors have been widely used to capture the spatial smoothness in segmentation problems. One of the most commonly used families of MRF priors is given as,

$$p(s(x)) = \frac{1}{Z} \exp\left(-\frac{1}{T} U(s(x))\right) \tag{5.12}$$

where Z is a normalizing constant, T is a scale factor and $U(s(x))$ is a smoothing function that controls the spatial correlation between the sites $x \in \boldsymbol{\omega}$ in a given neighborhood [93]. The prior follows from the Hammersley-Clifford Theorem [67] when assuming the local Markovian property over the flow field, that is, $p(s(x)|\boldsymbol{\omega}\backslash x)) = p(s(x)|x \in \mathcal{N}(x))$ where $\mathcal{N}(x)$ is the . It may be noted that the local Markovian property is quite natural for random fields defined over an image domain [34].

Several choices of the smoothing function have been proposed in the literature, e.g., see [93, 25]. However, the complexity of the posterior computation remains one of the critical challenges under MRF priors. To minimize the computational complexity, we present the following smoothing function based on [109],

$$U(s^{\tau+1}(x)) = -\sum_{x\in\boldsymbol{\omega}} \left(G_s^{\tau}(x) + \beta(1 - p_s^{\tau}(x))\right) \log\left(s^{\tau+1}(x)\right) \tag{5.13}$$

where the multiplier $G_s^{\tau}(x)$ is defined as,

$$G_s^{\tau}(x) = \exp\left(\frac{\beta}{2|\mathcal{N}(x)|} \sum_{y\in\mathcal{N}(x)} \left(p_s^{\tau}(y) + s^{\tau}(y)\right)\right) \tag{5.14}$$

Here, $|\mathcal{N}(x)|$ is the cardinality of the neighborhood of x, $p_s^{\tau}(x)$ and $s^{\tau}(x)$ are the current estimates of the source flow $p_s(x)$ and $s(x)$, respectively, and β is a smoothing constant. The term $G_s^{\tau}(x)$ in Equation (5.13) enforces spatial smoothness by mean filtering over the neighborhood $\mathcal{N}(x)$. This minimizes the slack between the flow field and flow capacity. Although the smoothing function is heuristically designed, an inherent advantage is that when maximizing the log-likelihood function the derivative is dependent only on the term $s^{\tau+1}(x)$ at the step $\tau+1$, thereby contributing to the computational efficiency. In the present implementations, we set the value of $\beta = 5$ and the neighborhood size as 5×5 over $\boldsymbol{\omega}$ such that $|\mathcal{N}(x)| = 25$. See [109] for details on the parameter selection.

5.4.2.2 Updating the flow capacities

We now determine the value of the source flow capacities $C_s^{\tau+1}(x)$ by maximizing the posterior probability in Equation (5.11). With respect to $s^{\tau+1}(x)$, we have,

$$\frac{d}{ds^{\tau+1}(x)}\left(\log P(I(x)|\mathcal{C}(x), \lambda^{\tau+1}(x)) + \log P(\mathcal{C}(x))\right) = 0$$

Algorithm 1: Iterative MAP estimate of source, sink and spatial capacities

```
Initialize: Initialize the parameters $\lambda^{(0)}, p_s^{(0)}(x), p_t^{(0)}(x), p^{(0)}(x)$ and $\mathcal{C}^{(0)}(x)$
repeat
    Solve the continuous max-flow problem in Equation (5.5) to estimate
      $\lambda^{\tau}(x), p_s^{\tau}(x), p_t^{\tau}(x)$ and $p^{\tau}(x)$;
    Evaluate the current estimate of $G_s^{\tau+1}(x)$ in Equation (5.14) and $G_t^{\tau+1}(x)$;
    Update the flow capacities as:
    $C_s^{(\tau+1)}(x) = |I(x) - (G_s^{\tau}(x) + \beta(1 - p_s^{\tau}(x)))\,|$
    $C_t^{(\tau+1)}(x) = |I(x) - (G_t^{\tau}(x) + \beta p_t^{\tau}(x))\,|$
    $C^{\tau+1}(x) = |\int_{\boldsymbol{\omega}} C_s^{\tau+1}(x)dx - \int_{\boldsymbol{\omega}} C_t^{\tau+1}(x)dx|$
until convergence;
```

For the first term, we refer to Equation (5.9) and consider the dual of the corresponding minimization problem stated in Equation (5.4). Using Lagrange multipliers $\eta(x)$ for the source constraints, we have,

$$s^{\tau+1}(x) = \frac{1}{T}\frac{G_s^{\tau}(x) + \beta(1 - p_s^{\tau}(x))}{\eta(x)}$$

For simplicity, we use $T = \eta(x)^{-1}$ such that the source flow capacity in iteration $\tau + 1$ is given as,

$$C_s^{(\tau+1)}(x) = |I(x) - (G_s^{\tau}(x) + \beta(1 - p_s^{\tau}(x)))\,| \tag{5.15}$$

Similarly, we update the sink and spatial flow capacities. The algorithm for simultaneous update of all the flow capacities is given in Algorithm 2.

5.5 Convergence and consistency

Inconsistency of the posterior is one of the biggest challenges while working with heuristic or otherwise non-standard priors as noted by Freedman [63]: *the set of all parameter-prior pairs* $(\theta, p) \in \Theta \times \mathcal{P}$ *for which the posterior is consistent at* θ *is a meager set.* Inconsistency is more common than expected and may lead to incorrect inferences. To avoid situations like this and others as indicated in [23], we show that the posterior probability of the flow capacities based on the MRF prior with smoothing function given in Equation (5.13) is consistent.

Let us consider the set of independently and identically distributed image observations $I(x)$ taking values in the measurable space $(\Omega, \mathcal{B})$ and are sampled from some unknown "true" distribution function F_0 with density function f_0. Given the observations $I(x)$, let $p(s(x)|I(x))$ denote the posterior distribution of $s(x)$. Let μ be a probability measure on the measurable space $(\Omega, \mathcal{B})$. We define a ε-Hellinger neighborhood of the true distribution F_0 as $s_\varepsilon(x) = \{F \in \mathcal{P} : H(F_0, F) \leq \varepsilon\}$ where $H(F_0, F)$ denotes the Hellinger distance and is given as,

$$H(F_0, F) = \left\{ \left(\int \sqrt{f_0} - \sqrt{f} \right)^2 \mu(d\omega) \right\}^{1/2}$$

and $\mathcal{P}$ is the subset of all finite probability measures that are absolutely continuous with respect to μ. Then the consistency of the posterior distribution relies on the following two assumptions [23],

Assumption 1. *For every $\varepsilon > 0$, $p(N_\varepsilon) > 0$ where N_ε is the ε-Kullback-Leibler neighborhood [23] of F_0.*

Assumption 2. *For every $\varepsilon > 0$, there exists a sequence $\{\mathcal{F}_{n=1}^{\infty}\}$ of subsets of $\mathcal{P}$, and positive real numbers c, c_1, c_2, δ with $c < ([\varepsilon - \sqrt{\delta}]^2 - \delta)/2$, $\delta < \varepsilon^2/4$, such that:*

1. *$p(\mathcal{F}_n^c) \leq c_1 \exp(-nc_2)$ for all but finitely many n, and*
2. *$\mathcal{H}(\mathcal{F}_n, \delta) \leq nc$ for all but finitely many n where $\mathcal{H}$ is the δ-metric entropy of $\mathcal{F}_n$ (see Definition 1 in [23]).*

Intuitively, Assumption 1 is needed to ensure positive prior probability in the neighborhood of F_0. The second assumption prevents the prior from giving substantial mass to distributions with "wiggly" densities (condition (i)). This is realized by imposing exponentially small probability to the complement of the sequence $\mathcal{F}_n$ of well behaved densities, i.e., not wiggly. Condition (ii) ensures that the sequence $\mathcal{F}_n$ of densities are well-behaved. Under these assumptions, [23] showed that the posterior distribution is consistent at F_0, i.e., the posterior concentrates all the mass in the ε-Hellinger neighborhood almost surely with probability 1. More formally, we have,

Theorem 3. *The posterior concentrates all the mass in the ε-neighborhood of F_0 almost surely, i.e., $p(s_\varepsilon(x)|I(x)) \to 1$ almost surely as $n \to \infty$.*

To show that the result holds, we first present the following lemma.

Lemma 5. *The MRF prior $p(s(x))$ in Equation (5.12) belongs to an exponential family.*

Proof. *Plugging the values of $U(s(x))$ and $G(x)$ from Equations (5.13) and (5.14), respectively in Equation (5.12), we have:*

$$p(s(x)) = \frac{1}{Z}\exp\left(\frac{1}{T}\sum_{\boldsymbol{\omega}}[e^{c_3(\tilde{p}_s+\tilde{s})} + \beta(1-p_s(x))]\log(s(x))\right)$$

where $c_3 = \beta/2\mathcal{N}(x)$, $\tilde{p}_s = \sum\limits_{y\in\mathcal{N}(x)} p_s(y)$, and $\tilde{s} = \sum\limits_{y\in\mathcal{N}(x)} s(y)$. Factorizing the parameter and variable terms, we rewrite $p(s(x))$ as,

$$p(s(x)) = \exp\left(\sum_{\boldsymbol{\omega}}[e^{c_3\tilde{p}_s}\log(s(x)) + \beta\log(s(x))] - \sum_{\boldsymbol{\omega}}[\beta p_s(x)\log(s(x)) - e^{c_3\tilde{s}}\log(s(x))]\right)$$

Since the product of exponential families belongs to the exponential family, $p(s(x))$ belongs to the exponential family. □

Given the Assumptions 1 and 2 and the prior $p(s(x))$ belonging to the exponential family, the posterior consistency and therefore, the proof of Theorem 1 follows from [23]. In the next section, we present the implementation results and comparison with state-of-the-art segmentation methods.

5.6 Experimental results

5.6.1 Case studies and evaluation metrics

To test the efficacy of the proposed methodology, we investigate two real-world case studies: Brain Tumor Segmentation (BraTS) using MR images. Both supervised as well as

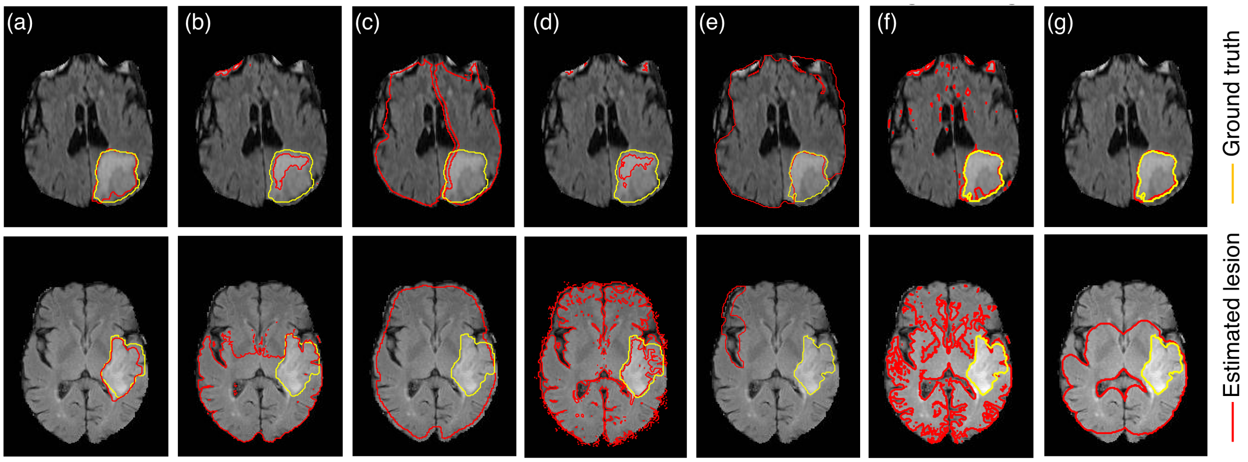

Figure 5.5: Segmentation results of different unsupervised approaches for the segmentation of brain tumor on HG (top row) and LG (bottom row) glioma. (a) The proposed method (b) mean shift (c) normalized cuts (d) blobworld (e) hierarchical image segmentation (f) GMM and (g) spatially constrained GMM.

unsupervised segmentation approaches have been reported in the literature with the majority being supervised. Therefore, we compare our segmentation results with both supervised as well as unsupervised algorithms. For the first case study, we refer to the supervised algorithms reported in the Medical Image Computing and Computer Assisted Intervention Society (MICCAI) proceedings 2013 and 2015 [103]. In the 2013 MICCAI proceedings, 20 algorithms were reported that include five generative, 13 discriminative and two generative-discriminative algorithms. In the 2015 BRATS dataset, three generative, two discriminative and seven neural network/deep learning approaches were reported. For unsupervised segmentation, we refer to k-means, expectation maximization (also referred to as blobworld) [43], Gaussian mixture model (GMM), GMM with spatial regularization (SC-GMM) [109], mean shift [49], normalized cuts [132], and hierarchical image segmentation [14]. Due to the limited dataset in the second case study, we compare the performance with only unsupervised algorithms.

To quantitatively compare the performance of the segmentation results, we refer to the

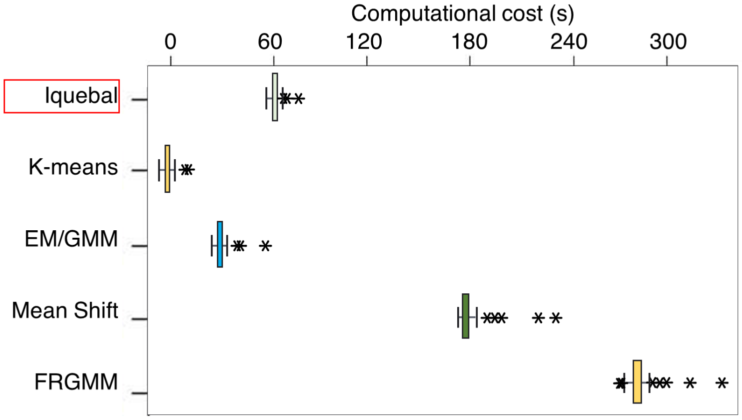

Figure 5.6: Comparison of the computational cost among the unsupervised algorithms that converged.

standard Dice score and the Hausdorff distance. The Dice score is given as,

$$\text{Dice}(\hat{\mathcal{R}}, \mathcal{R}) = 2\frac{|\hat{\mathcal{R}} \cap \mathcal{R}|}{|\hat{\mathcal{R}} + \mathcal{R}|} \tag{5.16}$$

where $\hat{\mathcal{R}}$ and $\mathcal{R}$ represent the segmented lesion/defects and the expert segmentation, respectively, and $|.|$ represents the size of the domain. Dice score measures the areal overlap or the agreement between the segmented area and the ground truth. The Hausdorff distance instead measures the surface distance between the segmented area and the ground truth and is given as,

$$\text{Haus}(\hat{\mathcal{R}}, \mathcal{R}) = \max\{\sup_{i \in \hat{\mathcal{R}}} d(i, \mathcal{R}), \sup_{j \in \mathcal{R}} d(j, \hat{\mathcal{R}})\} \tag{5.17}$$

where $d(j, \hat{\mathcal{R}})$ is the shortest Euclidean distance between the sites in $\mathcal{R}$ and $\hat{\mathcal{R}}$. Taking maximum over the supremum of these Euclidean distances make Hausdorff distance highly sensitive to the outliers present in $\hat{\mathcal{R}}$. To control this, we use the 95th percentile of the Hausdorff distance as suggested in [103].

5.6.2 Brain Tumor Segmentation

Despite significant advances over the past few years, the diagnosis of glioma—the most common type of brain tumor—remains limited. Neuroimaging offers a noninvasive approach

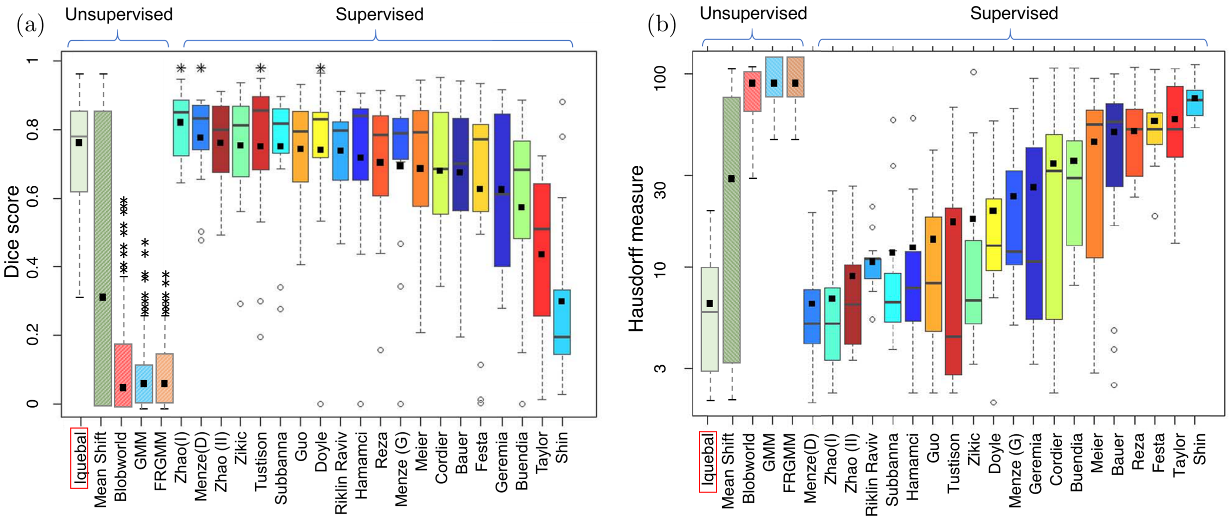

Figure 5.7: Comparative results of different algorithms tested for the segmentation of brain tumor on the BRATS 2013 dataset. Box plot adopted from [103]

to evaluate the progression of the lesions, thus allowing timely intervention and controlled treatment. In this study, we use the publicly available FLAIR-MR scans from BraTS 2013 and 2015 challenge. There are a total of 20 high grade (HG) and ten low grade (LG) glioma cases in the BraTS 2013 dataset and 274 HG and 54 LG glioma in the BraTS 2015 dataset. Each of these datasets contains annotated ground truth, already delineated by the clinical experts. All the images were resampled to the size of 240×240.

Segmentation results of a representative HG and LG glioma are presented in the top and bottom rows of Figure 5.5, respectively. The segmentation results for the present approach is shown in Figure 5.5(a) followed by rest of the unsupervised segmentation methods in Figures 5.5(b)-(g). Note that some of the methods such as mean shift (Figures 5.5(b)) required setting the bandwidth and kernel function whereas completely unsupervised methods such as normalized cuts (Figures 5.5(c)) failed to converge. Clearly, the present method performs better as compared to the unsupervised methods tested. The overall performance of the present algorithm is 78% and 75.6% on the Dice score for the BraTS 2013 and BraTS 2015 dataset, respectively. The 95% Hausdorff distance for the two datasets are 13.61 and 14.05, respectively. Based on the segmentation results, we also note that the present approach significantly minimizes oversegmentation as compared to most of the segmentation approaches reported in Figure 5.5. This is due to the TV regularization in the max-flow formulation that penalizes the oscillations in the pixel intensity due to random noise. We also compare the computational cost of the unsupervised algorithms that converged within a reasonable time and is summarized in Figure (5.6). Although our method is slower than k-means and GMM, it performs reasonably fast as compared to mean-shift and spatially constrained GMM.

The Dice score and the Hausdorff distance of all the methods including the supervised as well as unsupervised methods tested on the BraTS 2013 dataset are summarized in Figures 5.7(a) & 5.7(b). Interestingly, the present approach outperforms most of the supervised algorithms, both in terms of the average values of the Dice score and the Hausdorff distance (black squares inside the box plot indicate the average). The results suggest more than 90% improvement in the Dice score and more than 56% reduction in the Hausdorff distance when compared to the unsupervised methods. In terms of the supervised approaches, the present method performs statistically similar to the best performing method (Zhao(I) in [102]). For the BraTS 2015 dataset, no test results were available at the time of writing this chapter, so we only compare with the training results of the algorithms as reported in the MICCAI 2015 proceedings [103]. These results are summarized in Table 5.1. Indeed, most of the deep learning based method outperform the results of the present algorithm. Nonetheless, the Dice scores for all the supervised methods reported in Table 1 were calculated on the training dataset where the training sizes were more than 85% of the whole dataset [144].

5.6.3 Defect concentration in additively manufactured components

Recent advances in the manufacturing technologies, especially metal additive manufacturing (i.e., layer-by-layer deposition of metal powder to fabricate complex free-form surfaces) have revolutionized the landscape of fabricating industrial components and parts. Despite the capability of AM to fabricate components with minimum time and material waste, the overall functional integrity of AM components is considered much inferior to those realized with conventional manufacturing process chains, especially under real-world dynamic load-

Table 5.1: Dice score comparison for the BRATS 2015 dataset

Approach Summary	Dice score	Author
Unsupervised max-flow	75.6±10.5	Iquebal
Generative with shape prior	77±19	Agn [102]
Generative-Discriminative	83±7.5	Bakas [102]
Expectation Maximization	68	Haeck [102]
Random Forests	84	Maier [102]
Random Forests	80.7	Malmi [102]
Conditional Random Fields	82	Meier [102]
Conv. Neural Networks	88	Havaei[102]
Conv. Neural Networks	81±15	Dvorak [102]
Conv. Neural Networks	86	Pereira [102]
Conv. Neural Networks	67	Rao [102]
Conv. Neural Networks	81.41±9.6	Vaidhya [102]
Conv. Neural Networks	87.55±6.72	Wang [144]

ing conditions [18]. Defects, such as pores, undiffused metal powder, geometric distortions, surface cracks, and non-equilibrium microstructures significantly deteriorates the mechanical performance and overall functional integrity of the components.

Concentration of defects in AM components is largely affected by the parameters of the AM process, e.g., laser power, laser scanning speed [18]. Controlling the process parameters can help manufacturers realize components with minimum defects and superior functional integrity [139]. *In situ* imaging technologies allow monitoring and detection of the defects induced in AM components. However, detection of defects using *in situ* imaging technologies has its own limitations: (a) recording high-resolution images are costly, and therefore, only limited data is available, (b) uncertainties in the shape and morphology of defects, (c) low signal to noise ratio, etc.

In this case study, we employ the present approach to determine the concentration of defects on two different AM components that were fabricated with different process parameters using a laser-based AM process called selective laser melting (SLM). The process parameters investigated in this case study are laser power, laser scanning speed, and relative density of the AM components. For the first component (sample A, Figure 5.8(a)) the process parame-

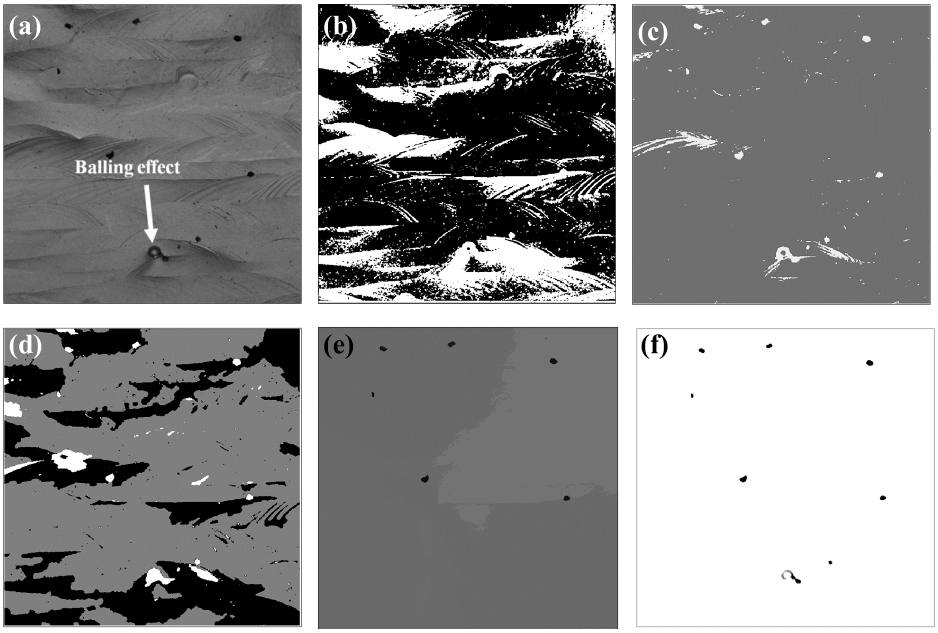

Figure 5.8: Comparative results of different algorithms tested for the segmentation of defects on sample A. (a) Original image for sample A (b) k-means with 2 clusters (c) Gaussian mixture model with expectation maximization (d) spatially constrained Gaussian mixture model with k-means initialization and (e) mean shift (f) the proposed method.

ters were set to: laser power = 165 W, laser scanning speed = 138 mm/s, and relative density = 99.5%. For the second component (sample B, Figure 5.9(a)) these parameters were set to: laser power = 85 W, laser scanning speed = 71 mm/s, and relative density = 96.4%. The images of the AM components were recored using an SEM (see [18] for details) and the defects were manually annotated to get the ground truth.

We mainly focus on the concentration of two different types of defects namely, pores and balling effect. Pores are essentially voids on the surface that are formed when gas particles trapped in the melt-pool (liquefied metal during deposition) escape. These are generally tracked by observing the dark spherical/oval shaped features on the surface. In contrast, balling effect is a complex metallurgical process that originates due to sub-optimal process parameters during the SLM process as well as the properties of the material powder such as the relative density of AM components. It causes the liquid scan track during SLM to break and result in the formation of spherical particles that eventually get trapped, causing inhomogeneous deposition of the powder in the next build layer. Authors in [18] showed that by increasing the laser power, the concentration of defects due to the balling effect decreases. Controlling pores as well as the balling effect is critical to avoid significant costs, as these defects may reduce the fatigue strength of material by more than 4 times, resulting in early, unexpected failure [77].

Figure 5.8(a) and 5.9(a) shows the representative surface from sample A and sample B, respectively. We note that sample A with high laser power (165 W) has relatively lower defect concentration as compared to sample B with low laser power (85 W). As the data size is limited, we compare our segmentation results only with that of the unsupervised segmentation methods. To keep the comparison fair, we ignore the methods that either required user inputs to define the foreground and background or did not converge in a reasonable time. The segmentation results for the first sample are presented in Figures 5.8(b-f). The effect of the noise (resulting from the shadow and underexposure) is clearly reflected in the results obtained from k-means clustering approach as shown in Figure 5.8(b). Although, there is some improvement in the segmentation obtained from GMM and SC-GMM as shown in Figure 5.8(c-d), yet the effect of noise is evident from the resulting oversegmentation. The segmentation from the mean shift algorithm (Figure 5.8(e)) is able to detect most of the pores (with 58.6% Dice score) but fails to detect the balling effect. Finally, the segmentation obtained with the proposed method is able to identify all the regions containing pores as well as the balling effect with a Dice score of 70.56% and Hausdorff distance of 32—approximately 86% smaller than the rest of the unsupervised segmentation methods (Figure 5.8(f)).

In the second sample, noise is significantly higher as compared to sample A, mainly due to the rougher surface morphology. Three instances of balling effect were identified manually as shown by the arrows in Figure 5.9(a), alongside multiple pores. Clearly, the segmentation results obtained from k-means (Figure 5.9(b)), GMM (Figure 5.9(c)), SC-GMM (Figure 5.9(d)) and mean shift (Figure 5.9(e)) mostly capture the noise present in the original image. In contrast, the proposed method is able to selectively segment the defects

Table 5.2: Average Dice score and Hausdorff measure of various unsupervised approaches implemented for defect segmentation.

Approach	Dice score	Hausdorff measure
Unsupervised max-flow	70.56	32
Mean shift	58.6	245
GMM	22.16	287
SC-GMM	2.6	219
k-means	1.4	321

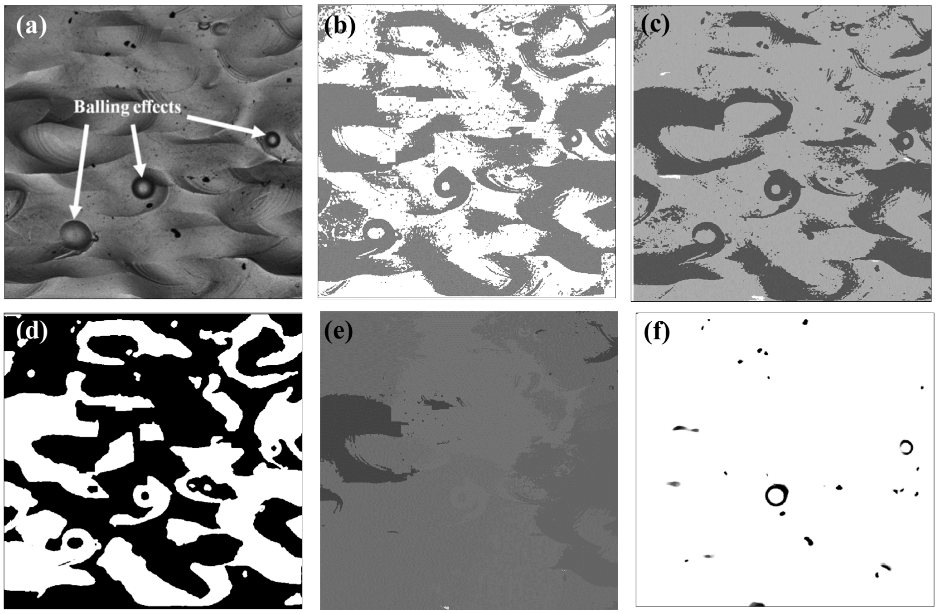

Figure 5.9: Comparative results of different algorithms tested for the segmentation of defects on Sample B. (a) Original image for sample B (b) k-means with 2 clusters (c) Gaussian mixture model with expectation maximization (d) spatially constrained Gaussian mixture model with k-means initialization and (e) mean shift (f) the proposed method.

while significantly reducing the oversegmentation (Figure 5.9(f)). However, the algorithm is able to identify only two out of the three areas showing balling effect. Nonetheless, the segmentation is a significant improvement over the standard state-of-the-art unsupervised segmentation methods. A summary of the Dice score and the Hausdorff measure of all the unsupervised approaches is presented in Table 5.2.

As mentioned earlier, estimating defect concentration in AM can help understand the effect of various process parameters on the build quality, and therefore determine the optimal parameter settings [77, 18]. Via visual inspection, we were able to verify the experimental observations [18] that the increase in the laser power results in the decrease in defect concentration. By estimating the area fraction of defects from segmented images, we note that the defect concentration on sample A is $\sim$1% and sample B is $\sim$ 4.39%. This is in accordance with the experimental observations. From a process standpoint, the present approach may be integrated with an experimental design strategy to determine the optimal process parameter settings that would minimize the defect concentration.

5.7 Summary and conclusions

Advances in microscopy and functional imaging technologies open exciting opportunities for fast and on the fly detection/segmentation of ROIs using image snapshots and streams. However, the uncertainty associated with the shape and location of ROIs renders the task of generating annotations and atlases extremely costly and time-consuming. Although considerable research exists in the image segmentation literature, a majority of the methods rely on huge training datasets or require manual intervention to set the parameters *apriori*. In contrast, only a handful of unsupervised approaches have been reported in the literature, many of which are computationally complex (e.g., normalized cuts) or require partial supervision (e.g., continuous max-flow).

In the chapter, we developed an approach to consistently estimate the flow capacity parameters leading to a fully unsupervised image segmentation approach. Our framework is based on iteratively estimating the image labels using a continuous max-flow approach followed by the MAP estimation of the flow capacities by considering an MRF prior over the flow field. In the sequel, we presented results to validate the consistency of the posterior distribution of the flow capacities to ensure that the estimated flow capacities are consistent under the MRF prior proposed in this work. Segmentation results on two distinct real-world case studies, including brain tumor segmentation (BraTS) using FLAIR-MR scans and defect segmentation in additively manufactured components using SEM images are presented. An extensive comparison with the state-of-the-art unsupervised as well as supervised algorithms suggests that the present method outperforms all the unsupervised as well as most of the supervised algorithms tested. More specifically, we note that the present approach results in more than 90% improvement in the Dice score and more than 56% reduction in the Hausdorff distance when compared to the unsupervised methods. Future works are focused on the segmentation of 3D images as well as a more comprehensive Bayesian model to estimate the parameters used in the MRF prior.

6. LEARNING ACOUSTIC EMISSION SIGNATURES FROM A NANOINDENTATION-BASED LITHOGRAPHY PROCESS: TOWARDS RAPID MICROSTRUCTURE CHARACTERIZATION *

We present an approach for rapid identification of the salient microstructural phases present on a metallic workpiece surface via nanoindentation-based lithography process. We employ a machine learning approach to connect the time-frequency patterns of the corresponding acoustic emission (AE) signals with the underlying microstructural phases. Results show that the AE frequencies in the range of 0.3-1 kHz and 30-50 kHz can discriminate between the microdynamics of the lithography process arising from different microstructural compositions and thereby predict these microstructural phases with accuracies exceeding 95%. We also draw physical interpretations of our "black-box" machine learning model and demonstrate that the physical insights into the underlying AE signals allow us to identify novel patterns and possible microstructural anomalies.

6.1 Introduction

Discovery of advanced, functional materials is the key to several technological advancements in aerospace, medical, electronics, and other related sectors. Conventionally, materials discovery involves an iterative sequence of design, synthesis, and characterization steps. While recent advances in high-performance computing and automation have accelerated the design and synthesis of novel materials, characterization still remains an extremely slow process [17, 10]. With recent advancements in machine learning and sensor technologies, nanoindentation instruments can be instrumented to server as platforms to enable rapid characterization.

Characterization of the materials structure, specifically the microstructures is important

---

*Reprinted with permission form A. S. Iquebal, S. Pandagare, and S. T. S. Bukkapatnam, "Learning acoustic emission signatures from a nanoindentation-based lithography process: Towards rapid microstructure characterization," Tribology International, vol. 143, p. 106074, Copyright 2019 Elsevier as they directly influence the resulting materials property and performance [6]. Developments in additive and other manufacturing technologies have led to the realization of materials with radically different types of microstructures—at unprecedented speeds—some of which were not known to exist heretofore [48, 126]. These novel microstructures may hold unprecedented properties that can dramatically enhance the materials performance envelope for industrial applications. Once the microstructures with the desired (or unexpected) properties are identified, one can investigate the thermodynamic pathways [167], and subsequently determine the processing routes conducive for their realization in bulk (i.e., solve the inverse problem [6]).

In order to systematically investigate these microstructures and hence the local mechanical properties, one needs to comprehensively map out the "spectrum" of different phases, including their shape, size, orientation, and spatial distribution realized from a process. The conventional approach for characterizing the microstructures involves a battery of cumbersome and time-consuming characterization tests, e.g., scanning electron microscopy (SEM), X-ray diffraction, mechanical testing [92]. Such an approach is untenable for estimating the properties of potentially hundreds and more of the material microstructures realized through a process within a reasonable time [111].

Recent advances in machine learning, together with those in MEMS (microelectromechanical systems) sensors and characterization techniques, most pertinently in micro/nanoindentation [79] and lithography instrumentation [166] provide a radically new way to rapidly map out the microstructures and estimate the associated properties [47, 58, 117]. In this work, we investigate a nanoindentation-based lithography process coupled with *in situ* acoustic emission (AE) sensing to enable rapid identification of microstructures.

A nanoindentation-based scanning probe lithography process (referred to as lithography in the remainder of the chapter) consists of creating specific contours on the surface of a given material through the controlled motion of a diamond indenter, typically within a nanoindentation platform [29]. Such lithography processes are particularly interesting as they offer

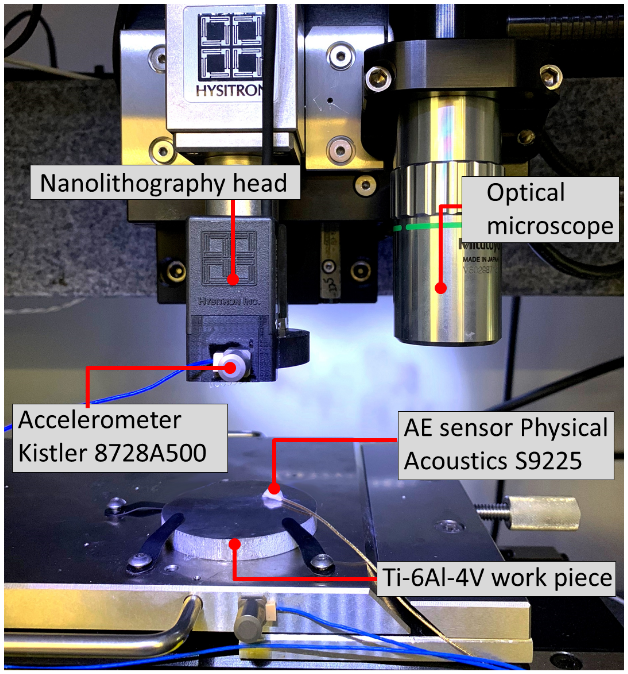

Figure 6.1: The Hysitron TI 950 nanoindentation setup employed in the current study showing the Ti-6Al-4V workpiece sample integrated with the AE sensor.

an approach to rapidly track the microstructural fingerprint by recording the corresponding microdynamics using high-resolution AE sensors [46]. Here, the microdynamics of the lithography process consists of various physical transformations at the indenter-material interface including plastic deformation, shear localization, microcrack propagation, as well as other contact mechanisms [27, 131]. AE sensors capture the microdynamics of the lithography process by tracking the high-frequency micro-elastic pulses produced as the indenter traverses across multiple material phases [91]. In fact, such micro-elastic pulses are generated whenever a material is subjected to plastic deformation. Hence, AE sensing has long been employed in the literature to characterize various material properties such as the creep behavior [160] and strength characteristics [52, 110, 85], or major anomalies, such as wear [19] and crack propagation [152, 128]. AE sensing has also been widely employed to characterize various machining processes at micro- as well as nano-scales [57, 7].

The precision of the lithography process to probing different material phases, coupled with the high-resolution ($\sim 10^6$ Hz sampling rates) sensing capability of AE allows us to track the microstructural variations occurring at micrometer scales, as opposed to tracking the bulk properties and major anomalies. When analyzed through machine learning approaches, the transient patterns of the AE signals can reveal significant information related to the underlying microstructure [150]. In this work, we employ machine learning of the resulting acoustic emission signatures to discern between different microstructures of Ti-6Al-4V as the indenter scans the surface during a lithography process. This necessitates harnessing the high-frequency information from the measured AE so that short time-scale variations resulting from grain-boundary crossing and/or microstructural changes can be detected. We employ random forest [64], a nonparametric machine learning model to distinguish between different microstructural compositions of Ti-6Al-4V using high-frequency signatures from the measured AE signals. Results show that the present approach can identify different microstructure types with accuracies exceeding 95%.

In the sequel, we present a model interpretation approach called LIME (local interpretable model-agnostic explanations) [121] to generate physical insights into the AE features that can be used to identify novel structures (i.e., previously unseen cases) that typically go unnoticed when working with black-box machine learning approaches. We show such an instance where the explanations generated from LIME allowed us to identify a microstructural anomaly (a deep preexisting scratch mark) on the surface. The remainder of the chapter is organized as follows: Section 6.2 delineates the experimental procedure and data collection from the nanoindentation-based lithography process. Details on the implementation of the machine learning algorithm for microstructure identification are presented in Section 6.3 followed by physical insights into the machine learning algorithm using LIME analysis in Section 6.4. Concluding remarks and future works are presented in Section 6.5.

6.2 Experimental approach

The current lithography study focuses on discerning the microstructure of an additively manufactured (via EBM) Ti-6Al-4V sample surface [77] through the analysis of the AE

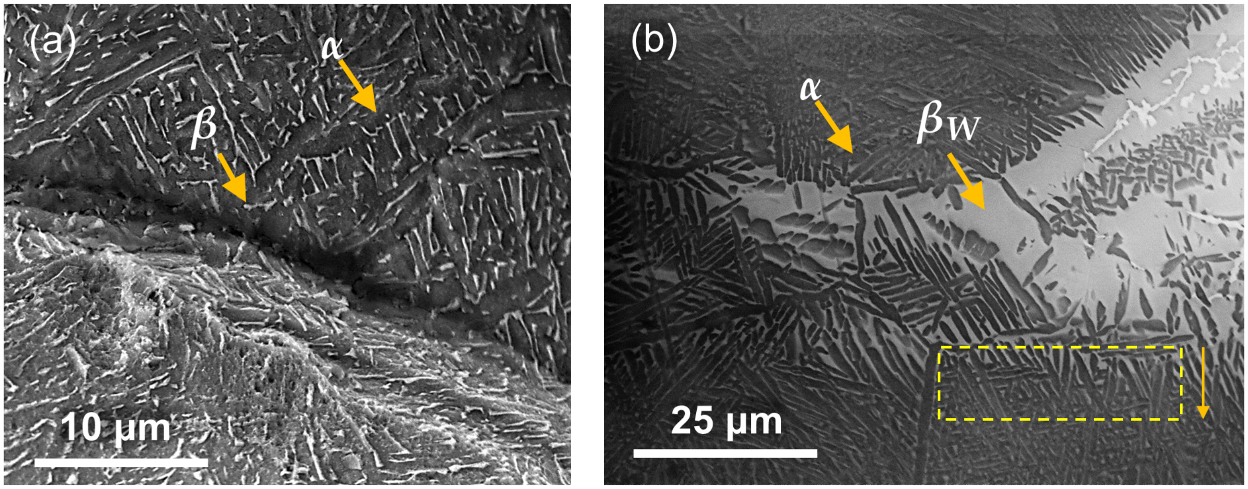

Figure 6.2: SEM images showing the representative microstructure of a Ti-6Al-4V workpiece. (a) The as-fabricated state consisting of the representative $\alpha + \beta$ colony with α lamellae (in dark) interspersed with β phase (rod-shaped, in white) of average thickness 200 nm and (b) the microstructure obtained after polishing shows extreme coarsening of the β phase at scattered locations (β_W see at arrow) and overall widening (≥ 3 μm average width).

signals generated during the lithography process. Details on the process parameters of the EBM can be found in [78]. The workpiece was polished on a Buehler Metaserv Grinder-Polisher (model 95-C2348-160) using silicon carbide (SiC) polishing pads (⌀203 mm), in stages, with progressively smaller abrasives ranging from 30 μm to 5 μm under dry conditions. A steady nominal down pressure of 0.5 kPa was maintained and the polisher speed was fixed at 500 rpm. The surface was manually subjected to a quasi-random orbital motion. The final polishing step involved the use of alumina abrasives (< 1 μm), suspended in an aqueous solution (20% by wt., pH ≈ 7.5) for 20 minutes to impart a specular finish (average surface roughness $S_a \leq 25$ nm) to the surface. The slurry was routinely flushed to avoid possible agglomeration of finer abrasives into large clusters that may result in scratching. To observe the microstructures, the mechanically polished samples were first treated with Kroll's reagent ($5 - 7\%$ nitric acid (HNO_3) and $2 - 4\%$ hydrofluoric acid (HF) and rest distilled water) for 10 s and then rinsed with distilled water.

A nanoindentation setup, Hysitron TI 950 carrying a Berkovich indenter with a diamond tip (included angle – 142.3° and tool tip radius – 100 nm) with a maximum downforce of 10,000 μN was employed for this experimental study. The testbed is mounted on a vibration isolating platform to neutralize the effect of external disturbances. The Ti-6Al-4V work piece was clamped on the Hysitron nanoindenter testbed and the AE sensor (S9225 from Physical Acoustic Corp) with an operating frequency range of 300-1800 kHz was placed on the top of the workpiece, affixed with a dental cement as shown in Figure 6.1. See [29] for further details on the experimental setup.

Figure 6.2(a) shows the microstructure of as-fabricated Ti-6Al-4V samples comprising of lamellar α (gray) phase interspersed with rod shaped β (white) phase with both colony and basket-weave morphology. We refer to this typical $\alpha + \beta$ phase as the standard microstructure in the rest of the chapter. While α phase (with hexagonal close packing structure) is more ductile and chemically inert, β phase (with body centered cubic packing) increases the strength and toughness of the material [90]. Subsequent mechanical polishing of these as-fabricated Ti-6Al-4V samples was found [78] to cause dilation of the β phase at scattered locations. This is primarily due to the high flash temperatures (in the range of 700-1000 K) coupled with extremely high cooling rates ($\sim 10^6$ K/s) at the asperity-abrasive interface. Such high flash temperatures cause migration of the β colony boundaries resulting in the apparent dilation as shown in Figure 6.2(b). We refer to this microstructure with widened β phase (β_W in Figure 6.2(b)) as the diffused microstructure and is composed of roughly 60% α and 40% β. In comparison, the as-fabricated microstructure primarily consists of ∼90% α phase with ∼10% β (see Figure 6.2(a)). We also note that in the diffused regions, α and β_W phases exist in both colony and basket-weave morphology with spearhead-like structures at the boundary (see the dotted box in Figure 6.2(b)) before merging into the standard needle-shaped β phase. These spearhead-like β_W phases represent an “intermediate” microstructure at the boundary separating the diffused and standard microstructures. Since the coarsening of the β phase occurs only at scattered locations, both standard and diffused microstructure types co-exist in the polished surface with former being the predominant one. Existence of such non-equilibrium microstructures, each influencing the mechanical behavior of the workpiece, creates a possibility to tune the hardness, fatigue strength, and other mechanical properties of additively manufactured components for specific applications [148]. For a detailed analysis of the microstructural study, please refer to [78].

Prior to performing the lithography of the polished samples, three representative locations, each (marked in Figure 6.3(a)) consisting of standard and diffused microstructures were identified (using an optical camera installed inside the Hysitron nanoindentation machine). At each location, lithography process was performed to generate five parallel scratches (marked as (i), (ii), (iii), (iv) and (v) in Figures 6.3(c& d)) each of length 15 μm. We ensured that the scratch marks are longer than the size of most of the key microstructural features, including the widths of the rod-shaped β and the diffused β_W phases. The maximum downforce of the indenter was set to 10,000 μN and the indenter speed to 0.5 μm/sec, such that each scratch lasted for 30 sec. The AE released during the process was collected using S9225 AE sensor from Physical Acoustic Corp with a sampling frequency of 500 kHz. The aforementioned lithography process was repeated at three random locations, each containing predetermined diffused and standard microstructures as depicted in Figure 6.3(a).

6.3 Results and discussions

6.3.1 AE time-frequency patterns

The AE signals acquired from the process (five parallel scratches made at three different locations) were divided into uniform 0.25 sec long segments (with each segment having 0.25 sec time segment × 500,000 samples/sec sampling rate = 125,000 data points). The 0.25 sec segment length was chosen to allow gathering the signatures of AE released from lithography over specific elementary microstructural features. Altogether, we have 600 such signal segments (30 sec × (1/0.25 sec) × 5) from each class of microstructure from each of the three locations. Representative time portraits of AE gathered during lithography of the surface with standard and diffused microstructures are shown in Figures 6.4(a) and 6.4(d) respec-

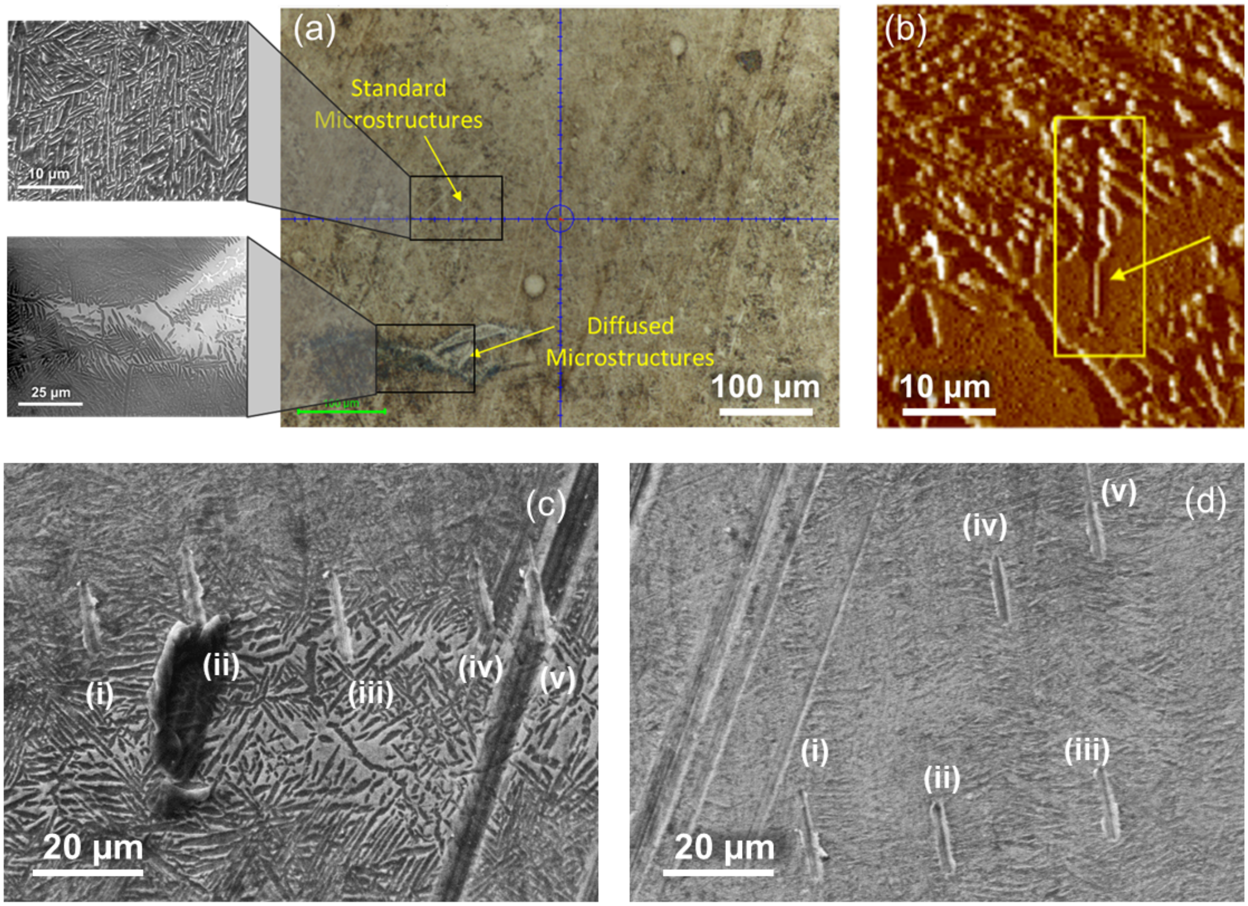

Figure 6.3: (a) Micrograph showing the standard and diffused microstructures as the scratch test was performed. Insets show the scanning electron micrographs of the standard and the diffused microstructure. (b) The scratch generated during the lithography procedure, (c) and (d) respectively are the SEM images of the diffused and standard microstructure regions indicating the 5 scratch marks generated during the lithography process.

tively. Little meaningful changes in the AE patterns are evident from visual examination of the time portraits. This is because the elastic energy released during the lithography process is transmitted in the form of nonstationary AE signals, similar to plucking the strings of a guitar. The signals are aperiodic and are randomly interspersed with multiple bursts and quiet zones that are hard to quantify using conventional statistical descriptors.

It may be noted that the frequency spectrum of the measured AE signals captures the effect of the microstructure on the microdynamics, comprising the various deformation mechanisms, of a lithography process [116]. We, therefore, employed the AE spectral content (signal energy) over various frequency bands as the features to discern between the two classes of the microstructure. Representative spectrum of the acoustic emission signal (Figure 6.4(b) and 6.4(e)) as well as the corresponding envelope spectrum (Figure 6.4(c) and 6.4(f)) show continuous frequency spectrum with a few dominant frequency bands, distinct harmonic distortions in the form of shifts in the dominant frequency modes as well as the emergence of some new modes in the frequency spectrum between standard and the diffused microstructures. However, no systematic changes in the pattern were evident. We, therefore, employed a machine learning algorithm known as random forest [64] to perform the classification task by learning from the frequency spectrum.

6.3.2 Learning AE features for microstructural identification

Random forest is a class of ensemble learning methods based on combining multiple decision trees using bootstrapped (sampling with replacement) training samples. Bootstrapping

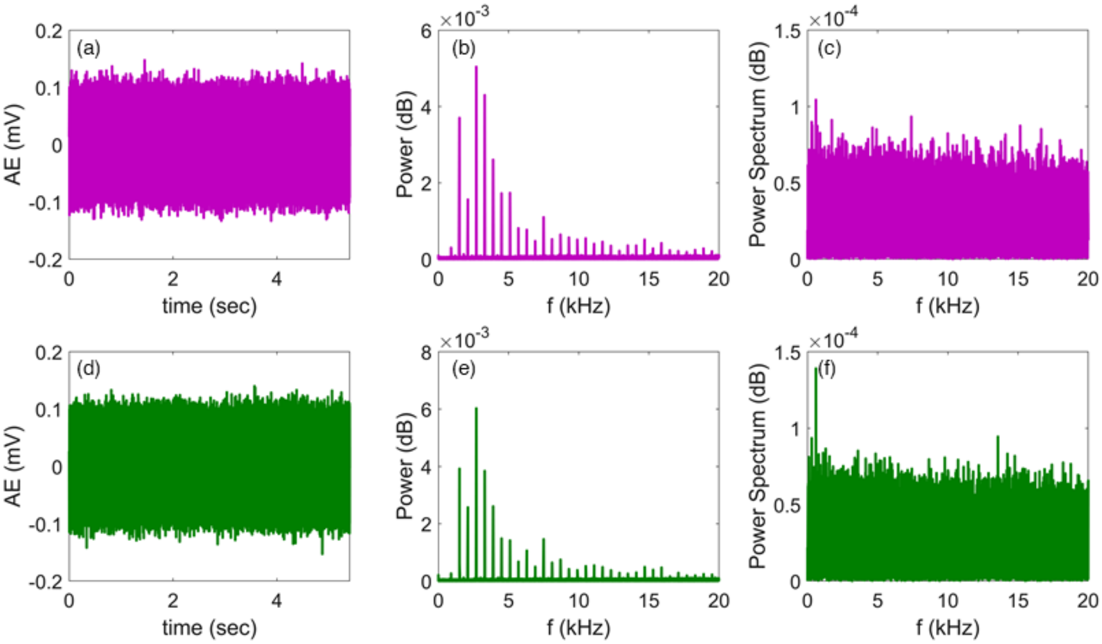

Figure 6.4: Top ((a), (b), (c)) and bottom ((d), (e), (f)) rows show the Time-domain of the AE signal, frequency spectrum, and the envelope spectrum corresponding to the standard and diffused microstructures.

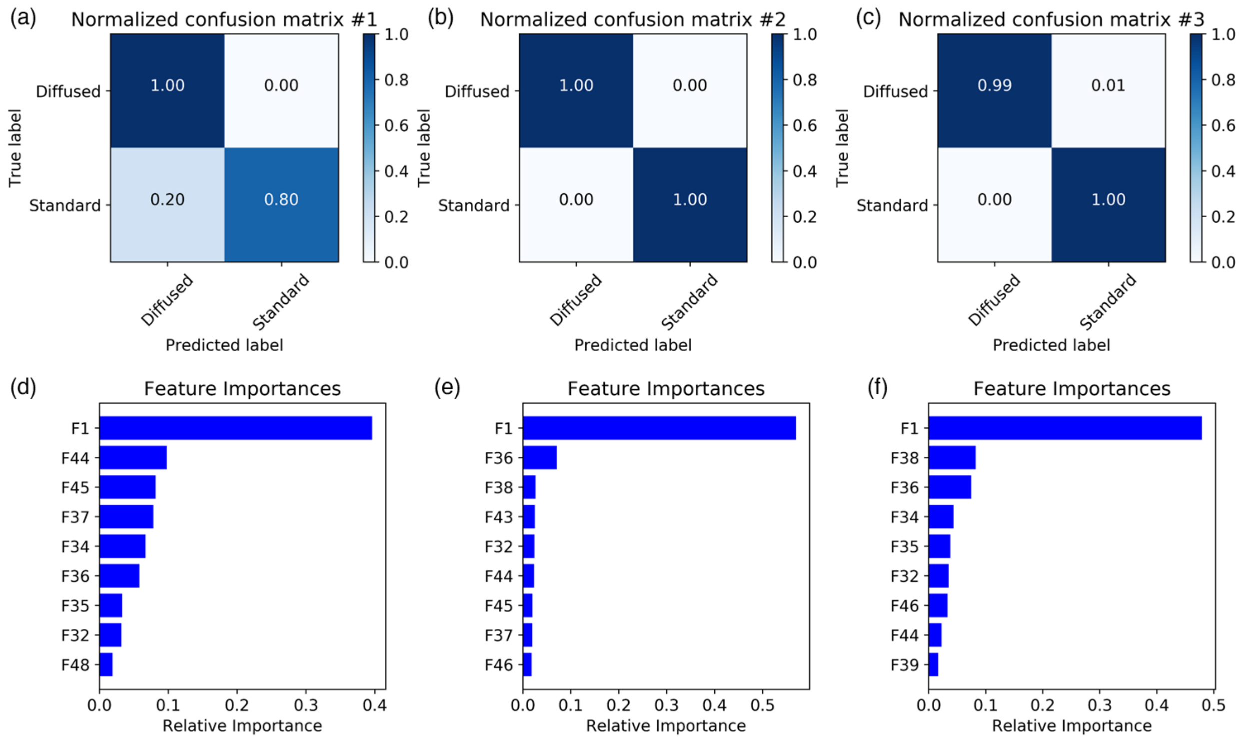

Figure 6.5: (a-c) Confusion matrix for the prediction results from the random forest model and (d-f) shows the most dominant features in each of the cases shown in figures (a-c).

reduces the overall variance, avoids overfitting and improves the prediction accuracy. Although various ensemble strategies exist, random forest models are particularly attractive because it randomizes the feature set at every stage of the binary decision making. This is beneficial as it decorrelates the trees and therefore their respective decisions unlike other ensemble methods such as bagging where most of the bagged trees look very similar to each other. Finally, the decision is made on the majority voting. Bootstrapping also enables out of bag error estimation in random forest, therefore, eliminating the need for any external cross-validation. However, random forest behaves more like a black-box due to its ensemble nature. Nonetheless, by employing the node impurity (also known as Gini index) defined as $\hat{p}_{mk}(1-\hat{p}_{mk})$, where $\hat{p}_{mk}$ is the proportion of observations in node m that belong to class k, random forest allows us to determine the importance measure for each of the features considered.

Being nonparametric, random forest does not make any distributional assumptions about the data and offers a powerful approach to perform classification and prediction tasks. To perform the classification, we first partitioned the frequency spectrum extracted from each of the 1200 segments (600 each from diffused and standard microstructure type) into 50 uniform bands of 5 kHz width (over the Nyquist range of 0-250 kHz). The signal energies from each of these bands were used as the features representing the AE signature from each signal segment. We trained the random forest model on the AE features extracted from two out of the three locations where lithography was performed and tested on the remaining one. Figures 6.5(a-c) summarize the results from the random forest models in the form of a confusion matrix. A confusion matrix specifies the performance of the classification method in terms of the number of instances in the predicted class versus the instances in the true class. In all the three cases, the model is able to predict the true microstructure type with an average accuracy of 96.33% with almost perfect sensitivity (or false negative rate of 0.003) and specificity (or false positive rate of 0.066) for detecting the diffused microstructures. This suggests that the AE response bears information to discern the differences in the work hardening and plastic deformation characteristics between different microstructural features (e.g., standard and diffused) as the indenter traverses the surface. We also compare the performance of the random forest with other standard classifiers such as linear discriminant analysis, support vector machine, and logistic regression. The corresponding classification accuracies were 87.50%, 91.75%, and 90.83%. We note that the performance of random forests is still better as compared to the aforementioned algorithms, particularly because of the ensemble nature of random forests, i.e., it leverages multiple decision trees, that may not have high accuracies themselves, but together as an ensemble offers a very accurate and consistent model.

Figures 6.5(d-f) delineate the 10 most important variables (ranked in terms of the Gini index) identified by the random forest model. We note that feature F1, capturing the signal content over the 0-5 kHz band is consistently ranked as the most important feature. We further refined the 0-5 kHz band of F1 into 250 frequency bands, each 20 Hz-wide, and included the signal energies over these frequency bands as additional features (labeled F1:1, F1:2, …, F1:250) to predict the microstructure. It was determined from this study that the DC component (zero frequency component) of the signal is the primary determinant of the classification accuracy of the model. From the lithography process standpoint, the DC component of the AE signal is related to the mechanical properties engendered by the microstructure, such as the strength and hardness.

Apart from the DC component, several low and high-frequency components were ranked among the top ten important features. These frequencies resonate with the microdynamics of the lithography process [97]. To explore these frequency features, we re-trained our model, however, this time excluding the DC component. The average prediction accuracy for this model is 65.83%. Although the new model has relatively lower accuracy, it suggests that the information related to the dynamics of the lithography process is mostly concentrated in the 30-50 kHz and 0.3-1 kHz frequency bands. Although the random forest model was able to identify these frequency bands as important features, it does not provide insights into how the feature characteristics vary between the two classes of microstructures. This information is useful for deriving physical relationships connecting the AE features with the microstructure.

6.4 Physical insights into AE features

As machine learning models get more and more predictive e.g., random forest, neural networks, they become more sophisticated to a point where they serve as mere black-boxes, thereby, significantly reducing their interpretability, i.e., why certain decisions/predictions are made. In this work, we utilize LIME model to interpret the influence of the important AE features on the prediction results. The approach is based on tracking the black-box (in this case, random forest) model's predictions on slightly perturbed datasets [121]. Once the model predictions on perturbed datasets are obtained, LIME trains an interpretable model that offers a good approximation to the black-box model's prediction locally. In this fashion,

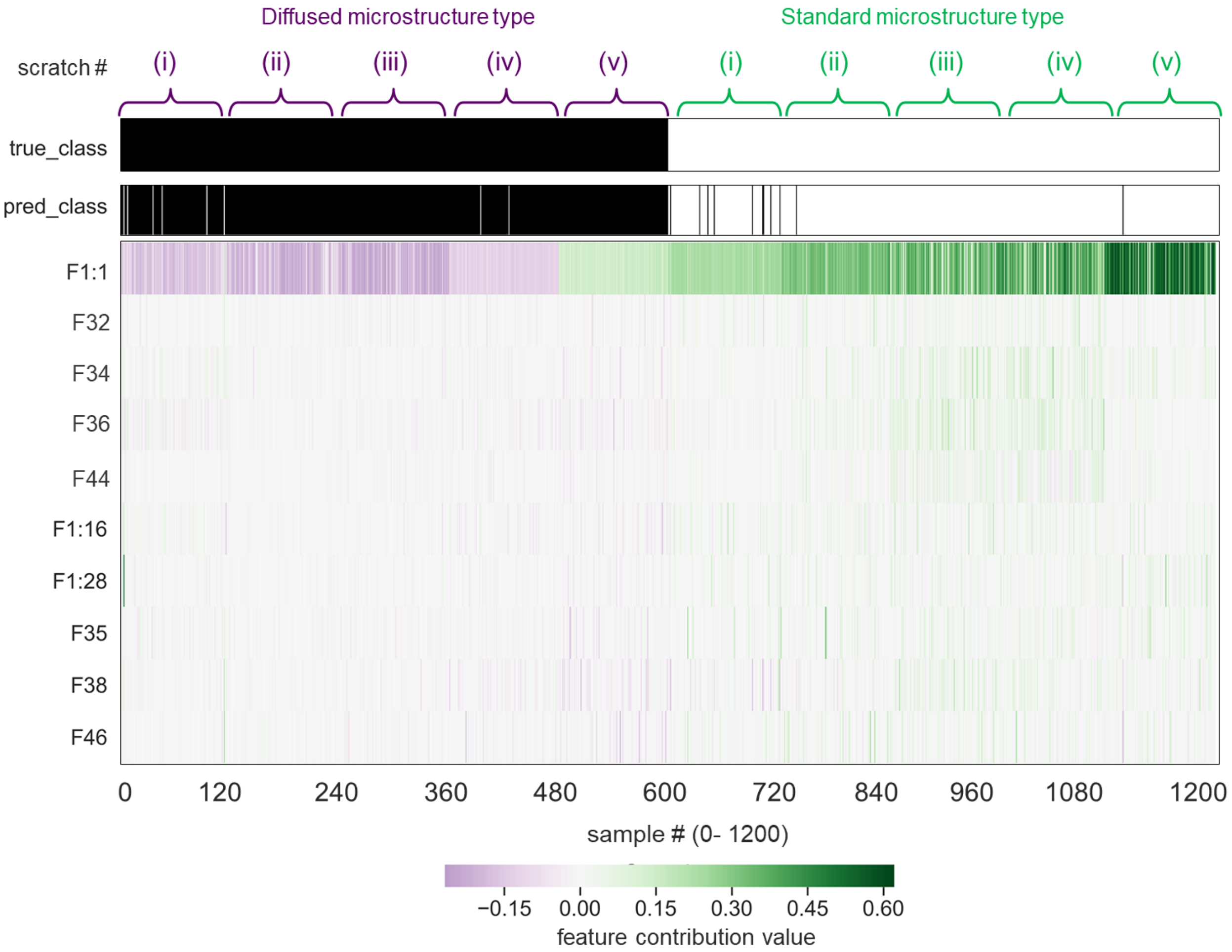

Figure 6.6: Analysis from LIME. The top two rows of the heat map representing the true class (true_class) and the predicted class (pred_class) of the microstructures of each of the 1200 samples or columns shown across the x-axis. The samples are laid out as scratches (i)-(v) of diffused followed by scratches (i)-(v) of the standard microstructure. Here we refer to diffused as "0" (in black) and standard microstructure as "1" (in white). Rows 3-12 are the values of most important features as inferred by the LIME algorithm. The values indicated by the colormap are the contributions from each of the features towards classifying the samples as diffused or standard (see Appendix for more details).

LIME generates low fidelity but interpretable, local surrogate models, $g(x, y) \in G$ where G is the space of all possible explanatory models such that it minimizes the penalized likelihood function given as:

$$\epsilon(x) = \arg\min_{g \in G} \mathcal{L}(f(x), g(x), x) + \omega(g(x))$$

where $f(.)$ is the random forest model, and $\omega(g(.))$ is the penalty on the complexity of the low fidelity model $g(x)$ defined a priori. Although, the low fidelity models are generally linear and only locally optimal, the explanations generated by the model allow us to understand the behavior of the most important features. The result of the LIME analysis on the random forest model built with the extended AE features (i.e., F1:1 through F1:250, and F2 through F50) is summarized in Figure 6.6. It captures the contribution (roughly, the weight) of each of the top ten most important features towards predicting the microstructure class of every one of the 1200 data samples. The first 600 data samples (AE segments and the resulting features) were extracted during the lithography, i.e., five 15 μm long scratches made over the diffused microstructures (shown in dark/purple in the top row of the figure), and the remaining 600 data samples were extracted during the lithography over standard microstructures (shown in white in the top row of the figure). The random forest model predictions for each of these 1200 samples are provided in the second row. Evidently, 592 out of 600 AE data samples from the lithography over diffused microstructure, and 589 out of 600 AE samples from the lithography over standard microstructure were correctly identified, indicating the predictive power of the AE features. For each subsequent row, the color and the intensity capture the contribution (positive vs. negative, and the extent, respectively) of each of the top ten features towards predicting the microstructure for the specific data sample. Clearly, we note a strong contrast in the feature contribution values between the left and the right half of the samples, and that the feature F1:1 stands out as the most discriminating feature which is consistent with the random forest result.

More importantly, Figure 6.6 points to an intriguing observation. Within the diffused microstructure region, we note that the contribution values of feature F1:1 corresponding to the samples in scratch (v) is significantly different from the feature contribution values of rest of the samples. This can be visualized from Figure 6.7 that shows the feature contribution values of F1:1 segregated into scratches (i)-(iv) and scratch (v) within the diffused microstructure region and scratches (i)-(v) within the standard microstructure region. Clearly, the samples

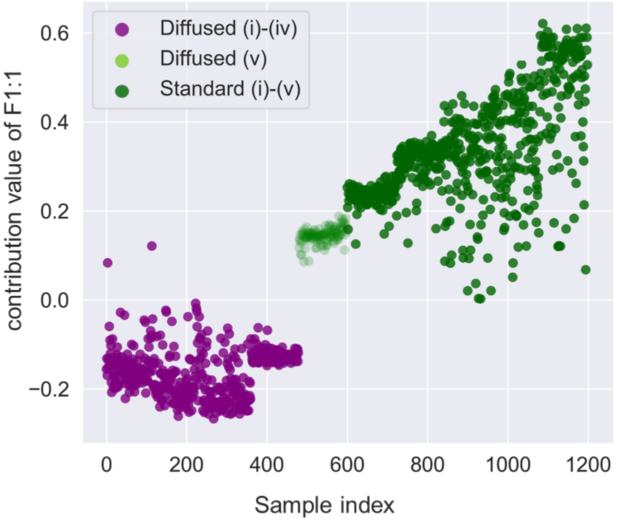

Figure 6.7: Feature contribution of F1:1 categorized into scratches (i)-(iv) (in purple) and scratch (v) (in light green) within the diffused microstructure region followed by scratches (i)-(v) (in dark green) within the standard microstructure region.

in scratch (v) within the diffused microstructure (denoted by light green) are distinctly different from the rest of the samples within the diffused microstructure region (denoted by purple color). Surprisingly, the feature contribution values of these samples are apparently closer to that of the standard microstructures. To explore the root cause of this peculiar pattern, we refer to the SEM images of the scratches generated during the lithography process. On the SEM image of the scratches in Figures 6.3(c), we note that scratch (v) within the diffused microstructure region traverses through a *deep, preexisting scratch mark* on the surface. As feature F1:1 corresponds to the DC component of the AE signals, it represents the underlying forces experienced by the moving indenter. From the packing structure of α and β phases, we know that the diffused β phase is harder than the standard $\alpha + \beta$ phase. Therefore, the indenter experiences relatively less force when traversing through the standard microstructure. Since the feature contribution values of F1:1 for scratch (v) within the diffused microstructure region are similar to that of the standard microstructures suggest that the indenter experiences less force while traversing through this scratch. This can potentially be justified if we consider the effect of the preexisting scratch. As the indenter operates under fixed downforce, presence of the preexisting scratch (or other similar microstructural defects) is likely to decrease the drag force on the indenter and therefore result in the observed anomaly.

Such novel patterns and anomalies typically go unnoticed when working with black-box machine learning models. By investigating the feature explanations generated from the LIME approach, we identified a microstructural anomaly in the form of a deep, preexisting scratch mark. This is interesting as it opens an exciting opportunity to not only rapidly characterize the known microstructure types, but also identify novel phases and microstructures, especially when studying the effects of different processing pathways and process parameters on the resulting structure [117].

6.5 Summary and conclusions

In closing, this chapter presents a machine learning approach to enable rapid characterization of microstructures by tracking the AE signatures from a scanning probe lithography process. Current approaches for characterizing microstructures involve a battery of manual experimentation and remains a critical bottleneck in the process of autonomous materials discovery. In this direction, we conducted lithography experiments on the surface of a Ti-6Al-4V workpiece fabricated via EBM process and subsequently subjected to mechanical polishing such that the microstructure composition was locally altered. We analyzed the AE signals gathered from the lithography experiments to distinguish between the locally diffused and the standard microstructure types. The results from random forest modeling suggest that the AE signatures can capture the changes in the microstructure with over 95% accuracy, therefore, offering a novel route to rapidly characterize the microstructure. More interestingly, our analysis also showed that there are two prominent frequency ranges, 0.3-1 kHz and 30-50 kHz that capture most of the dynamics of the lithography process. Existing research [26, 97] on the AE signatures of the machining processes reveals that these high frequencies are closely related to the elastic and plastic deformations, movement of dislocations as well as mild adhesive wear. In contrast, no conclusive evidence for the sources of low frequencies exists in the literature and remains an open area of research.

The results presented in this work are significant as the changes (scratches) occurring in such processes operate under microscopic forces ($< 10,000\ \mu$N) and are difficult to track/capture by many conventional and state-of-the-art instrumentation and monitoring methods. Beyond establishing that AE can be used to rapidly track the changes in the microstructures, we showed that the AE signatures contain potentially useful information that can aid in the exploration of novel structures, defects, and anomalies.

Although the current study is based on the microstructure classification of a given material system, the method is material agnostic and can be potentially useful for on the fly detection of different microstructure types, especially when developing new materials and identifying the presence of microscopic defects on the surface. Our current and future efforts are focused on developing an efficient mapping of AE signals with the microstructural composition (e.g., as obtained from SEM images) and employ these as part of the smart hybrid manufacturing platform for identifying microstructures of the various materials systems created during the process. We will also explore features based on envelope spectrum and cepstrum analysis to enrich our feature set for identifying novel microstructure phases, that are typically difficult to identify using standard spectrum-based features.

7. SUMMARY AND FUTURE WORKS

7.1 Summary

While there is a deluge of data, current smart manufacturing practices harness less than 25% of the data generated during advanced manufacturing processes. Lack of robust data representation and quantification methods impede the efficient utilization of data in advanced manufacturing processes. In this direction, this dissertation focused on developing statistical and data-driven models for representation and quantification of advanced manufacturing processes to realize rapid characterization. Most pertinently, we focus on additive manufacturing processes and the challenges therein, such as poor surface morphology and porosity.

Towards this, chapter 2 presented the challenges pertaining to surface quality and porosity issues in additive manufacturing and motivated the need to develop efficient techniques to finish the surface morphology of additively manufactured components via post-processing methods. We compared the two most commonly employed post-processing methods: machining and fine-abrasive finishing. Results showed that machining improved the average surface roughness 98.1% and increased surface hardness by 37%. In the case of fine-abrasive finishing, the average surface roughness improved by 99.82%, and microhardness increased by 11% (with significantly more efficacy on z-build-direction surfaces). We found that abrasive finishing reduced the fraction of voids by almost 99.81%, thus providing an effective means to enhance the bearing capacity of AM components. While this study demonstrated a multi-step finishing process to improve the surface morphology of AM components, different applications call for different surface finish requirements. Therefore, controlling the surface quality creates a need to investigate the phenomenology of surface modification during the post-processing stages and develop accurate modeling approaches to achieve the desired specifications. Chapter 3 of this dissertation showed that the exact phenomenology of surface smoothening involves asperity-abrasive contacts that exhibit viscous behavior. Here, the asperity material flows in the form of thin (1 - 10 μm) fluid-like layers. Subsequent bridging of these layers among neighboring asperities results in surface smoothening.

With the physical understanding of the surface smoothening process, we now return to the original question of rapid characterization. In Chapter 4, we leverage the physics of the finishing process to develop a copula-based random planar graph representation of the surface morphology evolution gathered from *in situ* images. Via theoretical and experimental studies, we showed that the graph spectrum served as efficient identifiers for endpoints, i.e., deciding when to stop the polishing, almost an order of magnitude faster as compared to traditional methods. We also showed that these representations are robust and efficient in capturing the surface morphological changes as compared to standard surface roughness measures. Along similar lines, another issue that we investigated was that of defect characterization. Chapter 5 presented an unsupervised image segmentation approach, with statistical consistency, by iteratively identifying the optimal graph cut and learning the parameters of the graph cut via maximum *a posteriori* estimation. Investigations into defect segmentation in noisy AM images and brain MR scans demonstrated more than 90% improvement in the segmentation performance as compared to state-of-the-art unsupervised methods.

Chapters 4 and 5 presented two different instances where analytical methods, particularly graph-based methods, emerged as promising tools for characterizing advanced manufacturing processes. We further extend this idea for the rapid characterization of the microstructures of additive manufactured components. Chapter 6 presents a machine learning approach to enable the rapid characterization of microstructures by tracking the acoustic emission signatures from a scanning probe lithography process. The results from machine learning modeling suggest that the AE signatures can capture microstructural change with over 95% accuracy, therefore offering a novel route to characterize the microstructure rapidly. More interestingly, our analysis also sheds light on the physical interpretation of the machine learning models. In particular, our study showed that there are two prominent frequency ranges, 0.3-1 kHz and 30-50 kHz, that capture most of the dynamics of the lithography process.

7.2 Future works

Rapid characterization is emerging as one of the critical areas of research in smart manufacturing and is becoming crucial for accelerating materials discovery. Current characterization techniques are so slow and cumbersome that they create a bottleneck in the process of autonomous materials discovery, qualification, and inspection. The potential to synergistically characterize as-you-make could benefit the emerging paradigm of materials-on-demand manufacturing–where the material properties, processing parameters, and geometric and structural characteristics can be optimally generated to meet the desired functionality.

Efforts are underway to implement materials-on-demand manufacturing as a part of our existing HM platform and demonstrate its potential in discovering materials with novel and superior characteristics. Chapter 6 of this dissertation laid the foundation for *in situ* characterization of bulk phase fractions of microstructures in titanium alloys. The authors would like to extend this work from identifying bulk phase fraction analysis on the material surface to detect change points or phase boundaries in microstructures with signals obtained during micro-milling experiments. Micro-mill cutting has the ability to traverse across different microstructure as the tip of the tool is at the same length scale of the microstructures found in stainless steel, providing a means for rapid characterization of materials using a hybrid machine.

From modeling and theoretical standpoint, significant opportunities exist. For instance, the methodology for consistent estimation of the max-flow may be extended for colored images and three-dimensional objects. These are particularly attractive for applications in medical imaging, e.g., CT scans. In addition to this, a more comprehensive Bayesian model to simultaneously estimate the parameters used in the MRF prior can be investigated.

A critical question that arises from this research is the need to reduce experimental efforts during the upstream advanced manufacturing processes. It holds the potential to accelerate the experimentation process and enable rapid characterization. Towards this, future research directions will explore active learning approaches to search for optimal process conditions while minimizing experimental costs. Venues for theoretical studies also exist in the active learning literature as theoretical guarantees remain limited, for example, in the presence of uncertainty (i.e., agnostic active learning) when strict improvements are not guaranteed. Under such circumstances, we may seek Probably Approximately Correct (PAC) learning models that offer theoretical guarantees on the generalization error with a very high probability.

REFERENCES

[1] (2015). *ASTM International. ISO/ASTM52900-15 Standard Terminology for Additive Manufacturing.* West Conshohocken, PA.

[2] A. S. Iquebal, Botcha, B., Panda, I., and Bukkapatnam, S. T. S. (2019a). Modeling the defect morphology in additive manufacturing processes using a Bayesian knot-free spline representation. *To be submitted to IISE Transactions.*

[3] A. S. Iquebal, Cline, D., and Bukkapatnam, S. T. S. (2019b). Planar graph representation of surface morphology: A copula-based approach for modeling spatial random fields. *To be submitted to Technometrics.*

[4] A. S. Iquebal, Pandagare, S., and Bukkapatnam, S. T. S. (2019c). Learning acoustic emission signatures from a nanoindentation-based lithography process: Towards rapid microstructure characterization. *Tribology International*, 143:106074.

[5] Aghan, R. and Samuels, L. E. (1970). Mechanisms of abrasive polishing. *Wear*, 16(4):293–301.

[6] Agrawal, A. and Choudhary, A. (2016). Perspective: Materials informatics and big data: Realization of the "fourth paradigm" of science in materials science. *APL Materials*, 4:053208.

[7] Ahn, B. and Lee, S. (2009). Characterization and acoustic emission monitoring of AFM nanomachining. *Journal of Micromechanics and Microengineering*, 19(4):045028.

[8] Akagaki, T. and Kato, K. (1988). Simulation of flow wear in boundary lubrication using a Vickers identation method. *Tribology Transactions*, 31(3):311–316.

[9] Akula, S. and Karunakaran, K. P. (2006). Hybrid adaptive layer manufacturing: An intelligent art of direct metal rapid tooling process. *Robotics and Computer-Integrated Manufacturing*, 22(2):113–123.

[10] Alberi, K., Nardelli, M. B., Zakutayev, A., Mitas, L., Curtarolo, S., Jain, A., Fornari, M., Marzari, N., Takeuchi, I., Green, M. L., et al. (2018). The 2019 materials by design

roadmap. *Journal of Physics D: Applied Physics*, 52:013001.

[11] Amine, T. A., Sparks, T. E., and Liou, F. (2011). A strategy for fabricating complex structures via a hybrid manufacturing process. In *22nd Annual International Solid Freeform Fabrication Symposium - An Additive Manufacturing Conference*, pages 175–184.

[12] Andreev, E. M. (1970). On convex polyhedra in Lobačevskiĭ spaces. *Mathematics of the USSR-Sbornik*, 10(3):413.

[13] Appleton, B. and Talbot, H. (2006). Globally minimal surfaces by continuous maximal flows. *IEEE Transactions on Pattern Analysis and Machine Intelligence*, 28(1):106–118.

[14] Arbelaez, P., Maire, M., Fowlkes, C., and Malik, J. (2011). Contour detection and hierarchical image segmentation. *IEEE Transactions on Pattern Analysis and Machine Intelligence*, 33(5):898–916.

[15] Archard, J. F. (1985). Mechanical polishing of metals: A scientific argument of long standing. *Physics Bulletin*, 36(5):212.

[16] Ashby, M. and Frost, H. (1982). *Deformation-Mechanism Maps: The Plasticity and Creep of Metals and Ceramics*. Pergamon Press, Oxford.

[17] Aspuru-Guzik, A. and Persson, K. (2018). Materials acceleration platform: Accelerating advanced energy materials discovery by integrating high-throughput methods and artificial intelligence. Technical report.

[18] Attar, H., Calin, M., Zhang, L., Scudino, S., and Eckert, J. (2014). Manufacture by selective laser melting and mechanical behavior of commercially pure Titanium. *Materials Science and Engineering A*, 593:170–177.

[19] Baccar, D. and Söffker, D. (2015). Wear detection by means of wavelet-based acoustic emission analysis. *Mechanical Systems and Signal Processing*, 60:198–207.

[20] Bae, E., Yuan, J., and Tai, X.-C. (2011). Global minimization for continuous multiphase partitioning problems using a dual approach. *International Journal of Computer Vision*, 92(1):112–129.

[21] Balla, V. K., Bhat, A., Bose, S., and Bandyopadhyay, A. (2012). Laser processed TiN

reinforced Ti6Al4V composite coatings. *Journal of the Mechanical Behavior of Biomedical Materials*, 6:9–20.

[22] Bárdossy, A. and Li, J. (2008). Geostatistical interpolation using copulas. *Water Resources Research*, 44(7).

[23] Barron, A., Schervish, M. J., Wasserman, L., et al. (1999). The consistency of posterior distributions in nonparametric problems. *The Annals of Statistics*, 27(2):536–561.

[24] Beilby, G. (1921). *Aggregation and Flow of Solids*. Macmillan, London.

[25] Besag, J. (1974). Spatial interaction and the statistical analysis of lattice systems. *Journal of the Royal Statistical Society: Series B (Statistical Methodology)*, pages 192–236.

[26] Bhuiyan, M., Choudhury, I. A., Dahari, M., Nukman, Y., and Dawal, S. (2016). Application of acoustic emission sensor to investigate the frequency of tool wear and plastic deformation in tool condition monitoring. *Measurement*, 92:208–217.

[27] Bhushan, B. (1998). *Handbook of Micro/Nano Tribology*. CRC press, Boca Raton.

[28] Blok, H. (1937). Theoretical study of temperature rise at surfaces of actual contact under oiliness lubricating conditions. In *Proceedings of the Institute of Mechanical Engineers: General Discussion on Lubrication and Lubricants*, volume 2, pages 222–235. London: IMechE.

[29] Botcha, B., Wang, Z., Rajan, S., Gautam, N., Bukkapatnam, S. T., Manthanwar, A., Scott, M., Schneider, D., and Korambath, P. (2018). Implementing the transformation of discrete part manufacturing systems into smart manufacturing platforms. In *ASME 2018 13th International Manufacturing Science and Engineering Conference*, pages V003T02A009–V003T02A009. ASME.

[30] Bowden, F. P. and Hughes, T. P. (1937). Physical properties of surfaces. iv. polishing, surface flow and the formation of the beilby layer. *Proceedings of the Royal Society of London A: Mathematical, Physical and Engineering Sciences*, 160(903):575–587.

[31] Box, G. E. and Cox, D. R. (1964). An analysis of transformations. *Journal of the Royal*

Statistical Society: Series B (Methodological), 26(2):211–243.

[32] Boyd, S. and Vandenberghe, L. (2004). *Convex Optimization*. Cambridge University Press, Cambridge.

[33] Boykov and Kolmogorov (2003). Computing geodesics and minimal surfaces via graph cuts. In *Proceedings of 9th IEEE International Conference on Computer Vision (ICCV)*, pages 26–33 vol.1.

[34] Boykov, Y., Veksler, O., and Zabih, R. (1998). Markov random fields with efficient approximations. In *1998 IEEE Computer Society Conference on Computer Vision and Pattern Recognition*, pages 648–655. IEEE.

[35] Bridgman, P. W. (1952). *Studies in Large Plastic Flow and Fracture: Emphasis on the Effects of Hydrostatic Pressure*. McGraw-Hill, New York.

[36] Brøtan, V. and Bovie, K. (2012). The hybrid manufacturing cell: Determining key parameters in the integration of powder bed fusion with high speed milling. In *2012 IEEE International Conference on Industrial Engineering and Engineering Management*, pages 583–587. IEEE.

[37] Bui, A. T. and Apley, D. W. (2018). A monitoring and diagnostic approach for stochastic textured surfaces. *Technometrics*, 60(1):1–13.

[38] Bukkapatnam, S., Rao, P., and Komanduri, R. (2008). Experimental dynamics characterization and monitoring of MRR in oxide chemical mechanical planarization (CMP) process. *International Journal of Machine Tools and Manufacture*, 48(12-13):1375–1386.

[39] Bukkapatnam, S. T. S., Iquebal, A. S., and Kumara, S. R. T. (2018). Planar random graph representations of spatiotemporal surface morphology: Application to finishing of 3D printed components. *CIRP Annals*, 67(1):495–498.

[40] Bulsara, V. H., Ahn, Y., Chandrasekar, S., and Farris, T. (1998). Mechanics of polishing. *Journal of Applied Mechanics*, 65(2):410–416.

[41] Campanelli, S., Contuzzi, N., Ludovico, A., Caiazzo, F., Cardaropoli, F., and Sergi, V. (2014). Manufacturing and characterization of Ti6Al4V lattice components manufactured

by selective laser melting. *Materials*, 7(6):4803–4822.

[42] Carslaw, H. S. and Jaeger, J. C. (1959). *Conduction of Heat in Solids*. Clarendon Press, Oxford.

[43] Carson, C., Belongie, S., Greenspan, H., and Malik, J. (2002). Blobworld: Image segmentation using expectation-maximization and its application to image querying. *IEEE Transactions on Pattern Analysis and Machine Intelligence*, 24(8):1026–1038.

[44] Challen, J. M., McLean, L. J., and Oxley, P. L. B. (1984). Plastic deformation of a metal surface in sliding contact with a hard wedge: Its relation to friction and wear. *Proceedings of the Royal Society of London A: Mathematical, Physical and Engineering Sciences*, 394(1806):161–181.

[45] Chan, T. F., Esedoglu, S., and Nikolova, M. (2006). Algorithms for finding global minimizers of image segmentation and denoising models. *SIAM Journal On Applied Mathematics*, 66(5):1632–1648.

[46] Chang, D.-C. and Bukkapatnam, S. (2004). Towards characterizing the microdynamics of AE generation in machining. *Machining Science and Technology*, 8:235–261.

[47] Chen, G., Jiang, K., Zhang, L., Bezold, A., Weichert, D., and Broeckmann, C. (2019). A Bayesian statistics based investigation of binder hardening's influence on the effective strength of particulate reinforced metal matrix composites (PRMMC). *International Journal of Mechanical Sciences*, 159:151–164.

[48] Chen, L.-Q., Chen, L.-D., Kalinin, S. V., Klimeck, G., Kumar, S. K., Neugebauer, J., and Terasaki, I. (2015). Design and discovery of materials guided by theory and computation. *npj Computational Materials*, 1:15007.

[49] Comaniciu, D. and Meer, P. (2002). Mean shift: A robust approach toward feature space analysis. *IEEE Transactions on Pattern Analysis and Machine Intelligence*, 24(5):603–619.

[50] Connelly, R., Gortler, S. J., Solomonides, E., and Yampolskaya, M. (2019). The isostatic conjecture. *Discrete & Computational Geometry*, pages 1–25.

[51] Cour, T., Benezit, F., and Shi, J. (2005). Spectral segmentation with multiscale graph

decomposition. In *2005 IEEE Computer Society Conference on Computer Vision and Pattern Recognition (CVPR'05)*, volume 2, pages 1124–1131. IEEE.

[52] De Bono, D. M., London, T., Baker, M., and Whiting, M. J. (2017). A robust inverse analysis method to estimate the local tensile properties of heterogeneous materials from nano-indentation data. *International Journal of Mechanical Sciences*, 123:162–176.

[53] De Oliveira, V., Kedem, B., and Short, D. A. (1997). Bayesian prediction of transformed Gaussian random fields. *Journal of the American Statistical Association*, 92(440):1422–1433.

[54] Dekking, F. M., Kraaikamp, C., Lopuhaä, H. P., and Meester, L. E. (2005). *A Modern Introduction to Probability and Statistics: Understanding Why and How.* Springer Science & Business Media.

[55] Derin, H. and Elliott, H. (1987). Modeling and segmentation of noisy and textured images using Gibbs random fields. *IEEE Transactions on Pattern Analysis and Machine Intelligence*, 9(1):39–55.

[56] Ding, Y. and Bukkapatnam, S. T. (2015). Challenges and needs for automating nano image processing for material characterization. In *Nanoengineering: Fabrication, Properties, Optics, and Devices XII*, volume 9556, page 95560Z. International Society for Optics and Photonics.

[57] Dornfeld, D. and Kannatey-Asibu, E. (1980). Acoustic emission during orthogonal metal cutting. *International Journal of Mechanical Sciences*, 22:285–296.

[58] Dragoni, D., Daff, T. D., Csányi, G., and Marzari, N. (2018). Achieving DFT accuracy with a machine-learning interatomic potential: Thermomechanics and defects in bcc ferromagnetic iron. *Physical Review Materials*, 2:013808.

[59] El-Amri, I., Iquebal, A. S., Srinivasa, A., and Bukkapatnam, S. (2018). Localized magnetic fluid finishing of freeform surfaces using electropermanent magnets and magnetic concentration. *Journal of Manufacturing Processes*, 34:802–808.

[60] Fang, Z. Z., Sun, P., and Wang, H. (2012). Hydrogen sintering of titanium to produce

high density fine grain titanium alloys. *Advanced Engineering Materials*, 14(6):383–387.

[61] Farayibi, P., Abioye, T., Murray, J., Kinnell, P., and Clare, A. (2015). Surface improvement of laser clad Ti–6Al–4V using plain waterjet and pulsed electron beam irradiation. *Journal of Materials Processing Technology*, 218:1–11.

[62] Franco, B., Ma, J., Loveall, B., Tapia, G., Karayagiz, K., Liu, J., Elwany, A., Arroyave, R., and Karaman, I. (2017). A sensory material approach for reducing variability in additively manufactured metal parts. *Scientific Reports*, 7(1):3604.

[63] Freedman, D. A. (1965). On the asymptotic behavior of bayes estimates in the discrete case ii. *The Annals of Mathematical Statistics*, 36(2):454–456.

[64] Friedman, J., Hastie, T., and Tibshirani, R. (2001). *The elements of statistical learning*, volume 1. Springer.

[65] Geman, S. and Geman, D. (1984). Stochastic relaxation, Gibbs distributions, and the Bayesian restoration of images. *IEEE Transactions on Pattern Analysis and Machine Intelligence*, (6):721–741.

[66] Geweke, J. (1989). Bayesian inference in econometric models using Monte Carlo integration. *Econometrica: Journal of the Econometric Society*, pages 1317–1339.

[67] Grimmett, G. R. (1973). A theorem about random fields. *Bulletin of the London Mathematical Society*, 5(1):81–84.

[68] He, Q., Huang, T., Shuai, L., Zhang, Y., Wu, G., Huang, X., and Jensen, D. J. (2018). In-situ investigation of the evolution of annealing twins in high purity aluminium. *Scripta Materialia*, 153:68–72.

[69] Hernández-Nava, E., Smith, C. J., Derguti, F., Tammas-Williams, S., Léonard, F., Withers, P. J., Todd, I., and Goodall, R. (2016). The effect of defects on the mechanical response of Ti–6Al–4V cubic lattice structures fabricated by electron beam melting. *Acta Materialia*, 108:279–292.

[70] Hou, Z.-B. and Komanduri, R. (1998). Magnetic field assisted finishing of ceramics—part III: On the thermal aspects of magnetic abrasive finishing (MAF) of ceramic

rollers. *Journal of Tribology*, 120:660–667.

[71] Hrylits' kyi, D., Evtushenko, O., and Pauk, V. (1996). Investigation of thermomechanical processes in the course of polishing. *Materials Science*, 31(2):160–169.

[72] Huang, X., Zhou, Q., Zeng, L., and Li, X. (2015). Monitoring spatial uniformity of particle distributions in manufacturing processes using the K function. *IEEE Transactions on Automation Science and Engineering*, 14(2):1031–1041.

[73] Hutchings, I. M. and Shipway, P. (1992). *Tribology: Friction and Wear of Engineering Materials*. CRC Press, Boca Raton, FL.

[74] Iquebal, A., Shrestha, S., Wang, Z., Manogharan, G., and Bukkapatnam, S. (2016). Influence of milling and non-traditional machining on surface properties of Ti6Al4V EBM components. In *Proceedings of the 2016 Industrial and Systems Engineering Research Conference*.

[75] Iquebal, A. S., Botcha, B., and Bukkapatnam, S. (2020). Towards rapid, in situ characterization for materials-on-demand manufacturing. *Manufacturing Letters*, 23:29–33.

[76] Iquebal, A. S. and Bukkapatnam, S. (2018). Unsupervised image segmentation via maximum a posteriori estimation of continuous max-flow. *arXiv preprint arXiv:1811.00220*.

[77] Iquebal, A. S., El Amri, S., Shrestha, S., Wang, Z., Manogharan, G. P., and Bukkapatnam, S. (2017). Longitudinal milling and fine abrasive finishing operations to improve surface integrity of metal AM components. *Procedia Manufacturing*, 10:990–996.

[78] Iquebal, A. S., Sagapuram, D., and Bukkapatnam, S. T. (2019). Surface plastic flow in polishing of rough surfaces. *Scientific reports*, 9(1):10617.

[79] Ismail, A. B., Rachik, M., Mazeran, P.-E., Fafard, M., and Hug, E. (2009). Material characterization of blanked parts in the vicinity of the cut edge using nanoindentation technique and inverse analysis. *International Journal of Mechanical Sciences*, 51:899–906.

[80] Jain, V. K., Sidpara, A., Sankar, M. R., and Das, M. (2011). Nano-finishing techniques: a review. *Proceedings of the Institution of Mechanical Engineers, Part C: Journal of Mechanical Engineering Science*, page 0954406211426948.

[81] Jiang, X., Scott, P. J., Whitehouse, D., and Blunt, L. (2007a). Paradigm shifts in surface metrology. part I. historical philosophy. *Proceedings of the Royal Society A: Mathematical, Physical and Engineering Sciences*, 463(2085):2049–2070.

[82] Jiang, X., Scott, P. J., Whitehouse, D., and Blunt, L. (2007b). Paradigm shifts in surface metrology. part II. the current shift. *Proceedings of the Royal Society A: Mathematical, Physical and Engineering Sciences*, 463(2085):2071–2099.

[83] Joe, H. (1997). *Multivariate models and multivariate dependence concepts*. Chapman and Hall/CRC.

[84] Kalidindi, S. R. and De Graef, M. (2015). Materials data science: current status and future outlook. *Annual Review of Materials Research*, 45:171–193.

[85] Karimi, N. Z., Heidary, H., and Ahmadi, M. (2012). Residual tensile strength monitoring of drilled composite materials by acoustic emission. *Materials and Design*, 40:229–236.

[86] Kennedy, F. E. (2011). Frictional heating and contact temperature. In Bhushan, B., editor, *Modern Tribology Handbook*, chapter 6, pages 235–259. CRC Press, Boca Raton.

[87] Koch, L. M., Rajchl, M., Bai, W., Baumgartner, C. F., Tong, T., Passerat-Palmbach, J., Aljabar, P., and Rueckert, D. (2018). Multi-atlas segmentation using partially annotated data: Methods and annotation strategies. *IEEE Transactions on Pattern Analysis and Machine Intelligence*, 40(7):1683–1696.

[88] Kolmogorov, V. and Zabih, R. (2004). What energy functions can be minimized via graph cuts? *IEEE Transactions on Pattern Analysis and Machine Intelligence*, (2):147–159.

[89] Komanduri, R. (1971). Some aspects of machining with negative rake tools simulating grinding. *International Journal of Machine Tool Design and Research*, 11(3):223–233.

[90] Layens, C. and Peters, M. (2003). *Titanium and titanium alloys: fundamentals and applications*. Wiley-VCH Verlag GmbH & Co. KGaA.

[91] Lee, Y. and Dornfeld, D. (1998). Application of open architecture control system in precision machining. In *31st CIRP International Seminar on Manufacturing*, pages 436–

441.

[92] Leng, Y. (2009). *Materials characterization: Introduction to microscopic and spectroscopic methods*. John Wiley & Sons.

[93] Li, S. Z. (2009). *Markov random field modeling in image analysis*. Springer-Verlag London.

[94] Liao, S. C. and Duffy, J. (1998). Adiabatic shear bands in a Ti-6Al-4V titanium alloy. *Journal of the Mechanics and Physics of Solids*, 46(11):2201–2231.

[95] Liou, F., Slattery, K., Kinsella, M., Newkirk, J., Chou, H.-N., and Landers, R. (2007). Applications of a hybrid manufacturing process for fabrication of metallic structures. *Rapid Prototyping Journal*, 13(4):236–244.

[96] Lu, P., Yao, N., So, J., Harlow, G., Lu, J., Wang, G., and Chaikin, P. (2005). The earliest use of corundum and diamond, in prehistoric China. *Archaeometry*, 47(1):1–12.

[97] Maia, L. H. A., Abrao, A. M., Vasconcelos, W. L., Sales, W. F., and Machado, A. R. (2015). A new approach for detection of wear mechanisms and determination of tool life in turning using acoustic emission. *Tribology International*, 92:519–532.

[98] Manogharan, G. (2014). *Hybrid Manufacturing: Analysis of Integrating Additive and Subtractive Methods*. North Carolina State University.

[99] Markou, M. and Singh, S. (2006). A neural network-based novelty detector for image sequence analysis. *IEEE Transactions on Pattern Analysis and Machine Intelligence*, 28(10):1664–1677.

[100] Mason, W. P. (1968). Dislocation Drag Mechanisms and Their Effects on Dislocation Velocities. In Rosenfield, A. R., George, H. T., Bement, A. L., and Jaffee, R. I., editors, *Dislocation Dynamics*, number 2, pages 487–505. McGraw-Hill, New York.

[101] Menafoglio, A., Grasso, M., Secchi, P., and Colosimo, B. M. (2018). Profile monitoring of probability density functions via simplicial functional PCA with application to image data. *Technometrics*, 60(4):497–510.

[102] Menze, B., Reyes, M., kalpathy Cramer, J., Farahani, K., Bakas, S., and Davatzikos,

C. (2015). Multimodal brain tumor image segmentation benchmark: “change detection”. In *2016 Proceedings of MICCAI*.

[103] Menze, B. H., Jakab, A., Bauer, S., Kalpathy-Cramer, J., Farahani, K., Kirby, J., Burren, Y., Porz, N., Slotboom, J., Wiest, R., Lanczi, L., Gerstner, E., Weber, M., Arbel, T., Avants, B. B., Ayache, N., Buendia, P., Collins, D. L., Cordier, N., Corso, J. J., Criminisi, A., Das, T., Delingette, H., Demiralp, ., Durst, C. R., Dojat, M., Doyle, S., Festa, J., Forbes, F., Geremia, E., Glocker, B., Golland, P., Guo, X., Hamamci, A., Iftekharuddin, K. M., Jena, R., John, N. M., Konukoglu, E., Lashkari, D., Mariz, J. A., Meier, R., Pereira, S., Precup, D., Price, S. J., Raviv, T. R., Reza, S. M. S., Ryan, M., Sarikaya, D., Schwartz, L., Shin, H., Shotton, J., Silva, C. A., Sousa, N., Subbanna, N. K., Szekely, G., Taylor, T. J., Thomas, O. M., Tustison, N. J., Unal, G., Vasseur, F., Wintermark, M., Ye, D. H., Zhao, L., Zhao, B., Zikic, D., Prastawa, M., Reyes, M., and Van Leemput, K. (2015). The multimodal brain tumor image segmentation benchmark (BRATS). *IEEE Transactions on Medical Imaging*, 34(10):1993–2024.

[104] Mohammadhosseini, A., Fraser, D., Masood, S., and Jahedi, M. (2013). Microstructure and mechanical properties of Ti–6Al–4V manufactured by electron beam melting process. *Materials Research Innovations*, 17(sup2):s106–s112.

[105] Mohar, B. (1997). Some applications of Laplace eigenvalues of graphs. In *Graph symmetry*, pages 225–275. Springer.

[106] Nadler, B. and Galun, M. (2007). Fundamental limitations of spectral clustering. In *Advances in Neural Information Processing Systems*, pages 1017–1024. MIT Press.

[107] Nelsen, R. B. (2007). *An introduction to copulas.* Springer Science & Business Media.

[108] Newton, I. (1979). *Opticks: Or, A Treatise of the Reflections, Refractions, Inflections and Colours of Light.* Dover Publications, New York.

[109] Nguyen, T. M. and Wu, Q. J. (2013). Fast and robust spatially constrained gaussian mixture model for image segmentation. *IEEE Transactions on Circuits Systems and Video Technology*, 23(4):621–635.

[110] Nikol'skii, S. G. and Stepanyants, T. S. (1994). Acoustic emission inspection of the strength of ceramics. *Strength of Materials*, 26:157–161.

[111] Olson, G. B. (2000). Designing a new material world. *Science*, 288:993–998.

[112] Park, C. (2014). Estimating multiple pathways of object growth using nonlongitudinal image data. *Technometrics*, 56(2):186–199.

[113] Park, C., Huang, J. Z., Ji, J. X., and Ding, Y. (2013). Segmentation, inference and classification of partially overlapping nanoparticles. *IEEE Transactions on Pattern Analysis and Machine Intelligence*, 35(3):1–1.

[114] Pedretti, C. (1978). *The Codex Atlanticus of Leonardo da Vinci: A Catalogue of its Newly Restored Sheets*. Johnson Reprint Corporation, New York.

[115] Petrick, I. J. and Simpson, T. W. (2013). 3D printing disrupts manufacturing. *Research Technology Management*, 56(6):12.

[116] Pollock, A. A. (1973). Acoustic emission - 2: Acoustic emission amplitudes. *Nondestructive Testing*, 6:264–269.

[117] Pollock, T. M. and Van der Ven, A. (2019). The evolving landscape for alloy design. *MRS Bulletin*, 44:238–246.

[118] Powers, A. S., Liao, H.-G., Raja, S. N., Bronstein, N. D., Alivisatos, A. P., and Zheng, H. (2016). Tracking nanoparticle diffusion and interaction during self-assembly in a liquid cell. *Nano Letters*, 17(1):15–20.

[119] Rabinowicz, E. (1968). Polishing. *Scientific American*, 218(6):91–99.

[120] Rao, P., Bukkapatnam, S., Kong, Z., Beyca, O., Case, K., and Komanduri, R. (2015). Quantification of ultraprecision surface morphology using an algebraic graph theoretic approach. *Procedia Manufacturing*, 1:12–26.

[121] Ribeiro, M. T., Singh, S., and Guestrin, C. (2016). Why should I trust you?: Explaining the predictions of any classifier. In *Proceedings of the 22nd ACM SIGKDD International Conference*, pages 1135–1144. ACM.

[122] Rittel, D., Landau, P., and Venkert, A. (2008). Dynamic recrystallization as a potential

cause for adiabatic shear failure. *Physical Review Letters*, 101(16):165501.

[123] Sagapuram, D., Viswanathan, K., Mahato, A., Sundaram, N. K., M'Saoubi, R., Trumble, K. P., and Chandrasekar, S. (2016). Geometric flow control of shear bands by suppression of viscous sliding. *Proceedings of the Royal Society of London A: Mathematical, Physical and Engineering Sciences*, 472(2192).

[124] Sagapuram, D., Viswanathan, K., Trumble, K. P., and Chandrasekar, S. (2018). A common mechanism for evolution of single shear bands in large-strain deformation of metals. *Philosophical Magazine*, 98(36):3267–3299.

[125] Sakia, R. (1992). The Box-Cox transformation technique: a review. *Journal of the Royal Statistical Society: Series D (The Statistician)*, 41(2):169–178.

[126] Sames, W. J., List, F., Pannala, S., Dehoff, R. R., and Babu, S. S. (2016). The metallurgy and processing science of metal additive manufacturing. *International Materials Reviews*, 61:315–360.

[127] Samuels, L. E. (2003). *Metallographic Polishing by Mechanical Methods.* ASM International, Materials Park, OH.

[128] Sause, M., Müller, T., Horoschenkoff, A., and Horn, S. (2012). Quantification of failure mechanisms in mode-I loading of fiber reinforced plastics utilizing acoustic emission analysis. *Composites Science and Technology,*, 72:167–174.

[129] Schepsmeier, U., Stoeber, J., Brechmann, E. C., Graeler, B., Nagler, T., Erhardt, T., Almeida, C., Min, A., Czado, C., Hofmann, M., et al. (2018). Package 'VineCopula'. *R package version*, 2(5).

[130] Shalabi, M., Gortemaker, A., Van't Hof, M., Jansen, J., and Creugers, N. (2006). Implant surface roughness and bone healing: a systematic review. *Journal of Dental Research*, 85(6):496–500.

[131] Shaw, L. and Miracle, D. (1995). On the relationship between microstructure and acoustic emission in Ti-6Al-4V. *Journal of Materials Science*, 30:4286–4298.

[132] Shi, J. and Malik, J. (2000). Normalized cuts and image segmentation. *IEEE Trans-*

actions on Pattern Analysis and Machine Intelligence, 22(8):888–905.

[133] Sikaroudi, A. E., Welch, D. A., Woehl, T. J., Faller, R., Evans, J. E., Browning, N. D., and Park, C. (2018). Directional statistics of preferential orientations of two shapes in their aggregate and its application to nanoparticle aggregation. *Technometrics*, 60(3):332–344.

[134] Sklar, M. (1959). Fonctions de répartition à n dimensions et leurs marges. *Publications de l'Institut Statistique de l'University de Paris*, 8:229–231.

[135] Spielman, D. A. and Teng, S. H. (2007). Spectral partitioning works: Planar graphs and finite element meshes. *Linear Algebra and its Applications*, 421(2):284–305.

[136] Stout, K. J. and Blunt, L. (2000). *Three dimensional surface topography*. Elsevier.

[137] Strong, D. and Chan, T. (2003). Edge-preserving and scale-dependent properties of total variation regularization. *Inverse Problems*, 19(6):S165.

[138] Sundaram, N. K., Guo, Y., and Chandrasekar, S. (2012). Mesoscale folding, instability, and disruption of laminar flow in metal surfaces. *Physical Review Letters*, 109:106001.

[139] Tammas-Williams, S., Withers, P., Todd, I., and Prangnell, P. (2017). The influence of porosity on fatigue crack initiation in additively manufactured titanium components. *Scientific Reports*, 7(1):7308.

[140] Thomas, N., Iquebal, A. S., and Bukkapatnam, S. (2016). Nanofinishing of Biomedical Implants. In Jain, V. K., editor, *Nanofinishing Science and Technology: Basic and Advanced Finishing and Polishing Processes*, chapter 20, pages 569–616. CRC Press, Boca Raton.

[141] Tian, X. and Kennedy, F. E. (1993). Contact surface temperature models for finite bodies in dry and boundary lubricated sliding. *Journal of Tribology*, 115(3):411–418.

[142] Tian, X. and Kennedy, F. E. (1994). Maximum and average flash temperatures in sliding contacts. *Journal of Tribology*, 116(1):167–174.

[143] Uchic, M. D., Dimiduk, D. M., Florando, J. N., and Nix, W. D. (2004). Sample dimensions influence strength and crystal plasticity. *Science*, 305(5686):986–989.

[144] Wang, G., Zuluaga, M. A., Li, W., Pratt, R., Patel, P. A., Aertsen, M., Doel, T., Divid,

A. L., Deprest, J., Ourselin, S., et al. (2018). DeepIGeoS: a deep interactive geodesic framework for medical image segmentation. *IEEE Transactions on Pattern Analysis and Machine Intelligence*.

[145] Wang, K. and Tsung, F. (2005). Using profile monitoring techniques for a data-rich environment with huge sample size. *Quality and reliability engineering international*, 21(7):677–688.

[146] Wang, L., Guan, P., Teng, J., Liu, P., Chen, D., Xie, W., Kong, D., Zhang, S., Zhu, T., Zhang, Z., et al. (2017). New twinning route in face-centered cubic nanocrystalline metals. *Nature Communications*, 8(1):2142.

[147] Wang, L., Teng, J., Liu, P., Hirata, A., Ma, E., Zhang, Z., Chen, M., and Han, X. (2014). Grain rotation mediated by grain boundary dislocations in nanocrystalline platinum. *Nature Communications*, 5:4402.

[148] Wang, Z., Palmer, T. A., and Beese, A. M. (2016). Effect of processing parameters on microstructure and tensile properties of austenitic stainless steel 304L made by directed energy deposition additive manufacturing. *Acta Materialia*, 110:226–235.

[149] Wei, K., Tai, X.-C., Chan, T. F., and Leung, S. (2015). Primal-dual method for continuous max-flow approaches. In *Computational Vision and Medical Image Processing V: Proceedings of the 5th Eccomas Thematic Conference on Computational Vision and Medical Image Processing (VipIMAGE 2015, Tenerife, Spain*, pages 17–24.

[150] Wei, Q., Lü, J., Yang, Q., and Li, X. (2018). Multi-pass micro-scratching and tribological behaviors of an austenitic steel in media. *Tribology International*, 117:112–118.

[151] Winter, P. and McDonald, W. (1969). Biaxial residual surface stresses from grinding and finish machining 304 stainless steel determined by a new dissection technique. *Journal of Basic Engineering*, 91(1):15–22.

[152] Wisner, B., Mazur, K., Perumal, V., Baxevanakis, K. P., An, L., Feng, G., and Kontsos, A. (2019). Acoustic emission signal processing framework to identify fracture in aluminum alloys. *Engineering Fracture Mechanics*, 210:367–380.

[153] Wycisk, E., Emmelmann, C., Siddique, S., and Walther, F. (2013). High cycle fatigue (HCF) performance of Ti-6Al-4V alloy processed by selective laser melting. *Advanced Materials Research*, 816-817:134–139.

[154] Xiang, W., Xuliang, M., Xinlin, L., Lihua, D., and Mingjia, W. (2012). Effect of boron addition on microstructure and mechanical properties of TiC/Ti6Al4V composites. *Materials & Design (1980-2015)*, 36:41–46.

[155] Xie, Y. and Bhushan, B. (1996). Effects of particle size, polishing pad and contact pressure in free abrasive polishing. *Wear*, 200(1-2):281–295.

[156] Xiong, X., Zhang, H., and Wang, G. (2009). Metal direct prototyping by using hybrid plasma deposition and milling. *Journal of Materials Processing Technology*, 209(1):124–130.

[157] Yan, M. and Yu, P. (2015). An overview of densification, microstructure and mechanical property of additively manufactured Ti-6Al-4V—comparison among selective laser melting, electron beam melting, laser metal deposition and selective laser sintering, and with conventional powder. In Lakshmanan, A., editor, *Sintering Techniques of Materials*. InTech.

[158] Yang, W., Guo, L., Zhao, T., and Xiao, G. (2007). Improving watersheds image segmentation method with graph theory. In *2007 2nd IEEE Conference on Industrial Electronics and Applications*, pages 2550–2553. IEEE.

[159] Yashchuk, V. V., Tyurin, Y. N., and Tyurina, A. Y. (2016). Modeling of surface metrology of state-of-the-art X-ray mirrors as a result of stochastic polishing process. *Optical Engineering*, 55(7):074106.

[160] Yeo, A., Kai, Y., Che, F., and Zhou, K. (2017). Study on damage and fracture of thin-film stacked structures through indentation test with acoustic emission sensing. *International Journal of Mechanical Sciences*, 128:159–167.

[161] Yuan, J., Bae, E., and Tai, X.-C. (2010a). A study on continuous max-flow and min-cut approaches. In *IEEE Computer Society Conference on Computer Vision Pattern*

Recognition (CVPR), pages 2217–2224. IEEE.

[162] Yuan, J., Bae, E., Tai, X.-C., and Boykov, Y. (2010b). A continuous max-flow approach to Potts model. In *European Conference on Computer Vision (ECCV)*, pages 379–392. Springer.

[163] Yuan, J., Bae, E., Tai, X.-C., and Boykov, Y. (2014). A spatially continuous max-flow and min-cut framework for binary labeling problems. *Numerische Mathematik*, 126(3):559–587.

[164] Zhang, L., Wang, K., and Chen, N. (2016). Monitoring wafers' geometric quality using an additive gaussian process model. *IIE Transactions*, 48(1):1–15.

[165] Zhang, Y., Brady, M., and Smith, S. (2001). Segmentation of brain MR images through a hidden Markov random field model and the expectation-maximization algorithm. *IEEE Transactions on Medical Imaging*, 20(1):45–57.

[166] Zhou, Q., Tang, P., Liu, S., Pan, J., Yan, Q., and Zhang, S.-C. (2018). Learning atoms for materials discovery. *Proceedings of the National Academy of Sciences*, 115(28):E6411–E6417.

[167] Zong, H., Pilania, G., Ding, X., Ackland, G. J., and Lookman, T. (2018). Developing an interatomic potential for martensitic phase transformations in zirconium by machine learning. *npj Comput Mat*, 4:48.